University of Reading

Diamond Light Source

HARD AND SOFT NANOMATERIAL FILMS

A thesis submitted for the degree of Doctor of Philosophy

Department of Chemistry

Samuel J. Richardson

Supervisors: Adam Squires, Joanne Elliott, Nick Terrill

September 2016

Declaration

I confirm that this is my own work and the use of all material from other sources has been properly and fully acknowledged.

Signed: Date:

Acknowledgements

I would like to thank everyone who provided help and advice to me during my PhD research and throughout the write-up of this thesis. Also to Diamond Light Source and the University of Reading for funding my research.

I am sincerely grateful to my supervisors Adam Squires, Joanne Elliott and Nick Terrill; I owe all of my achievements to their expert guidance, feedback and inspiration.

Additionally, I am indebted to those who assisted with my work at various synchrotron trips, particularly Matt Burton, Nassar Abdelrahim, Paul Staniec, Kunal Rastogi, Annela Seddon and Christian Pfrang. A large portion of the data in this thesis was collected over approximately 30 collective days of experiments, so all the input received is greatly appreciated. Moreover, I would like thank the beamline and support scientists at Diamond, MaxLab and ESRF for their support in experimental setup and efforts to fix equipment in the middle of the night, especially Jonathan Rawle and Tomás Plivelic.

Further gratitude goes to Nick Spencer, for valuable assistance with the X-ray facilities at Reading, and Peter Harris and Amanpreet Kaur of the EMLab, who provided training and support in my electron microscopy measurements.

I'm thankful to my parents and sister for their support and faith that I would eventually finish this thesis. Finally, my greatest thanks are for Annabel, who managed to always remain encouraging and optimistic, keeping me motivated whilst writing this thesis in my spare time over the past year.

Abstract

Bicontinuous cubic phases are high surface area nanostructures formed spontaneously by amphiphilic lipids on contact with water. This thesis reports studies into the behaviour of thin lipid films, capable of forming bicontinuous cubic phases, and their use as soft templates for the electrodeposition of aligned platinum nanostructures. In addition, the suitability of these mesoporous films for use as catalysts in direct alcohol fuel cells is detailed.

Through an experimental and theoretical study of thin films of lipid under controlled humidity, it was demonstrated that adding glycerol progressively lowers the humidity at which Q_{II} phase films are stable, without affecting their lattice parameter[1]. These findings open up the possibility of utilising cubic phases in a much wider range of environments, where typically the structure would collapse due to dehydration. The addition of glycerol allowed for a study into the orientation adopted by these lipid films[2]; the Q_{II}^G and the Q_{II}^D phases were observed to be reproducibly orientated with the (110) and the (111) facets aligned parallel to the substrate respectively up to a measured thickness of 1.4 µm. These results agreed with theoretical predictions based on the minimization of interfacial energy.

Self-assembled cubic phase films were used to template mesoporous platinum nanostructures 1-2 microns thick featuring uniaxial alignment with the (111) plane orientated parallel to the substrate and high surface area (42 ± 1 m^2/g) [3]. To investigate the electrodeposition process time resolved X-ray scattering measurements were taken *in situ* as the platinum nanostructures grew within the lipid template using a custom electrochemical cell developed for use on a synchrotron beamline[4]. These measurements identified two surprising

characteristics of the templated electrodeposition process. Firstly, the aligned platinum nanostructures are templated from polydomain lipid films, suggest that up to 3 μm away from the lipid/substrate interface, polydomain Q_{II} samples display a region of uniaxial orientation. Secondly, the platinum films are found to be cubic while the lipid template is in place but undergo a slight distortion of the lattice along the 111 direction once the template is removed resulting in a rhombohedral structure where $\alpha = 87\,^{\circ}$ ($\alpha = 90^{\circ}$ for cubic structures).

Additionally, these phytantriol templated platinum nanostructures were assessed for use as anode catalysts in alcohol fuel cells. The catalytic response towards the oxidation of methanol and ethanol was found to be enhanced in phytantriol-directed nanostructured films in comparison to non-structured platinum. Lipid templated platinum was directly electrodeposited onto porous carbon gas diffusion layers as used in conventional fuel cell design. Platinum nanostructures on carbon and gold disc electrodes showed a comparable result towards the oxidation of ethanol. These findings present lipid templated electrodeposition as a practical method to incorporate nanostructured platinum materials into conventional fuel cell designs for enhanced catalytic response towards the oxidation of alcohols.

Table of Contents

1 INTRODUCTION

1.1 AMPHIPHILIC SELF-ASSEMBLY AND BICONTINUOUS CUBIC PHASES

Bicontinuous cubic phases are a class of structure exhibited by the aggregation of hydrated amphiphilic lipids. The chemical structure of an amphiphilic lipid known as phytantriol, which is used extensively in this report, is shown in Figure 1.1.

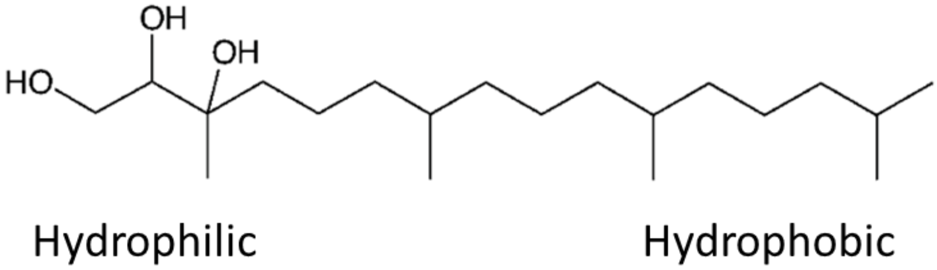

Figure 1.1 Chemical structure of phytantriol with the general form of an amphiphilic lipid shown in Figure 1.2.

This class of molecules contains two main components: a head group, which is hydrophilic; and a tail section, which is hydrophobic. In the case of phytantriol, the head group is composed of three hydroxyl groups and the tail section is composed of a long carbon chain[5]. The hydroxyl groups are highly polar leading to a strong affinity to water, whereas the carbon chain is non-polar leading to repulsion. The combination of these two distinct sections results in two opposing forces acting on the molecule when exposed to water. On their own, the head groups would dissolve completely in order to fully surround themselves in water molecules. The tail sections, however, would favour complete phase separation, in order to minimise the contact area. The combination of these effects leads to aggregation of the molecules into various structures in order to satisfy the two forces[5]. Figure 1.2 depicts some of the various structures formed by hydrated lipids.

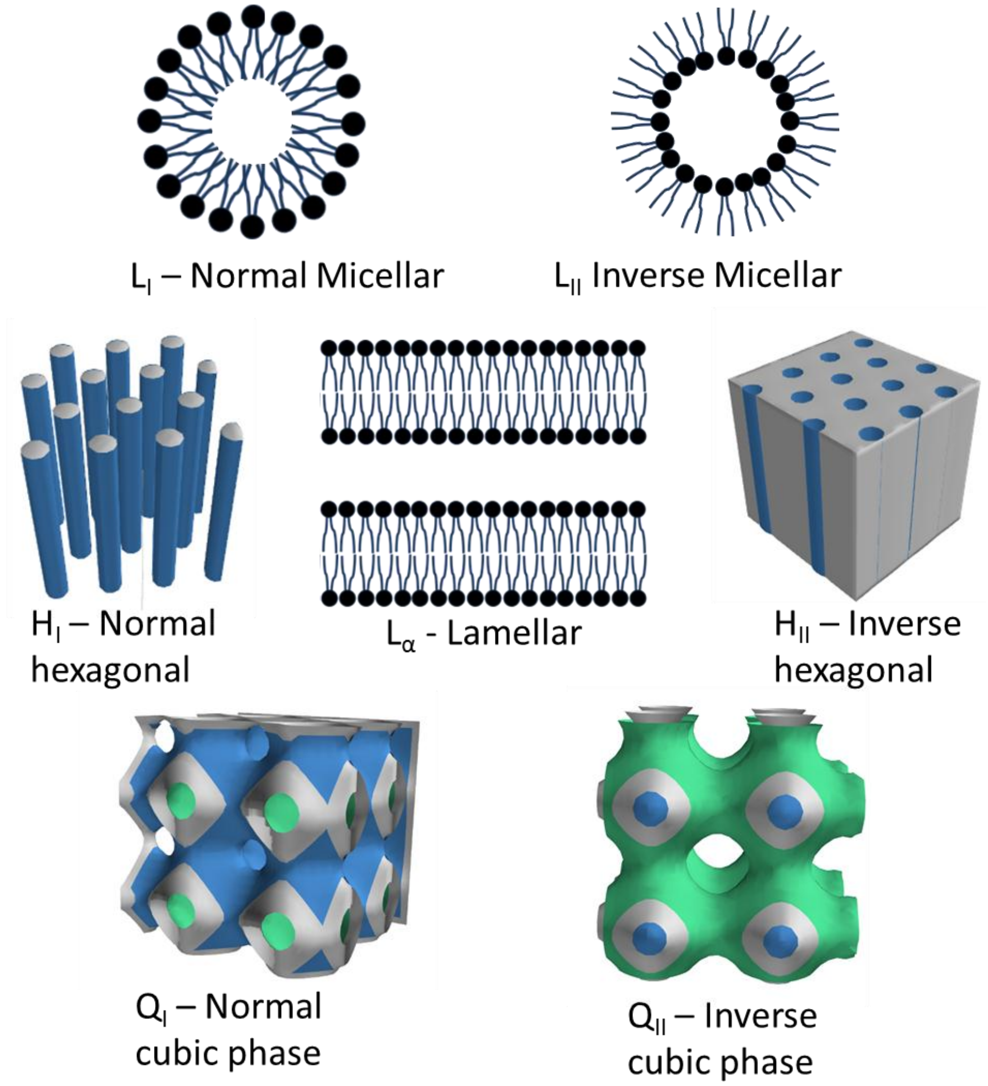

Figure 1.2. Various structures formed by amphiphilic lipids.

The type of lipid, its concentration and temperature are the main determinants of the adopted structure[6,7], however, certain additives can also influence the structure formation[8]. Generally, at low surfactant concentrations, molecules aggregate to form simple spherical structures known as micelles. As the molecule concentration increases, these rearrange to form continuous structures known as a mesophase[9].

The physical dimensions of the lipid monomer, defined by a packing parameter[10], P, determine the potential lipid aggregations in a particular system. This parameter is defined by,

$$P = \frac{v}{al}$$

where v is the volume, l is the length of the hydrocarbon chain and a is the area per molecule at the aggregate interface. Lipids are defined as type I or II dependent on whether this parameter is greater or less than 1, which leads to the formation of normal or inverse structures respectively, as shown in Figure 1.3.

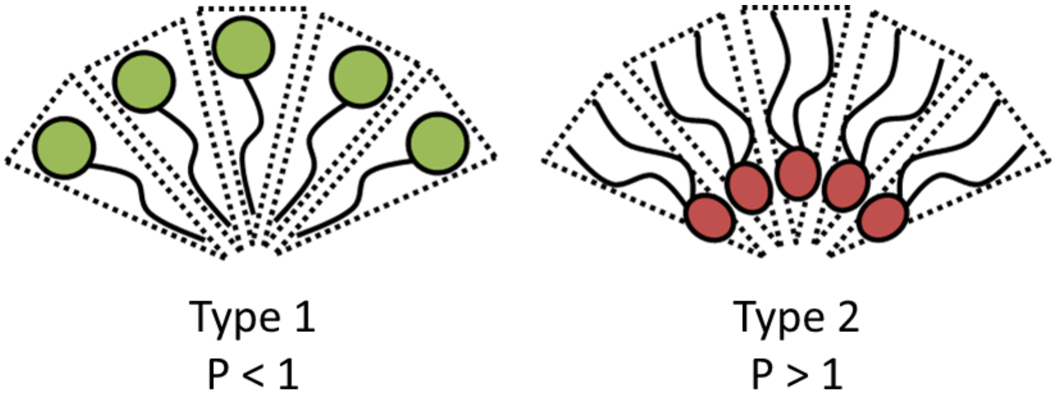

Figure 1.3. Schematic of type I and type II lipids demonstrating the packing of aggregated molecules.

Type I lipids have a relatively large head group compared to the tail, whereas type II have a larger tail area; phytantriol is an example of a type II lipid. All phases that display elements of curvature, i.e. micelle, hexagonal or cubic, have normal or inverse varieties formed by type I or II lipids respectively. The difference in these structures is that the lipid bilayer curves either towards (inverse) or away (normal) from the water. The resulting structures appear similar when just considering the lipid layer; however, they lead to a very different containment of water. Using the hexagonal phase for example, as shown in Figure 1.2, the regular hexagonal structure features a bulk water network with a hexagonal arrangement of cylindrical lipid layers; conversely the inverse structure features many disconnected water channels.

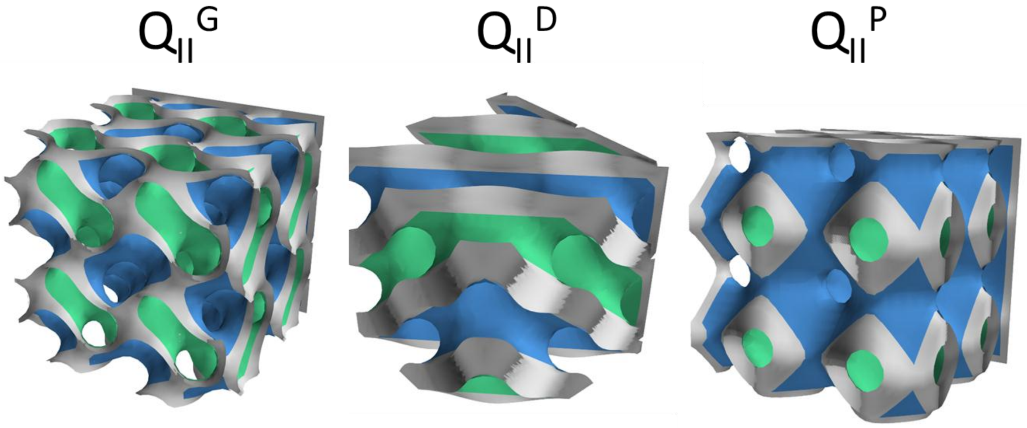

Figure 1.4. Models of the three inverse Bicontinuous cubic phases. The blue and green surfaces represent the two water channels and the grey region represents the area containing the lipid bilayer**.**

A common feature of many of these phases is the lipid bilayer sheet; the lamellar phase shown in Figure 1.2 is composed of multiple flat bilayer sheets, stacked above one and another with layers of water in-between. Bicontinuous cubic phases are a more complex structure, but formed in the same manner; these mesophases are composed of a continuous curved bilayer sheet lying between two separate water channel networks. This type of phase can also be regular or inverse depending upon its curvature. Figure 1.4 shows the three reported types of inverse cubic phase, Q_{II}^D (diamond), Q_{II}^G (gyroid) and Q_{II}^P (primitive) [11]. Each phase can be described by a mathematical surface, which is known as a triply periodic minimal surface and maps the centre of the bilayer sheet.

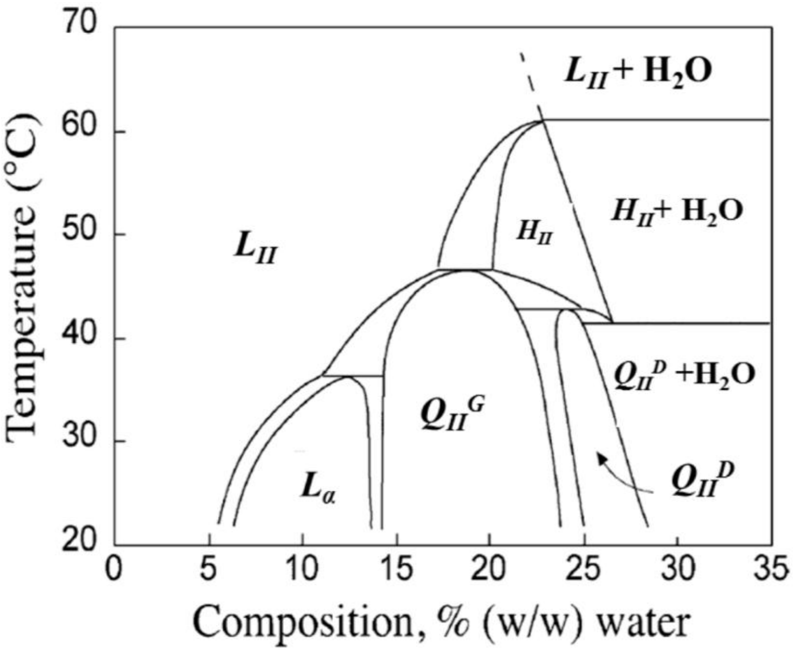

Figure 1.5. Phase composition plot for the phytantriol/water system with respect to temperature[9,12].

1.2 ORIENTATION OF LIPID CUBIC PHASES

In bulk, lipid cubic phases are described as polydomain, as they are composed of many randomly orientated domains thought to be on the micron scale[13]. There are, however, several reasons why it would be advantageous to produce lipid cubic samples with an overall alignment. Orientation can be described as either uniaxial or biaxial dependent on whether one or two axes of the unit cell are fixed in orientation across the sample. Methods of inducing both uniaxial and biaxial orientation in Q_{II} phase samples have previously been reported using a range of conditions such as shear force[13], cooling from melt[14], and controlled dilution from a disordered sponge phase[15]. For example, a shear induced uniaxially aligned Q_{II}^D phase has been produced during a controlled dilution of a sponge phase formed by a monoolein / butanediol system[13]. A similar technique was used to produce orientation in thin films of both Q_{II}^D and Q_{II}^G phase formed by lipids coated onto the inside of a capillary[16]. Further reports demonstrated the controlled dilution from a sponge phase could also be used to produce biaxially orientated structures[15]. Finally, reduced sample dimensions have also been demonstrated to produce orientation, with Rittman et al. reporting the observation of thin films of phytantriol and monoolein forming the Q_{II}^{D} and Q_{II}^{G} phases, both with two facets orientated parallel to the substrate[17].

1.3 APPLICATIONS OF LIPID CUBIC PHASES

The unique geometry of the Q_{II} phases has led to a wide variety of applications within material, biological and medical sciences. Lipid cubic phases have been demonstrated to be a suitable environment for the crystallisation of membrane proteins[18–21] leading to records of almost 200 new protein structures[19]. In addition, the recently developed serial femtosecond crystallography utilises a lipid cubic phase matrix to reduce the amount of protein required for an experiment[22]. There has been a lot of interest in the use of cubic phases for the delivery of drugs, both as distinct particles of cubic phase known as cubosomes for oral[23] and intranasal[24] administration and as a film applied directly to the skin for topical delivery[25,26]. Cubic phases have both hydrophobic and hydrophilic regions, allowing a great variety of active ingredients to be carried, and a high internal volume, for a high degree of drug loading per volume unit[27]. Furthermore, cubic phases have the potential to be used as a smart delivery system, where release of the active ingredient is controlled or triggered by changes to environmental conditions such as pH[28] or temperature[29–31] . Beyond these two applications, cubic phases have demonstrated value for use in sensors[32], ion conductivity media for batteries and fuel cells[33], aroma release[34] and in the templating of mesoporous metals[35].

1.4 MESOPOROUS MATERIALS

Much of this thesis covers the application of lipid cubic phases as templates to produce mesoporous materials. Materials classed as mesoporous feature pores of dimensions between 2 and 50 nm. Due to these pores, mesoporous materials have an extremely high internal surface area, which is an appealing property for use in catalysts[36], drug delivery[37], solar cells[38,39] and metamaterials[40].

Attard et al. first demonstrated true liquid crystal templating in 1997[41], by electrodepositing metal directly onto a substrate coated in a type I liquid crystal template with hexagonal morphology. There have been many subsequent reports of templating through the hexagonal phase[42], but so far very little utilising cubic phases. Cubic phases formed by type I lipids are much more viscous than those of hexagonal phase[43] which, along with only being observed for a small region of the composition-temperature phase diagram[12], has meant their use in deposition has only been reported once[44]. Work by Akbar et al. demonstrated that it was possible to use type II cubic phases to directly template a nanostructured platinum structure[45]. The cubic phase of the type II lipid phytantriol is stable in excess hydration[12], which was exploited by using a substrate coated in a thin film lipid template that could be submerged in liquid analyte to form a Q_{II} phase. This overcame difficulties of working with such viscous samples, as the thin film template could be applied to the sample through dip-coating from a non-viscous lipid and ethanol solution. Phytantriol was applied as a thin film to the surface of an electrode, where it was used to template the electrodeposition of platinum from hexachloroplatinic acid (HCPA). Due to only one channel of the cubic phase being exposed to the bulk solution, a previously unreported 'single diamond' structure was discovered. These structures exhibited an extremely high specific surface area whilst maintaining a relatively simple one-pot production under chemically mild conditions and temperatures.

1.5 DIRECT ALCOHOL FUEL CELLS

Future energy demands for transportation require a new greener alternative to limited and environmentally damaging fossil fuels such as petroleum. Fuel cell technology potentially offers a route to reliable sustainable energy; these systems are able to convert chemical energy in fuels such as ethanol and methanol into electrical energy. Both fuel sources have relatively high energy densities comparable to that of petrol[46] and can be easily handled and transported in their liquid form, overcoming infrastructure issues associated with the storage and transportation of compressed gas required for hydrogen fuel cells[47,48].

A fuel cell consists of three main sections. An anode, cathode and ion exchange membrane. Fuel and water are inserted at the anode and oxidised, producing electrons and hydrogen ions. For methanol this half reaction is[49],

$$\mathrm{CH_3OH + H_2O \rightarrow 6H^+ + 6e^- + CO_2}$$

At the cathode, the electrons and hydrogen ions participate in a reduction reaction with O_2 pumped into the device[49],

$$\mathrm{\tfrac{3}{2}O_2 + 6H^+ + 6e^- \rightarrow 3H_2O}$$

Combined, the overall reaction is[49],

$$\mathrm{CH_3OH + \frac{3}{2}O_2 \rightarrow 2H_2O + CO_2}$$

The combined reaction produces the by-products of H_2O and CO_2 which is also the case for the ethanol fuel cell[50]. The ion exchange membrane has been specially designed to only allow for the transfer of ion currents between the anode and cathode forcing the electron current to pass through an external load, providing power to a connected device[51].

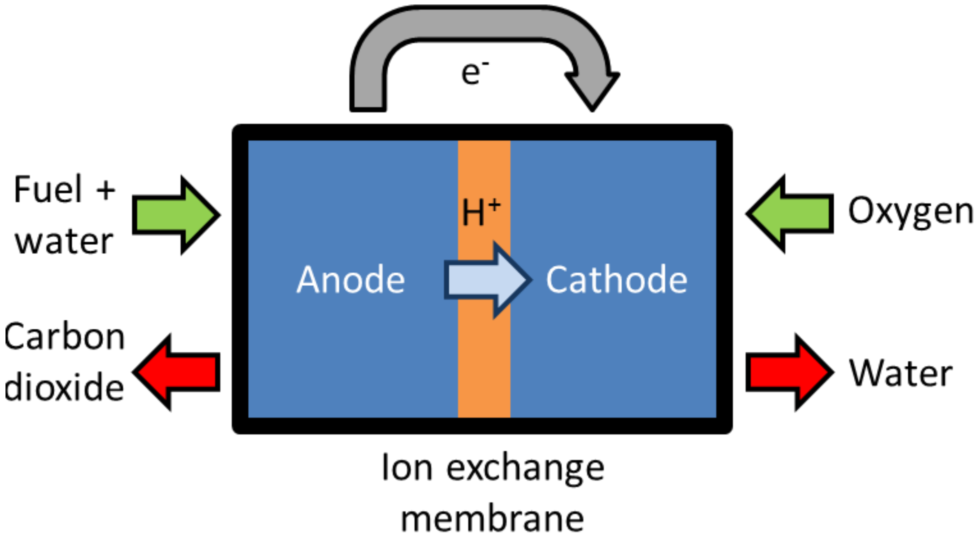

Figure 1.6. Schematic showing the operation of a fuel cell.

One of the main issues restricting the mass commercialisation of these technologies is the requirement for precious metal catalysts at the cathode and anode, which accounts for the majority of a fuel cells cost. The current industry standard for use as catalysts are carbon supported platinum nanoparticles, which provide extremely high available surface area per gram and thus mass activity (activity per gram) due to their nanoscale dimensions[52]. However, these catalysts still require too much precious material and are prone to a loss in surface area through poisoning, coalescence and detachment, leading to an overall reduction in active catalytic sites[53]. Recently, 3D ordered nanostructures have been proposed as an alternative to these nanoparticle systems[54–56]. These structures, typically based on the gyroid minimal surface, are fabricated through directed silica[54,56] or etched block copolymer[55] routes. The ordered platinum structures formed have shown greatly enhanced catalytic activity per unit area in comparison to commercial nanoparticles, thought to be due to the gyroid morphology featuring a higher proportion of the more active (100) and (111) facets[54]. In addition, their 3D structure gives greatly enhanced stability when compared to nanoparticles, postulated as a result of the self-supporting nature of the 3D topology[54].

1.6 THESIS OVERVIEW

This thesis describes several studies into lipid cubic phases formed by amphiphilic lipids, the fabrication of mesoporous materials from lipid cubic templates, and characterisation of the catalytic properties of mesoporous platinum for direct alcohol fuel cells. In addition to this experimental work, Chapter 2 gives a brief overview of the methods utilised throughout this thesis, in order to give context to the results for those unfamiliar with the techniques. The experimental findings begin in Chapter 3, which describes a series of GISAXS experiments performed upon thin lipid films under controlled humidity. Thin lipid films are shown to feature uniaxial orientation, agreeing with theoretical predications where the minimisation of interfacial energy drives alignment. Additionally, the additive glycerol is shown to reduce the humidity required for cubic phases to form. Chapter 4 details a study into the electrodeposition of mesoporous platinum films from a lipid template, producing aligned platinum structures from polydomain lipid cubic templates. A study monitoring the symmetry of the template and deposit by SAXS during the electrodeposition process investigates the mechanisms leading to the aligned platinum structures in more detail. Chapter 5 reports the catalytic characterisation of these platinum nanostructures for use in direct alcohol fuel cells, with a comparison to current commercial catalysts and other mesoporous structures. Finally, a conclusion and summary of all the work is given in Chapter 6, along with a proposed list of future directions if further research time was available.

2 TECHNIQUES

2.1 ELECTROCHEMISTRY

Electrochemistry is an expansive field concerned with the relationship between electricity and chemical reactions. Many important current technologies are based on electrochemical concepts such as batteries, supercapacitors and fuel cells. Throughout this thesis electrochemical techniques are used in order to fabricate and characterise samples the main techniques being: chronoamperometry, whereby a set potential is applied whilst the current is measured over time; and cyclic voltammetry, where a voltage ramp is applied whilst again recording the current. All electrochemical experiments described take place in a cell containing three electrodes (working, reference and counter), placed in an electrolyte solution (as shown in Figure 2.1) and the potential difference between the working and reference electrode is controlled by a potentiostat. In this system, a circuit is made between the potentiostat, working and counter electrodes with the reference electrode used to monitor the potential of the working electrode. The electrochemical cell used for both experiments consisted of a silver/silver chloride reference electrode (RE) with a platinum flag counter electrode (CE). Various gold working electrodes (WE) were used, described in more detail in Chapter 4. The working electrode makes contact with an analyte and is used to apply potential, allowing the transfer of charge to and from the analyte. The reference electrode has a known reduction potential (measure of a chemical species' ability to acquire electrons) and the counter electrode is used to balance the charge of the working electrode[57].

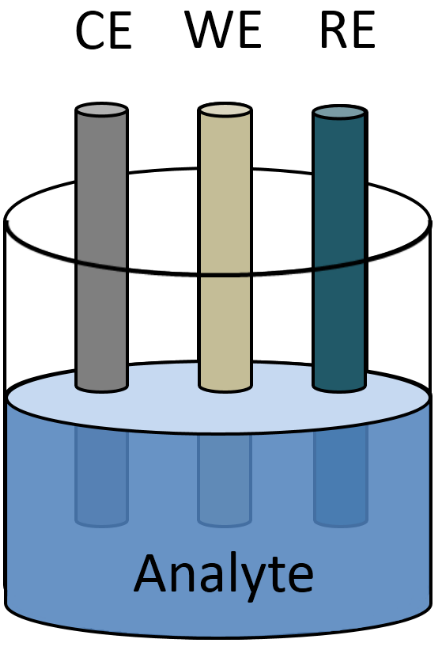

Figure 2.1. Schematic of an electrochemical cell used, with a working electrode (WE), counter electrode (CE) and reference electrode (RE) submerged in an analyte.

2.1.1 Amperometry

Platinum was deposited onto the surface of the working electrode using a potential step amperometry technique. For this method, a potential is applied to the working electrode whilst the current is measured as a function of time. Initially, a set potential, E_1, is applied to the working electrode; E_1 is chosen so that the reduction of platinum is thermodynamically unfavourable. The potential is then rapidly stepped from E_1 to another value, E_2, set so the reduction of platinum is now favourable. This causes current to flow as platinum species towards the electrodes, resulting in metal deposition at the surface.

This technique allows for the quantity of material deposited to be monitored *in situ, as* the amount of material deposited onto the surface can be estimated from the amount of charge passed. For the deposition of platinum from hexachloroplatinic acid, electrons are transferred from the electrode surface to the solution allowing solid platinum to be deposited according to the following three redox couples[58],

(1) $PtCl_6^{2-} + 2e^- \leftrightarrow PtCl_4^{2-} + 2\ Cl^-$ E° = 0.47 V vs. Ag/AgCl

(2) $PtCl_4^{2-} + 2e^- \leftrightarrow Pt_s + 4\ Cl^-$ E° = 0.45 V vs. Ag/AgCl

(3) $PtCl_6^{2-} + 4e^- \leftrightarrow Pt_s + 6\ Cl^-$ E° = 0.46 V vs. Ag/AgCl

The deposition of platinum metal is a four electron processes where the mass of platinum, m_{Pt}, can be found by,

$$\mathrm{m_{Pt}} = \frac{1}{4}\left(\frac{\mathrm{QM_{Pt}}}{\mathrm{Q_e}}\right)$$

Where Q is the charge passed, M_{Pt} is the atomic mass of platinum (195.078 g/mol) and Q_e is the charge of a mole of electrons.

Amperometry experiments were also performed to measure catalytic stability in platinum samples. As alcohol is oxidised at the anode of a fuel cell, carbon monoxide (CO) is produced as a by-product. This CO can bind to the surface of the catalyst, reducing the active area and thus the catalytic response of the material. By applying a set over potential where oxidation occurs this degradation can be monitored as a function of time.

2.1.2 Cyclic voltammetry

Cyclic voltammetry (CV) is one of the most flexible electrochemical measurements and is appropriate in many circumstances. This technique is primarily used to measure the redox potentials of a material, but can also be used for measuring capacitance, system stability and elemental identification as well being a means to estimate electroactive surface area.

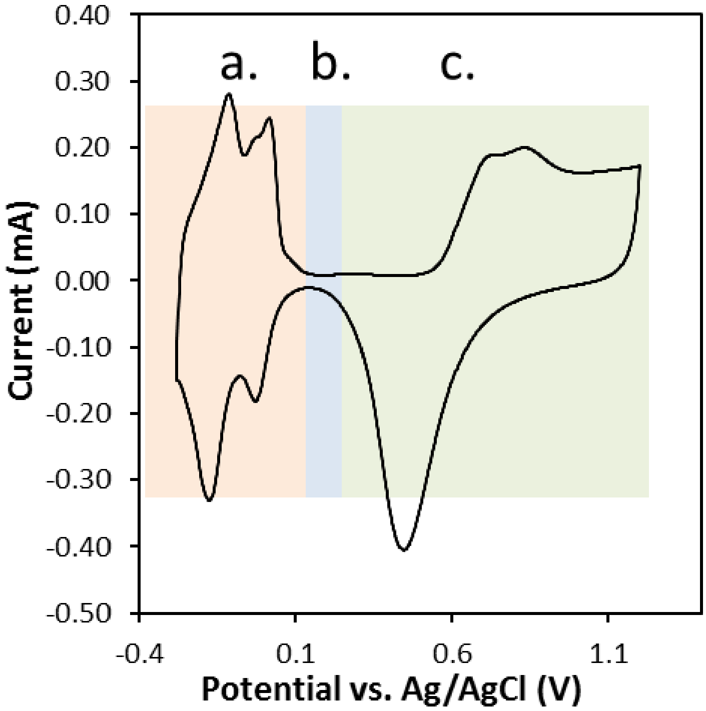

Figure 2.2. Typical CV measurement of a platinum surface, where the hydride (a), double layer (b) and redox (c) regions can be observed.

In a typical CV measurement, the current through the working electrode is measured as a function of time, whilst an applied potential is varied or cycled between an upper and lower limit at a set scan rate, (V/s)[59]. The upper and lower limit are chosen to be just within range of the oxidation and reduction potentials of the working electrode; for platinum this is ~-0.25V to 1.2 V vs Ag/AgCl[42].

Platinum electrodes have a characteristic trace when measured in acid using cyclic voltammetry, as shown in Figure 2.2. Initially, the potential is scanned in the positive direction, which causes the oxidation of platinum on the surface of the electrode and a positive, anodic current to flow between the acid and the working electrode, as electrons are carried towards the metal interface. When the scan direction is reversed, the species reduces at the working electrode resulting in a negative, cathodic current. As demonstrated in Figure 2.2, the hysteresis measured (voltammogram), has three distinct regions: hydride, double layer and redox, **a**, **b** and **c** respectively. Initially a potential of 0.2 V is applied relative to the reference electrode. As the potential becomes more positive, anodic current flows due to the formation of adsorbed oxygen or the formation of platinum oxide. When the current is reversed, cathodic current flows due to the reduction of the surface platinum oxide. Once the material is fully reduced, opposing charges will build up at the metal/solution interface causing the formation of an electrical double layer, which results in a halt in current flow. As the potential becomes more negative, peaks start to appear due to the adsorption of hydrogen onto the surface, as electrons from the platinum reduce H^+ ions in solution. The size, shape and number of these peaks are dependent upon the crystal facets present at the surface[60]. This region of the voltammogram is known as the hydrogen under potential or hydride region[57]. As an electron from the working electron is required to reduce each adsorbed hydrogen atom that forms the monolayer, the charge passed in this region can be used to estimate the surface area of the sample. The electro-active surface area, S, of an electrode can be found by,

$$\mathrm{S} = \frac{(\mathrm{C}_1 + \mathrm{C}_2)/2}{2.1 \times 10^{-4}}$$

where C_1 and C_2 are the total charge passed in the hydride region in the forward and reverse scans and $2.1\text{x}10^{-4}$ C cm^{-2} was taken as the hydrogen adsorption charge density[61]. This charge conversion factor is experimentally determined and only provides an estimate of the actual surface area, as there are multiple possible configurations of binding for hydrogen on a platinum surface leading to variations in surface packing[57]. Using this surface area (S) and the mass as determined by amperometry (m), it is possible to determine the specific surface area,

$$\sigma_{\mathrm{m}} = \frac{\mathrm{S}}{\mathrm{m}}$$

where σ_m is measured in m^2/g.

2.2 SMALL ANGLE X-RAY SCATTERING

Small angle X-ray scattering is a powerful technique, used in order probe the morphology of nanostructured materials. Diffraction of the rays follows Bragg's law,

$$\mathrm{n}\lambda = 2\mathrm{d}_{\mathrm{hkl}}\sin\theta$$

where n is the diffraction order, λ is the wavelength and d_{hkl} is the distance between lattice planes. Constructive interference will occur at positions that satisfy this relation and regular repeating structures in a sample will lead to a diffraction pattern. This pattern follows Bragg's law and (Bragg) peaks are observed at the angles where Bragg's law is conserved. For a cubic structure, the interplanar distance between the two closest lattice planes with same Miller indices is found using,

$$d_{hkl} = \frac{a}{\sqrt{h^2 + k^2 + l^2}}$$

where a is the lattice parameter and h, k and l are the Miller indices, which mathematically describe the position of a family of planes within the unit cell of a given crystal[62].

SAXS measurements can be used in order to determine the morphology of the individual unit cell making up a structure. Crystallographic space groups are used in order to describe unit cells of structures in three dimensions; these symmetry groups detail the repeating inhomogeneities in electron density and thus provide a prediction for the expected Bragg peaks from a scattering experiment. Table 2.1 lists the structures described in this text with the space group and expected Bragg peaks[9]. For lipid mesophases, it is possible to identify the symmetry and therefore the lyotropic liquid crystalline phase in addition to the lattice parameter from these measurements.

Table 2.1. List of structures discussed in this thesis with corresponding space groups, characteristic Bragg peaks and Miller indices[12,45].

STRUCTURE	SPACE GROUP	BRAGG PEAKS	MILLER INDICES (HKL)
DOUBLE DIAMOND (Q_{II}^{D})	Pn3m	√2, √3, √4, √6, √8, √9	110, 111, 200, 211, 220, 221
SINGLE DIAMOND	Fd3m	√3, √8, √11, √12	111, 220, 311, 222
GYROID (Q_{II}^{G})	Ia3d	√6, √8, √14, √16	211, 220, 321, 400
HEXAGONAL (H_{II})	NA	√1, √3, √4,	10, 11, 20
LAMELLAR (L_{A})	NA	1, 2, 3	1, 2, 3

In addition to providing information on the morphology of the individual components making up a repetitive structure, SAXS can also be used to measure the relative orientation of unit cells within a structure. A polydomain sample will result in scattering of even intensity around the beam centre, known as Debye Scherrer rings, as shown in Figure 2.3. Conversely, an orientated single crystal-like structure will produce a specific pattern of dots relative to the orientation of the sample to the beam[63].

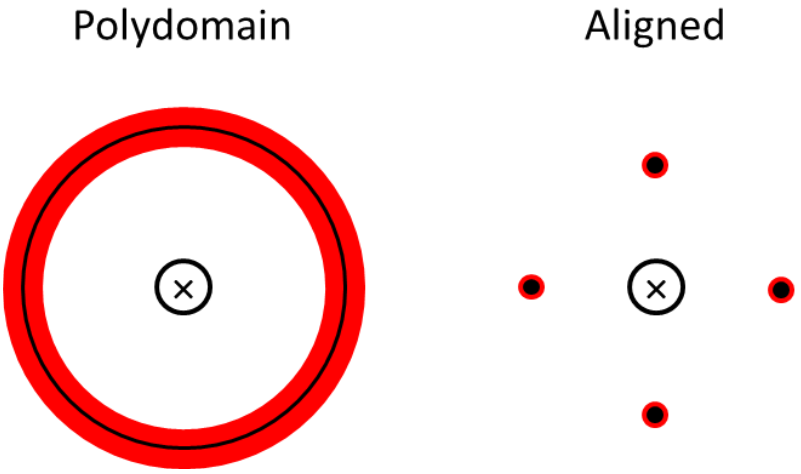

Figure 2.3. X-ray scattering patterns observed for poly-domain and aligned nanostructured samples, where x marks the beam centre.

The diffraction patterns produced by polydomain and aligned samples can be explained by the Ewald sphere construction. This surface, shown in 2D in Figure 2.4, maps where the scattering condition is satisfied. This allows for the observed scattering patterns measured in real space to be related back to the reciprocal space, which represents the crystal lattice of the sample. The Ewald sphere has a radius of 1/λ with the sample at the centre. The origin of the samples reciprocal lattice lies in the direct beam at the edge of the sphere. This reciprocal lattice is the Fourier transform of the real space crystal lattice. Diffraction spots will occur when the Bragg condition is satisfied, as is the case when the Ewald sphere intersects a point on the reciprocal lattice. A spot pattern is produced for single crystal samples where the entire lattice is aligned. The reciprocal lattice moves with respect to the sample, so that if the sample is rotated so too is the lattice. This gives rise to the circular diffraction patterns observed from polydomain samples. Within a single polydomain sample, many domains are located with no preferential alignment. Thus, virtually all orientations will be represented, meaning that lattice points will intersect the Ewald sphere at all angles. This results in a spherical diffraction pattern on the detector.

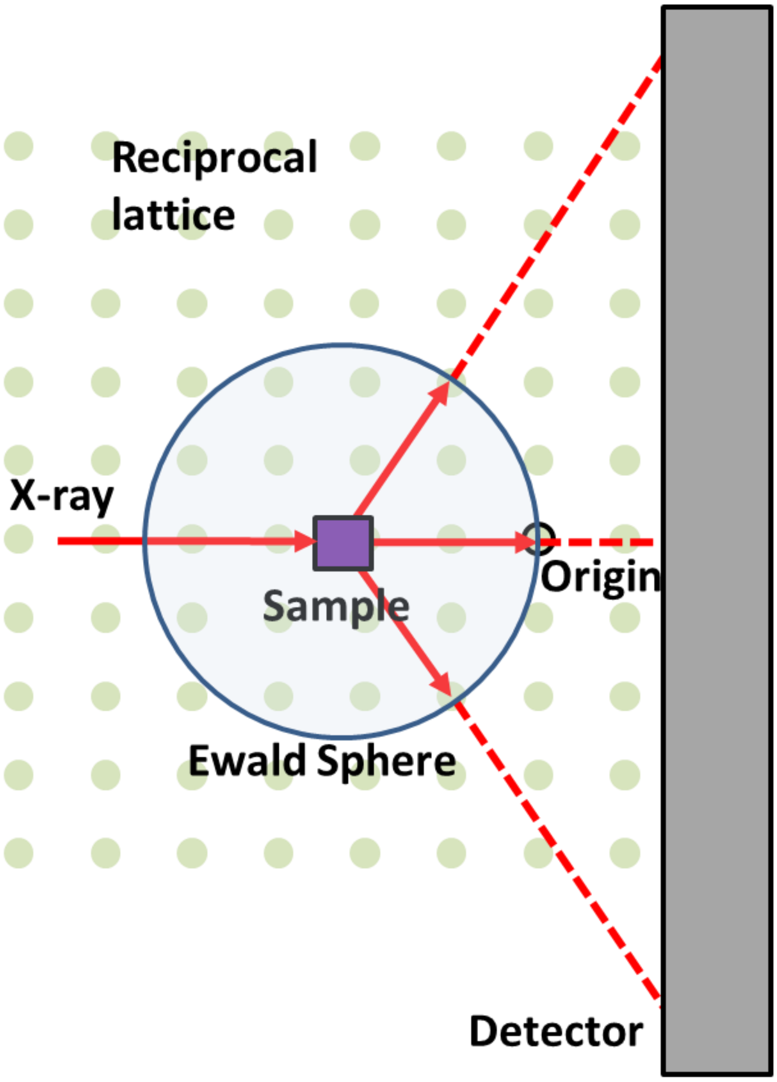

Figure 2.4. The Ewald Sphere projection in 2D where the green dots represent the reciprocal lattice of the sample.

Samples are measured in transmission, meaning that substrates used must be able to let X-rays through, being either X-ray transparent or low absorbance and physically thin; it is possible to investigate both solid and liquid materials if transmission can occur. The basic set up involves X-rays being produced by an electron gun and sent through a collimator producing a very narrow beam. The beam is then sent through the sample causing some X-rays to scatter, due to electron density inhomogeneities in the sample, and some of the beam to travel straight through. A beam stop is used to remove signal from the main beam, leaving the detector to measure solely the scattered radiation. The Bragg peaks will show up as bright rings or spots in the 2D image; these 2D images can then be radially integrated giving a 1D profile of the scattering. However, this does lose any orientational information contained in the 2D image.

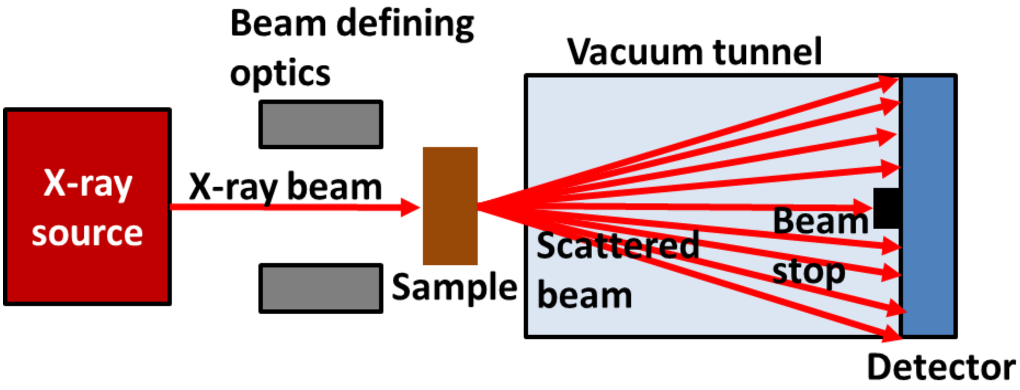

Figure 2.5. Schematic of a SAXS experimental set-up.

SAXS experiments are often performed at a synchrotron X-ray source, which provides several advantages over conventional laboratory sources. For the experiments described in this thesis, the greatly enhanced flux of synchrotron sources allowed for time resolved studies to be performed, as images can be resolved much faster than possible in a lab. In addition, synchrotron sources feature tuneable wavelengths, allowing for selection of wavelengths below the absorption bands of platinum, important for the SAXS studies of platinum nanostructure growth.

2.3 GRAZING INCIDENCE SMALL ANGLE X-RAY SCATTERING

Grazing incidence small angle X-ray scattering (GISAXS) is a scattering technique used in order to measure thin films and surfaces at nanoscale dimensions. A variation on SAXS, which utilises the reflection geometry rather than transmission; GISAXS combines the small length scales of SAXS with the surface sensitivity of grazing incidence reflection[64]. This removes sample limitations found in conventional transmission mode SAXS.

Setting the angle of incidence (θ – Figure 2.6) to approach the critical angle of the material under analysis allows for diffraction and reflectivity information to be collected in addition to scattering data[65]. However, for all GISAXS experiments described in the thesis, the experimental geometry was set so that only scattering data was observed; thus, all GISAXS work can be thought of as simply an additional geometry for SAXS experiments.

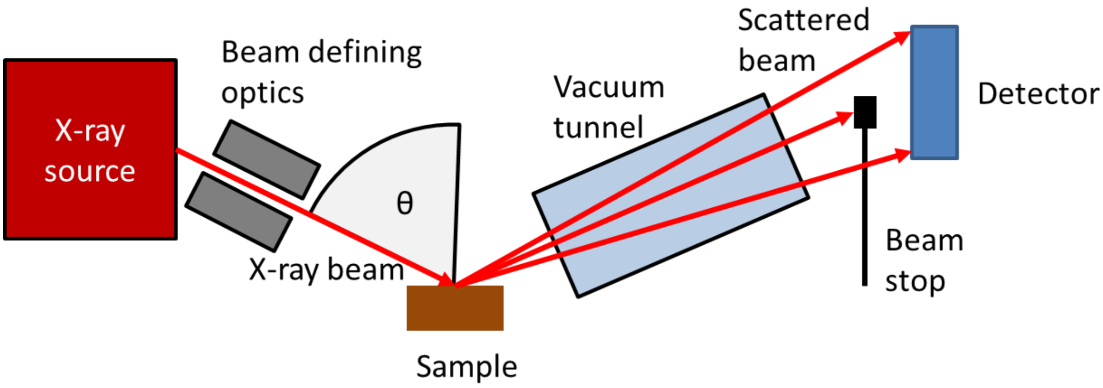

Figure 2.6. Schematic of a GISAXS experimental setup.

2.4 SPECTROSCOPIC ELLIPSOMETRY

Spectroscopic ellipsometry is an optical measurement technique used in order to determine the thickness of a thin film by measuring the change in linearly polarised light reflected off a sample. This reflection often causes the light to become elliptically polarised, which is where ellipsometry draws its name from[66]. The experimental set up for an ellipsometry measurement is shown in Figure 2.7, where a light source and polariser are used to produce a linearly polarised beam of light with a tuneable wavelength. The beam is reflected off the sample and the circularly polarised reflection is sent through another polariser and onto the detector.

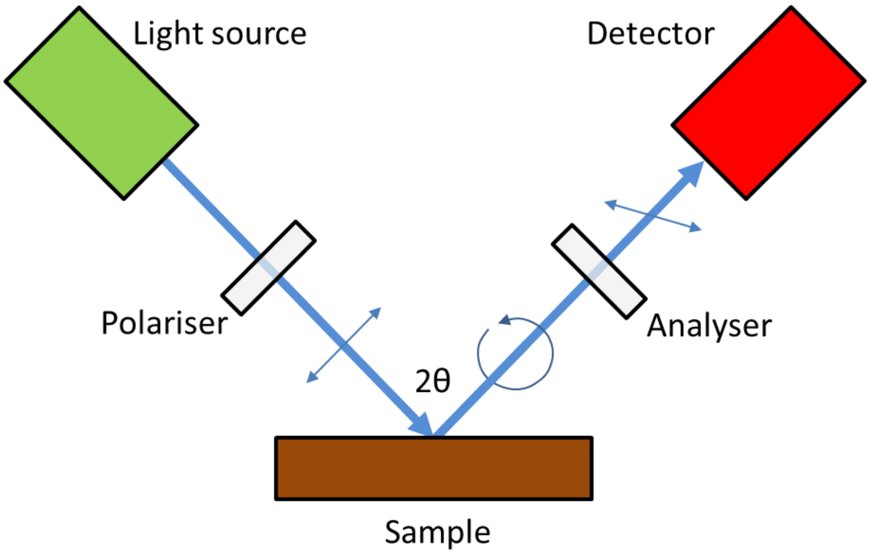

Figure 2.7. Schematic of an experimental set-up for ellipsometry measurements.

Two components of the reflected light are measured; the phase shift angle, Δ and the amplitude ratio between the p and s polarized waves, Ψ. In spectroscopic ellipsometry, the wavelength incident light is varied typically in the ultra violet and visible range, producing a spectrum for Δ and Ψ. The main advantages of this technique are high sensitivity (~0.1 Å)[67] and that it is non-destructive, unlike Profilometer methods. A disadvantage, however, is that it is an indirect measurement of the films thickness; Δ and Ψ spectra are recorded, then a model must be produced and fitted to the data in order to provide an estimate for the thickness, requiring knowledge of the refractive index values. It also produces a low spatial resolution of typically a few millimetres, limited by the size of the incident beam.

Figure 2.8 shows the model used for fitting ellipsometry data in this thesis, which features three layers: air, thin film and substrate and thus two interfaces: air/film and film/substrate. The model uses the complex refractive index of each layer (N_0, N_1 and N_2) as well the thickness of the film (d) and angle of incidence (θ_0), in order to predict Δ and Ψ spectra.

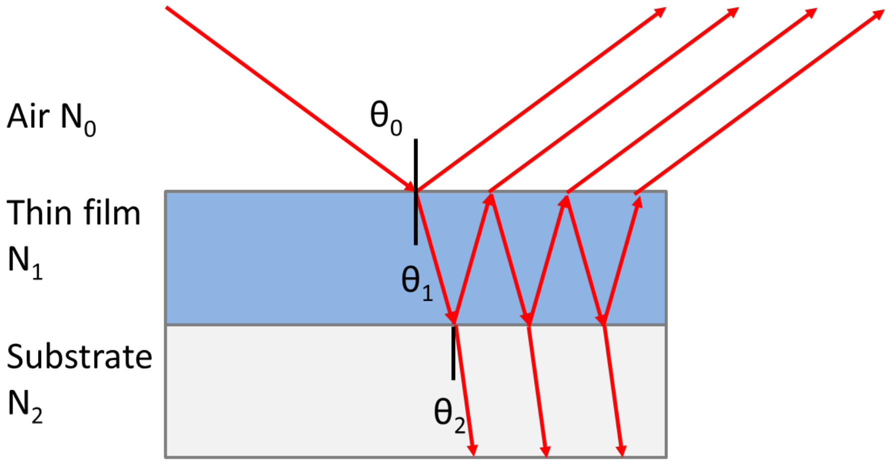

Figure 2.8. Schematic of the model used for ellipsometry measurement of a thin lipid film on a substrate.

The polarisation change in the reflected beam is due to both reflections from the two interfaces the interference effects from various beams combining again after exiting the film. The refraction occurring at the interfaces is described by the Fresnal equations, which take complex refractive index of material to give the amplitude reflection coefficient, r[68],

$$r_{jk,p} = \frac{N_k \cos\theta_j - N_j \cos\theta_k}{N_k \cos\theta_j + N_j \cos\theta_k} \qquad r_{jk,s} = \frac{N_j \cos\theta_j - N_k \cos\theta_k}{N_j \cos\theta_j + N_k \cos\theta_k}$$

here j and k are both different interfaces, θ is the angle of incidence and N is the complex refractive index. The phase interference effects are described by the film phase thickness, β. Refraction will occur to the incident beam at the first interface (air/film), which causes some of the beam to be transmitted (secondary beam) and some to be reflected (primary beam). A proportion of the transmitted beam will then be reflected at the film/substrate interface, where again a proportion of this will be transmitted through the air/film interface allowing interference to occur with the primary beam. Each beam will be at a different phase dependent upon the distance it has travelled and the refractive index of the mediums. The amount of interference that occurs is dependent upon total difference between the phase variation that has occurred in the primary and secondary beam. The film phase thickness, β, quantifies the amount that the phase varies due to the beam traveling through the film and is given by[68],

$$\beta = \frac{2\pi d}{\lambda} N_1 \cos\theta$$

here d is film thickness, λ is wavelength and θ is the angle of incidence. From these equations it is possible to find the amplitude reflection coefficient, describing both the interface reflections and inference effects arising from both p and s polarisations[67],

$$r_{012,p} = \frac{r_{01,p} + r_{12,p}\exp(-i2\beta)}{1 + r_{01,p}r_{12,p}\exp(-i2\beta)}$$

$$r_{012,s} = \frac{r_{01,s} + r_{12,s}\exp(-i2\beta)}{1 + r_{01,s}r_{12,s}\exp(-i2\beta)}$$

Ψ and Δ can then be found using[66],

$$tan(\psi) = \frac{|r_{012,p}|}{|r_{012,s}|}$$

$$tan(\psi)e^{i\Delta} = \frac{r_{012,p}}{r_{012,s}}$$

The simulated and experimental values for Ψ and Δ can then be plotted against wavelengths. The model value for film thicknesses, d, can then be varied in order to minimise the difference between experimental and predicted values to provide an estimate of film thickness.

2.5 ELECTRON MICROSCOPY

Electron microscopy techniques allow for direct imaging of a surface or structure at nanometre resolution. Throughout this thesis scanning and transmission electron microscopy (SEM and TEM respectively) are used to characterise platinum nanostructures. Both techniques use a focused electron beam in order to image the samples. When an electron beam is incident to a sample, interactions between electrons and the surface generate the emission of secondary electrons, backscattered electrons and X-rays as shown in Figure 2.9[69]. In SEM measurements, information from these processes is used for imaging. Typically, it is the secondary electrons measured by a detector on the microscope that are used to image the surface topology of the sample. X-rays emitted from the surface have an energy characteristic of the ionisation energy of the incident element, and thus can be used to identify the composition of a materials surface in a technique known as energy dispersive X-ray spectroscopy (EDX)[70].

The electrons that are not scattered or absorbed are transmitted through the sample with intensity proportional to the sample electron density. These transmitted electrons are used in TEM imaging, an analogue to optical microscopy with electrons replacing photons. TEM is able to achieve greater resolutions than is possible with SEM measurements; resolution of around 1 nm is possible with TEM and around 10 nm for SEM[71].

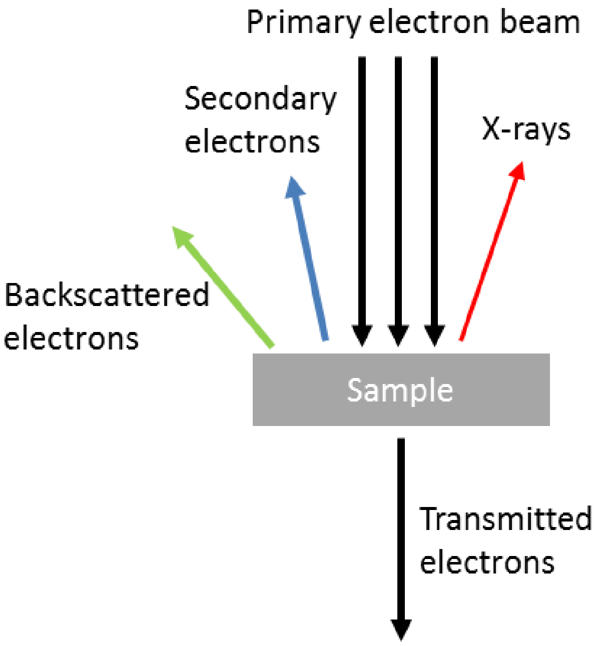

Figure 2.9. Summary of the processes in electron microscopy.

The nature of each technique leads to a different restriction on sample format. For SEM measurements, the surface of a sample must be conductive in order to avoid a build-up of charge. Typically, non-conductive samples are coated in gold in order to overcome this issue; this was not required within the experiments described as only conductive platinum samples were imaged. Transmission electron microscopy relies on the transmitted electron beam in order to image this sample. This means that the sample is required to be physically extremely thin, hundreds of nanometres at most; because of this sample preparation can be very complex, when compared to the requirements for SEM studies.

3 A GISAXS STUDY OF THIN LIPID FILMS: PREVENTING DEHYDRATION THROUGH THE ADDITION OF GLYCEROL AND INTERFACIAL DRIVEN ORIENTATION.

3.1 INTRODUCTION

This chapter describes an investigation into thin lipid films in a controlled humidity environment; the additional of glycerol is demonstrated to controllably lower the humidity for Q_{II} phases to form, which allowed for a study into the interface induced alignment of these structures.

Lipid films are experimentally difficult to investigate in an open environment due to their tendency to dry out, unless exposed to air approaching saturation. In the first part of this chapter it is demonstrated experimentally and theoretically that adding glycerol controllably lowers the humidity at which cubic phases form. These results facilitate the study of lipid films in a humidity controlled environment and broaden the potential applications of cubic phases, whilst also opening up the potential of new humidity-responsive nanomaterials.

Typically Q_{II} phases are studied either at a fixed water:lipid ratio in a sealed cell[72,73], or else dispersed or submerged in aqueous surroundings[74–77] where they adopt an "excess water" structure, usually a Q_{II}^{D} phase[12,72,73]. This is because in an open environment (i.e. in contact with air or other gases), dehydration will reduce the lattice parameter and ultimately cause phase transitions from Q_{II}^{D} to Q_{II}^{G} and then to lower hydration structures, such as the fluid lamellar (L_{α}) or the inverse micellar (L_{II})[76]. Maintaining sample hydration is also an issue for existing procedures and applications using Q_{II} phases, such as membrane protein crystallisation and crystallography, especially using the recently developed serial femtosecond approach[21], topical drug delivery[25], ion conductance[33] and sample preparation for cryoTEM[78].

Several groups have reported studies of Q_{II} phases in a controlled humidity gaseous environment, assessing the structure optically[79] as well as by X-ray scattering[33,76] on micron sized droplets or thin films. In these experiments, humidity provides precise control over the lattice parameter and lipid mesophase, allowing for both kinetic and equilibrium properties of the Q_{II} phases to be studied. The main disadvantage of using humidity control is that Q_{II} phases require a high relative humidity (RH) in order to remain stable; for example above 90% is needed in monoolein[76], which is difficult to achieve and measure practically[76,80] .

In this chapter, it is demonstrated that the addition of glycerol to thin lipid films will produce samples that spontaneously adopt and maintain cubic phase nanostructures, when exposed to RH values consistent with typical laboratory or outdoor values. Without significantly affecting the cubic phase structure, a Q_{II} phase was observed down to RH = 16%, which allows investigation at a more practically manageable level of humidity in a laboratory. Additionally, this is of use for other applications requiring a Q_{II} phase in an open environment at a typical ambient humidity.

Further value of this work lies in the production of a new class of smart humidity-responsive materials. Responsive systems have already been reported where the formation and/or lattice parameter of a cubic phase responds to changes in ionic strength[81], pH[28], temperature[29–31] and enzymatic lipolysis[23]. Alterations in these conditions change the diffusion properties of each material and these previous examples were investigated for applicability in controlled or triggered drug release. Here, a new class of responsive cubic phase is demonstrated, whereby humidity can dictate cubic phase formation depending on glycerol content. This varying glycerol content permits control over the lower humidity threshold at which cubic phases form. Additionally, accurate modelling of this relationship is shown, allowing for development of tuneable humidity-responsive materials with applications in triggered aroma release[34,82] or sensor technologies.

In the second part of this chapter, the orientation adopted by thin films of Q_{II} phase is studied. Typically, in bulk, lipid cubic phases are polydomain with no particular orientation; however, there are several reasons why it is advantageous to form an oriented single-domain structure. Firstly, orientated Q_{II} phase samples provide additional information to polydomain analogues when studying phase change pathways[77]. Moreover, orientated lipid films may allow for the production of orientated metal structures when used as a template; single domain bicontinuous structures have been shown to feature exotic opto-electronic properties[83,84], such as negative refractive index. Another application of Q_{II} phases is in drug or flavour delivery, whereby diffusion of these molecules in and out of the lipid would likely depend upon the nature of the interface[85]. Through the addition of glycerol, it was possible to study thin films of Q_{II} phase under controlled humidity, without requiring levels of humidity approaching saturation. Films of phytantriol and 20% glycerol produced by spin-coating were observed to consistently form uniaxially aligned structures across a range of thicknesses, between 540 ± 10 and 1440 ± 10 nm. The observed orientation of the Q_{II}^G and Q_{II}^D phases was found to agree with theoretical predictions based upon the minimization of energy at the air/lipid interface[2]. These results demonstrate spin-coating as a robust and procedurally simple method to produce uniaxially orientated films, beneficial to the study of cubic phases and which may have applications in the deposition of orientated nanostructured metals. Finally, this study will be of value to any application of Q_{II} phases involving the diffusion of molecules, such as biosensors[32] or drug delivery techniques[86], which will be highly dependent upon the nature of the interface formed.

3.1 EXPERIMENTAL

All compounds were used as received. Phytantriol (3,7,11,15-tetramethyl-1,2,3-hexadecanetriol) was received as a gift from Adina Cosmetic Ingredients (UK). Rylo 19^{TM}, an industrial form of monoolein (2,3-dihydroxypropyl (Z)-octadec-9-enoate)[87], was a gift from Danisco (UK). Glycerol (propane-1,2,3-triol) was purchased from Sigma Aldrich (UK).

Lipid (phytantriol or Rylo)/ethanol and glycerol/ethanol solutions were prepared at 80% (w/w) ethanol with heating at 50 °C to assist in dissolution. On cooling, the glycerol and lipid solutions were combined in different ratios to produce mixtures that were all 80% (w/w) ethanol, and which, following ethanol evaporation during spin-coating, had concentrations of (0%, 5%, 10%, 20%, 25%) glycerol to phytantriol or (0%, 20%, 40%) (w/w) glycerol to Rylo respectively. Round silicon wafers (diameter = 2 cm) were made hydrophobic as described by Rittman et al:[12]. The wafers of silicon were cleaned in piranha solution, dried, and placed in a solution of toluene (50 ml), octyltrichlorosilane (0.2 mL) and triethylamine (0.3 mL) and left overnight. Finally, wafers were rinsed with toluene and ethanol and left to dry in air.

For the spin-coating, 100 µl of lipid/glycerol/ethanol solution was deposited onto wafers by spin-coating at speeds of 1, 5 and 10 kRPM over 40 s. This was sufficient time for the ethanol to evaporate, by visual inspection (the films were colored, due to interference, and color changes were observed during ethanol evaporation). Ethanol (100 µl) was applied to the wafer edge during a second 30 s rotation at 5 kRPM in order to remove excess buildup of solution at the edges of the disc. Finally, discs were left in air for half an hour before analysis.

Once prepared, a Brewster Angle Microscope spectroscopic ellipsometer was used to estimate the thickness of the films at ambient humidity (approx. RH = 50%). Measurements of the angles Delta (Δ, the phase shift between incident and reflected beam) and Psi (ψ, the amplitude ratio between the p and s polarized waves in the reflected beam) were performed with the angle of incidence set to 75° over the wavelengths 350 – 1000 nm.

Grazing incidence small-angle X-ray scattering (GISAXS) measurements were performed at beamline I07 at Diamond Light Source using a beam size of 300 µm x 500 µm with energy of 12.5 KeV. A Pilatus 100K detector was used to collect data over a q range of 0.01 $Å^{-1}$ to 0.50 $Å^{-1}$. A sample of silver behenate was used as a calibrant in order to measure the sample to detector distance and beam center. A vertical rod was used as a beamstop to block the direct and reflected beams.

The samples were contained within a controlled-humidity cell (183 mm diameter, ~ 2.5 L) with polyimide walls to allow for X-ray transmission. The RH was controlled over a range of 10% to 97% using a combination of hydrating sources (water-soaked tissue paper and/or pipe cleaners) and a variable dry helium line-in; a handheld Vaisala HM70 humidity sensor (factory calibration, ± 0.6% RH at 0 – 40% RH and ± 1% RH at 40 – 97% RH) was placed near the sample in the chamber to monitor humidity. GISAXS images of 1 s exposure were taken regularly as the humidity of the sample environment was varied. A schematic of the experimental set-up is shown in Figure 3.1.

Two-dimensional GISAXS images were radially integrated over one quadrant using YAX[88,89], a custom macro that runs within the ImageJ software package. Phases were identified by assigning peaks measured to Bragg reflections for a given phase.

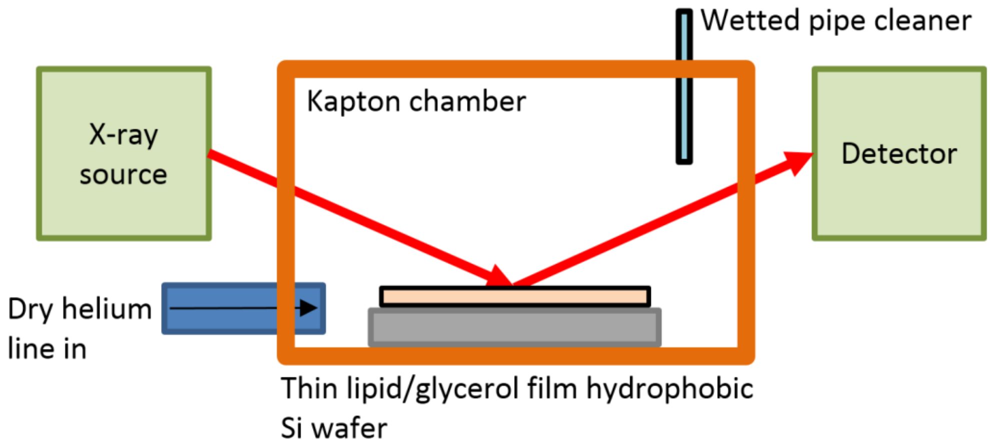

Figure 3.1. Schematic of an experimental GISAXS set-up.

3.2 RESULTS

3.2.1 Film Thickness Measurements

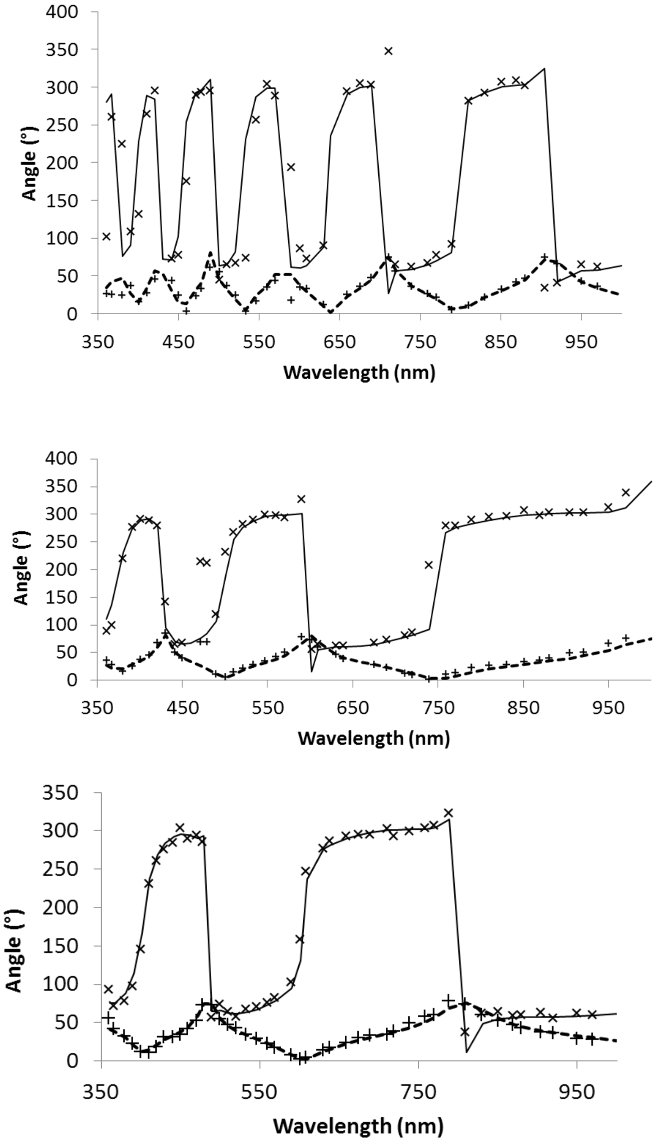

Thickness = 1440 ± 10 nm
Spin speed 1000 RPM

Thickness = 675 ± 10 nm
Spin speed 5000 RPM

Thickness = 540 ± 10 nm
Spin speed =10,000 RPM

Figure 3.2. Ellipsometric data from films prepared by spin-coating at three different speeds, producing films of different thickness. Solid and dotted lines represent simulated data, and × and + experimental data, for Δ and ψ respectively. All films were spun from a solution that was 80% w/w ethanol (20% phytantriol / glycerol). Top and bottom films were 20%:80% (w/w)

Lipid/glycerol films were produced on hydrophobic silicon wafers by spin-coating. These thin films were coloured due to interference effects and were observed to be homogeneous through visual inspection. Ellipsometry measurements were performed to estimate the thickness of the lipid/glycerol films at ambient humidity (RH ≈ 50%). 'ELLIPSHEET'[66] was used to simulate ψ and Δ where film thickness was found by minimizing the sum of the squares of the deviations between the simulated and measured data. For air n=1 and k =0; for phytantriol/glycerol films the refractive index was assumed to be n = 1.47[90,91] and k is also equal to zero. Silicon has a non-zero extinction coefficient and a complex refractive index which varies over wavelengths; at λ=360nm n =6.01 and k=2.91 and at λ=1000nm n=3.57 and k=0.00[92]. Representative experimental and simulated data is shown in Figure 3.2.

The reproducibility of this technique was demonstrated by preparing two samples in the same fashion, using an ethanol solution with 10% w/w lipids applied to the substrate at 10 kRPM. The sample thicknesses were estimated to be 234 nm and 237 nm. Whilst additional measurements would be needed to confirm this reproducibility to within the 10 nm range, it does indicate small margins of error in both the spin-coating and ellipsometry measurements combined.

3.2.2 Phase locations with respect to humidity phytantriol

GISAXS images of phytantriol/glycerol films were taken in series as the humidity was increased. The data were reduced and intensity profiles were plotted as stacked scatter plots with the y-axis intercept set to be proportional to the RH, as shown in Figure 3.3. This allowed for the emergence of the Q_{II}^{G} and Q_{II}^{D} phases to be clearly observed from characteristic peaks.

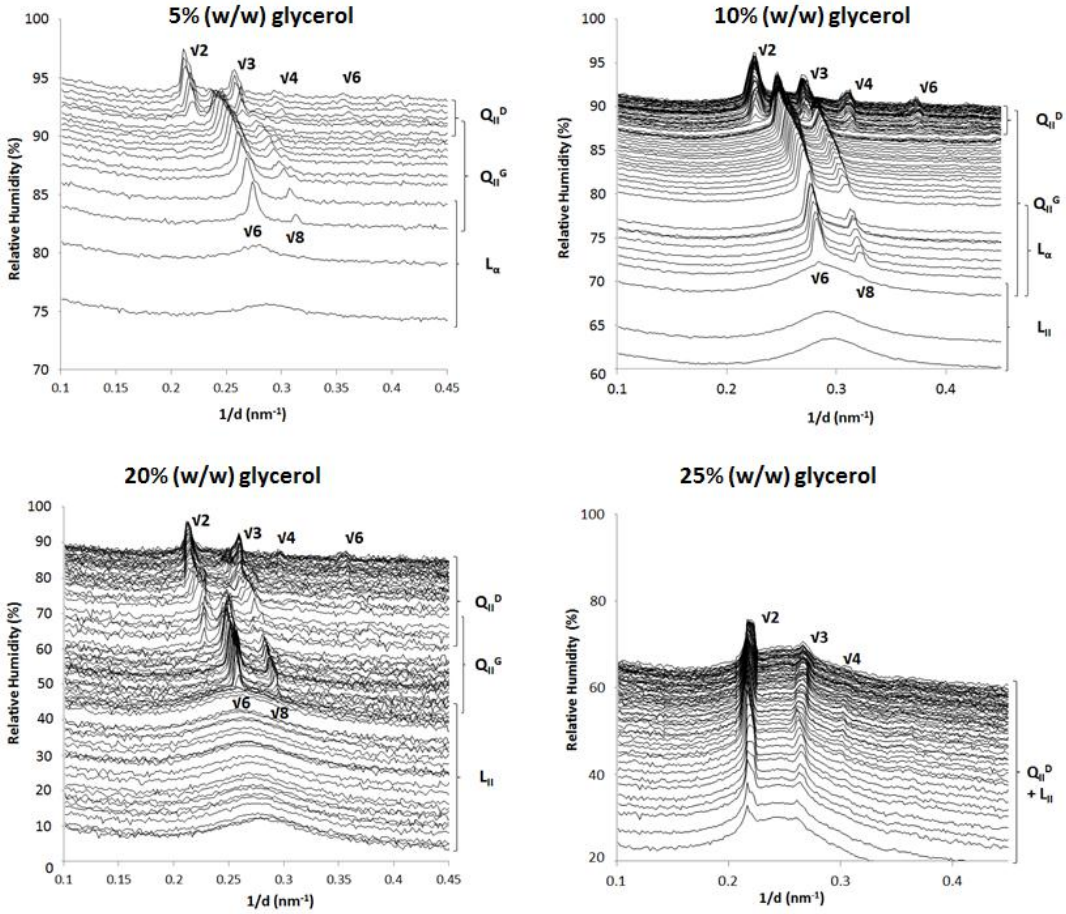

Figure 3.3. Stacked GISAXS intensity profiles for thin films of phytantriol and 5%, 10%, 20% and 25% glycerol.

The 2D images featured a relatively low level of mosaicity, observed as distinct dots rather than an arc; this indicates well-orientated lipid films, which will be discussed in section 3.2.8. Due to this orientation, the diffraction arcs from the L_{α} phase were difficult to include in the 1D data without also including the strong on-axis reflection from the main beam. Due to this, the appearance of the lamellar phase was deduced purely from the 2D images, as shown in Figure 3.4.

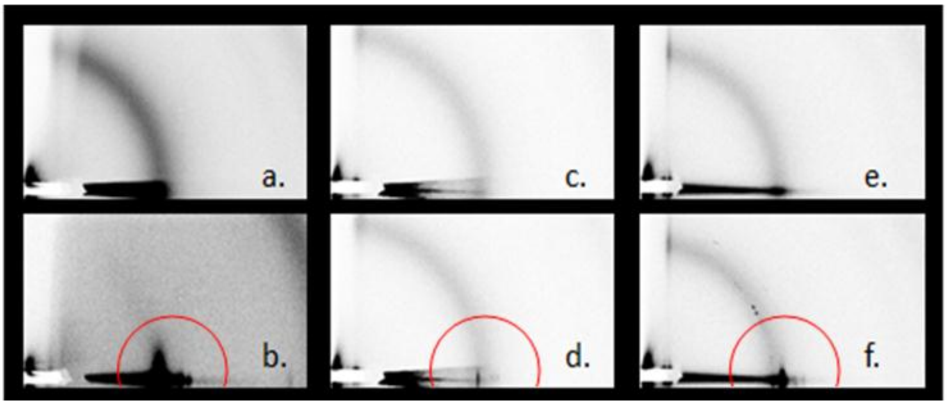

Figure 3.4. 2D GISAXS images showing appearance of the L_α phase. (a)-(b) show images of phytantriol film with no added glycerol, where the L_{II} phase is observed at RH = 92.8% (a) and the L_α phase forms at RH = 95.9% (b). Images (c)-(d) show a film of phytantriol with 5% (w/w) glycerol, where initially the L_{II} is observed at 82.7% (c) and at RH = 83.8% a coexistence of L_α and L_{II} can be observed (d). Images (e)-(f) show a film of phytantriol with 5% (w/w) glycerol, where the L_{II} phase is observed at RH = 65.8 (e) and the L_α phase is observed to appear at RH = 70% (f). A red circle has been added to images, b, d and f to label the L_{II} reflection.

A summary of the location of each observed phase with respect to RH is shown in Figure 3.5, with the exact values given in Table 3.1. The results clearly show that the appearance of each mesophase is seen to occur at lower RH values with increased glycerol content. Of particular note is phytantriol with 25% (w/w) glycerol, where the Q_{II}^D phase was observed across the entire measured humidity range down to RH = 24%. Measurements were stopped during hydration when either the lattice parameter of the Q_{II}^D phase appeared to be saturated (marked by a white dotted line), as no further phase change can be expected according to published phytantriol/water phase diagrams[12], or else the maximum achievable humidity (97%) was reached. The black dotted line on 5% and 10% glycerol also indicates where the controlled humidity measurement was halted; the location of the L_{II} phase below this was extrapolated from phase measurements upon bulk phytantriol/glycerol, which is assumed to be equivalent to a film at RH = 0%. The order in which phases appear on increasing RH agrees with previously published data[12,76], except at 20% glycerol concentration where the lamellar phase was not observed.

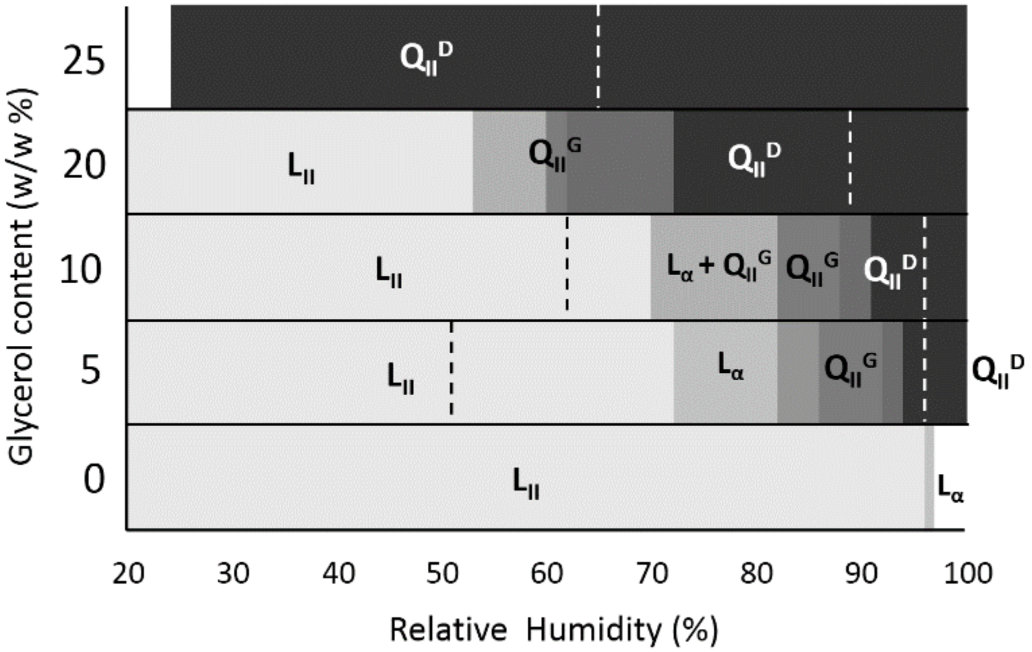

Figure 3.5. Identity and location of each phase with respect to RH within the phytantriol/glycerol systems. Unlabeled grey regions are occupied by a coexistence of the two neighboring phases. White dotted lines indicate the upper limit measured. Q_{II}^{D} phase occupation beyond this is assumed from previous literature[12]. Black dotted lines indicate the lower limit; the existence of the L_{II} phase below this was inferred from measurements upon bulk phytantriol/glycerol solution (an approximation for RH = 0%).

Table 3.1. Measured relative humidity values of phase boundaries in phytantriol/glycerol systems in order of increasing humidity.

Glycerol (%w/w)	L_{II} RH (%)	L_{α} RH (%)	Q_{II}^{G} RH (%)	Q_{II}^{D} RH (%)
0	12* - 96	96 – 97*	-	-
5	51* - 72	73 – 86	82† ± 1 - 94†	92† - 96*
10	62* - 70	70 – 82	70 - 91	88 – 96*
20	10* - 60 ± 5	-	53 ± 7 – 73 ± 1	63 ± 1 – 89*
25	-	-	-	24* - 65*

* Indicates where the measurement was halted and not where the phase was observed to appear/disappear. † Indicates that a duplicate value of >94.1% from a second wafer has been excluded.

In order to estimate the phase that a film of phytantriol and glycerol would form at, RH = 0% bulk un-hydrated samples of phytantriol/glycerol solution sealed in glass capillaries were measured using SAXS. SAXS measurements of both samples showed a broad ring, indicating that both 5% and 10% (w/w) glycerol and phytantriol samples had formed the L_{II} phase.

Two samples were measured with 5% glycerol and phytantriol, labelled wafer 1 and wafer 2. Table 3.2 lists the observed phase locations. Wafer 1 maintained a L_{α} phase to the maximum measured humidity of RH = 94% with no Q_{II} phases observed. This suggests that the lower humidity limits for the two Q_{II} phases were above this, higher than those measured in wafer 2. Because no actual value can be associated with these transitions, it was not possible to meaningfully take an average of the values for wafers 1 and 2, and therefore only presented the values of 84% and 92.5% for wafer 2 in Table 3.1. This is despite the fact that the average of the two values would have been significantly higher and would have given a better theoretical fit to the trend line shown later in Figure 3.11.

Table 3.2. Observed phase locations with respect to relative humidity for two samples of phytantriol with 5% glycerol.

Wafer	L_{II} RH (%)	L_α RH (%)	Q_{II}^G RH (%)	Q_{II}^D RH (%)
1	71.0* - 91.3	73.0 – 94.1*	-	-
2	-	76.0* - 86.0	84.0 – 94.0	92.5 – 96*

3.2.3 Phase locations with respect to humidity Rylo

Rylo/glycerol films were found to behave in a similar fashion to those of phytantriol/glycerol. For pure Rylo, the Q_{II}^G phase first appeared at RH = 93% and the Q_{II}^D phase was not observed to appear before the maximum humidity measured of RH = 96%, agreeing with observations by Rittman et al.[76]. With the addition of 20% w/w glycerol to Rylo, the Q_{II}^D phase was observed to form at RH = 57% and, with 40% w/w glycerol, the Q_{II}^D phase was found to occupy the entire measured range down to RH = 16%.

Curiously, the 20% glycerol data indicate the presence of an inverse hexagonal phase at lower RH% values. This was not seen in any other sample and, as only one data set was obtained for this sample, it cannot be stated whether it is reproducible. It is a possibility that this is an artefact induced by beam damage; however, as it disappears on increasing humidity and the sample adopts a Q_{II}^D phase of typical dimensions expected for an excess water phase formed from Rylo, this seems unlikely.

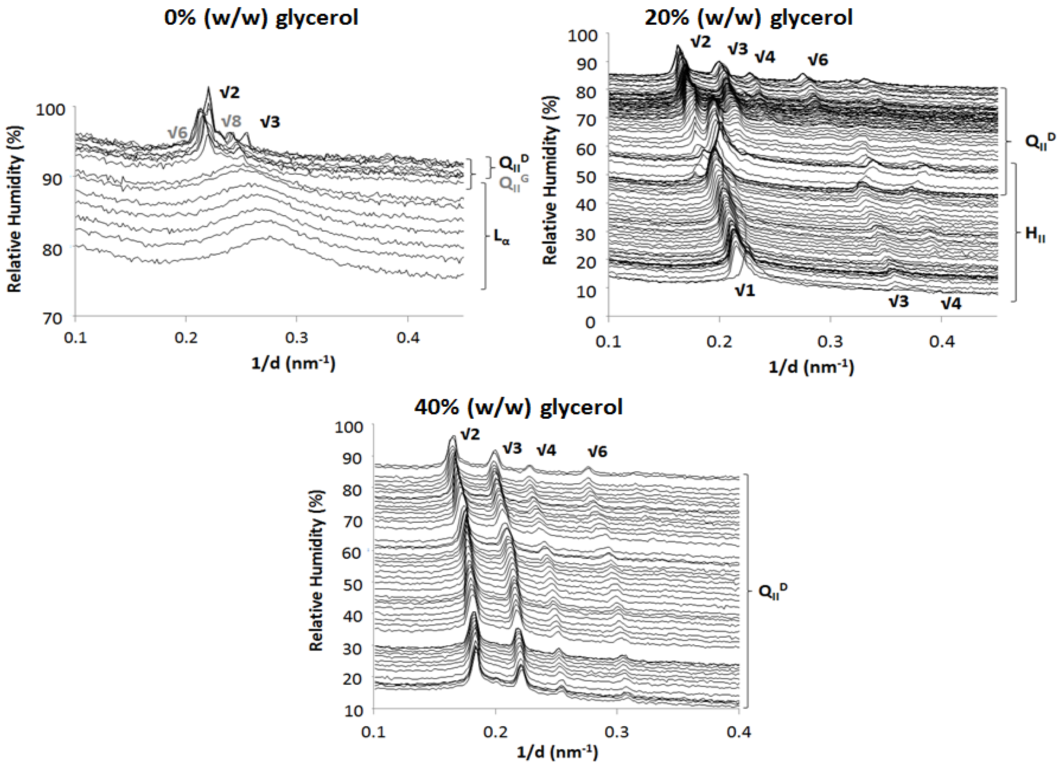

Figure 3.6. Stacked GISAXS intensity profiles for a thin film of Rylo with 0%, 20% and 40% (w/w) glycerol under increasing levels of humidity, plotted on a log scale. Mesophases with corresponding Bragg peaks are notated on the plot.

3.2.4 Lattice parameter vs. glycerol concentration

In order to investigate whether the phase structure was modified by the presence of glycerol, the lattice parameter for the saturated Q_{II}^{D} phase adopted under limiting high-humidity conditions was plotted at varying levels of glycerol concentration, as shown in Figure 3.7. For comparison, published lattice parameters of the saturated Q_{II} phase in phytantriol[12] and Rylo[76] have been plotted at 0% glycerol content. No significant variation in lattice parameter is observed as glycerol content is increased. This indicates that glycerol does not enter the bilayer or interact strongly with the lipid head-groups which would cause a shift in lattice parameter[93].

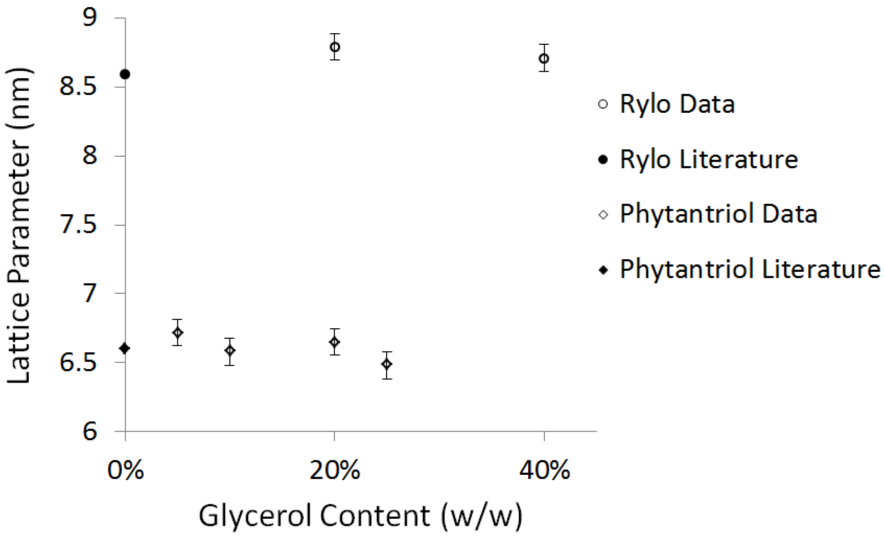

Figure 3.7. Lattice parameter of saturated Q_{II}^{D} phase of phytantriol/glycerol and Rylo/glycerol films plotted with previously reported literature lattice parameters[12,76].

3.2.5 Suppression of lamellar phase

In samples of phytantriol with 20% glycerol, the L_α phase was found to be suppressed. These samples were observed to form the L_{II} phase at low humidity and then transition to the Q_{II}^{G} phase, without displaying the L_α phase. Figure 3.8 shows a coexistence of the Q_{II}^{G} and L_{II} phases occurring during the transition (radial profiles shown in Figure 3.9). This coexistence proves that the L_α phase is indeed suppressed, and not simply missed experimentally as a result of having changed humidity too coarsely on going from L_{II} to Q_{II}^{G}. These findings suggest that the glycerol enters the cubic phase water channels and simply replaces the water with a water/glycerol mixture. The entropy of mixing lowers the chemical potential of the water in the cubic phase, thus lowering its vapor pressure (through Raoult's law), and effectively favouring water being kept within the cubic phase rather than evaporating into the surrounding vapor. This model gives a good quantitative description of the exact extent to which the addition of glycerol lowers the relative humidity at which cubic phases can form, shown later in section 3.2.7. This also explains why the lamellar phase is not observed as, according to measurements by Barauskas and Landh[12], the L_α phase is not observed below 89% (v/v) phytantriol (a cubic phase is formed instead) and the maximum lipid volume fraction for the 20% (w/w) glycerol sample is 84% (v/v), even containing no water. However, this does not explain why the micellar phase forms at lower hydration in the 20% (w/w) glycerol sample. The simple model whereby glycerol simply replaces an equivalent volume of water would suggest that, in the absence of water, the system would form a Q_{II}^G phase; the micellar phase in the corresponding phytantriol/water phase diagram only occurs at lipid volume fractions above 95% (v/v).

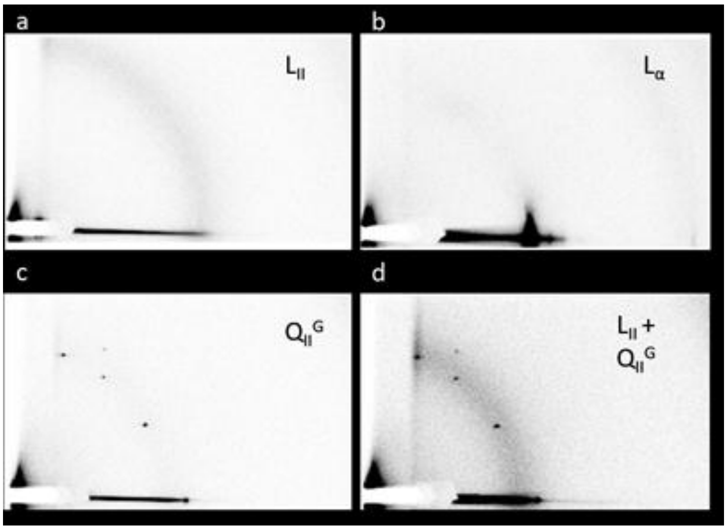

Figure 3.8. GISAXS images of phytantriol/glycerol films. Phytantriol and 5% w/w glycerol at RH = 54.2% (a) and RH = 92% (b) showing L_{II} and L_α phases respectively. Phytantriol with 20% w/w glycerol at RH = 34% showing Q_{II}^G phase (c) and RH = 45%, where a coexistence of L_{II} and Q_{II}^G phases was observed without the presence of a L_α (d).

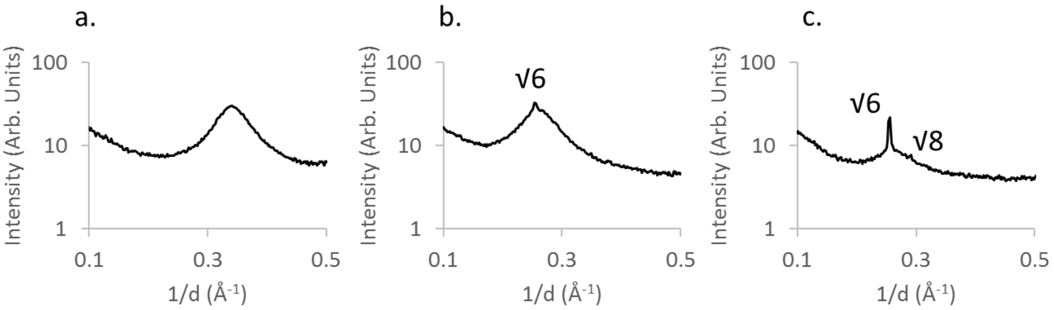

Figure 3.9. Radial profiles of phytantriol/glycerol films shown in Figure 3.8 with characteristic Bragg peaks noted. (a) Phytantriol and 5% w/w glycerol at RH = 54.2% showing a broad peak characteristic of an L_{II} phase. (b) Phytantriol with 20% w/w glycerol RH = 45%, where a coexistence of L_{II} and Q_{II}^G phases was observed without the presence of a L_α. (c) Phytantriol with 20% w/w glycerol at RH = 34% showing Q_{II}^G phase.

3.2.6 Lattice parameter vs. humidity

In order to show the reproducibility of the system, and thus changes in humidity were gradual enough for the lipid film to reach in equilibrium with its surroundings, a film of phytantriol with 20% glycerol was monitored under decreasing and then increasing humidity. Figure 3.10 shows the evolution of lattice parameter for the film as humidity is varied. Good agreement under both conditions demonstrates the reproducibility of the system, indicating that the data can be meaningfully fitted to thermodynamic models.

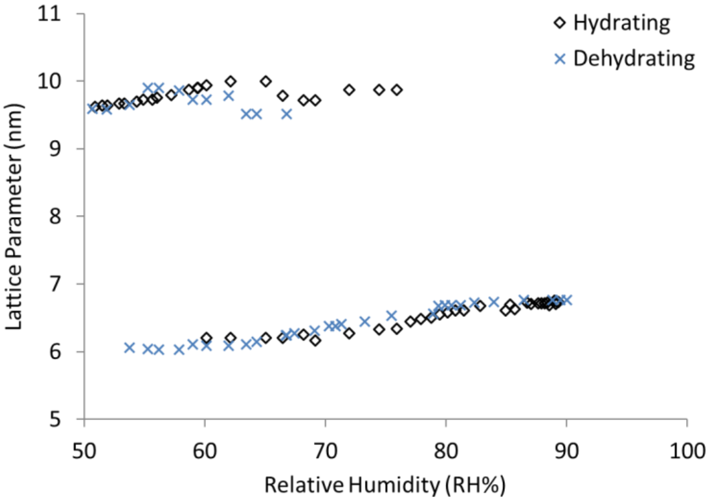

Figure 3.10. Lattice parameter values for a sample of phytantriol and 20% glycerol under increasing and then decreasing levels of humidity. Values between 9-10nm are for the Q_{II}^{G} phase and those between 6-7 nm are for the Q_{II}^{D} phase.

3.2.7 Simulating humidity boundaries

The phase boundaries for the phytantriol/glycerol/water vapor system were predicted by modelling the energetics as follows. For the system to be in equilibrium it is assumed that the chemical potential of the water inside the cubic phase (μ_W) plus the contribution to chemical potential from the bending energy of the lipid bilayer (μ_B) must be equal to the chemical potential of the water vapour (μ_V),

$$\mu_V(\mathrm{RH}) = \mu_W(x) + \mu_B$$

where μ_v varies with RH and μ_W varies with the mole fraction of water to glycerol inside the cubic phase, x. The bending energy, μ_B, of the lipid is assumed to be constant at phase transition because the lattice parameters at phase boundaries are consistent.

Measurements of PEG 6000 induced osmotic pressure on the cubic phase of phytantriol by Slaughter, shown in Table 3.3[94], were used to estimate the bending energy at the Q_{II}^{D}/Q_{II}^{G} and Q_{II}^{G}/L_{α} transitions.

Table 3.3. Mesophase observed in phytantriol/PEG 6000 samples measured in excess water conditions. Taken from work by Slaughter[94].

Grams of PEG per gram of solution (g)	Phase Observed
0.00	Diamond
0.05	Diamond
0.11	Gyroid
0.18	Gyroid
0.25	Gyroid
0.33	Gyroid
0.43	Gyroid / Lamellar
0.67	Lamellar

The amount of PEG 6000 required to cause phase transitions was equated to osmotic pressure, P (Pa), using the equation[95],

$$\mathrm{P} = -1.31\times10^{5}\mathrm{TG}^{2} + 141.8\times10^{56}\mathrm{G}^{2} + 4.05\times10^{5}\mathrm{G}$$

where G is grams of PEG 6000 per gram of water and T is the temperature (°C). The potential bending energy of the bilayer was then found by,

$$\mu_B = PV_w$$

where V_W is the molar volume of water (1.8×10^{-5} m^3). For the L_{II}/L_{α} transition the bending energy was estimated from data on humidified films without glycerol,

$$\mu_{\mathrm{B}} = \mathrm{RT}\ln\left(\frac{\mathrm{RH\%}}{100}\right)$$

where R is the gas constant and T is the temperature in Kelvin. RH% is the relative humidity that the lamellar phase was observed to form in our measurements of a pure phytantriol film; in this system, it is assumed the bending energy must equate to the chemical potential of water vapour. The chemical potential of water inside the cubic phase at phase transition (μ_w) varied with the mole fraction of water to glycerol in the cubic phase. The phytantriol/glycerol ratio is set for each sample; however, the ratio of glycerol to water varies as humidity increases, as the cubic phase takes on water.

In order to calculate the amount of moles of water inside the cubic phase at phase transition, the weight percentage of lipid to water at phase transitions, ($\%w/w_s$), was taken from measurements by Barauskus and Landh[12] and used to calculate the weight of lipid at phase transition,

$$\mathrm{m_s} = \left(\frac{\mathrm{m_l}}{100 - \%\mathrm{w/w_s}}\right)(\%\mathrm{w/w_s})$$

where m_s is the weight of solution at phase transition and m_l is the weight of the lipid. The total volume of water inside the cubic phase, V_w, was found by

$$V_w = V_s - V_G$$

where V_s is the total volume of the solution at the phase transition (found from m_s) and V_g is the volume of glycerol. The mole fraction of water inside the cubic phase was then calculated by,

$$x = \frac{\left(\frac{\mathrm{m_s} - \mathrm{m_g}}{\mathrm{M_w}}\right)}{\left(\frac{\mathrm{m_s} - \mathrm{m_g}}{\mathrm{M_w}}\right) + \left(\frac{\mathrm{m_g}}{\mathrm{M_G}}\right)}$$

where m_s is the weight of the solution at phase transition, m_g is the weight of glycerol, M_W is the molar weight of water and M_g is the molar weight of glycerol. This was used to estimate μ_W using $\mu_W = RT \ln x$. Finally, the phase boundaries were calculated by,

$$\mathrm{RH\%} = 100 \exp\left(\frac{\mu_V}{RT}\right)$$

where μ_v is the sum of μ_w and μ_B.

Figure 3.11 shows the predicted phase boundaries plotted with the observed first appearance of the pure Q_{II}^D, Q_{II}^G and L_{II} phases. The model shows good agreement with the measured data, indicating that the system behaves as hypothesised. This raises the possibility of responsive materials, where the exact humidity threshold desired can be chosen by using calculated glycerol content.

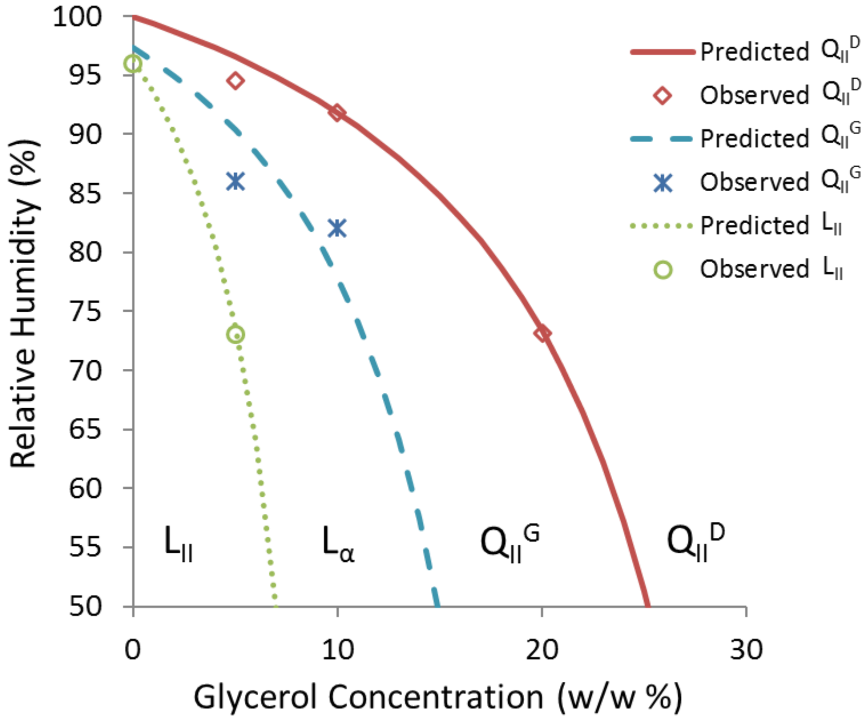

Figure 3.11. Lines show the predicted first appearance of each phase in a phytantriol/glycerol system, with points indicating the experimentally observed first appearance of each phase as humidity was increased.

3.2.8 2D GI-SAXS Images

As previously mentioned, the 2D GISAXS images of the Q_{II}^G and Q_{II}^D phases feature a relatively low level of mosaicity, indicating orientated films in the observed plane. This can be clearly observed in the GISAXS images in Figure 3.12.

GISAXS images were taken of films of phytantriol and 20% (w/w) glycerol under increasing humidity. The image of the Q_{II}^D phases was taken at RH = 90% and the Q_{II}^G phase was imaged at RH = 36%. In both cases, the spot pattern is ‘fibre averaged’ where one facet plane of the cubic phase is found consistently orientated parallel to the substrate. The orientation in both phases is confirmed by simulated scattering patterns, which have been superimposed onto the images and show good agreement between experimental and theoretical data. These simulations indicate that the Q_{II}^G phase is orientated with the (110) facet parallel to the substrate and, for the Q_{II}^D phase, the (111) facet is orientated parallel to the substrate.

Three phytantriol/glycerol films were tested of varying thicknesses and all displayed similar spot patterns, as shown in Figure 3.13. Film thickness was varied through speed of rotation during spin-coating with speeds of 1000, 5000 and 10,000 rpm producing films of thickness 1440 ± 10, 675 ± 50 and 540 ± 10 nm respectively.

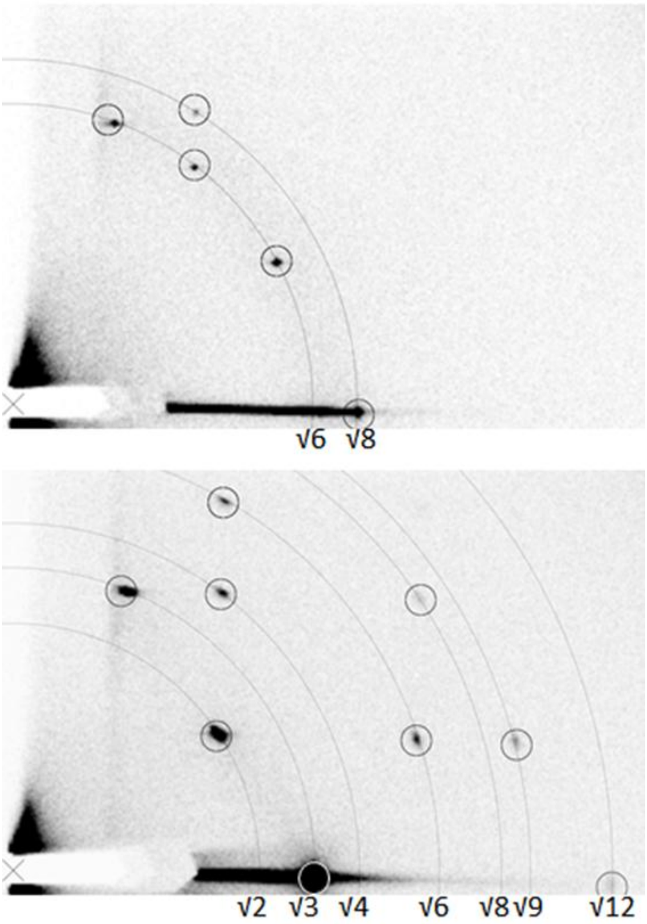

Figure 3.12. GISAXS images of phytantriol and 20% (w/w) glycerol films on hydrophobic silicon wafer at relative humidity = 36% (top) and 90% (bottom). Simulated spot patterns (small circles) are superimposed onto images for the Q_{II}^{G} (top) and Q_{II}^{D} (bottom) phases with the (110) and the (111) plane orientated parallel to the substrate respectively, together with partial rings to show where isotropic reflections would lie for different sets of (hkl) planes, with $\sqrt{(h^2 + k^2 + l^2)}$ values labelled. The beam centre is marked with an X near the bottom left of each image; the film is vertical as shown, and the substrate normal horizontal.

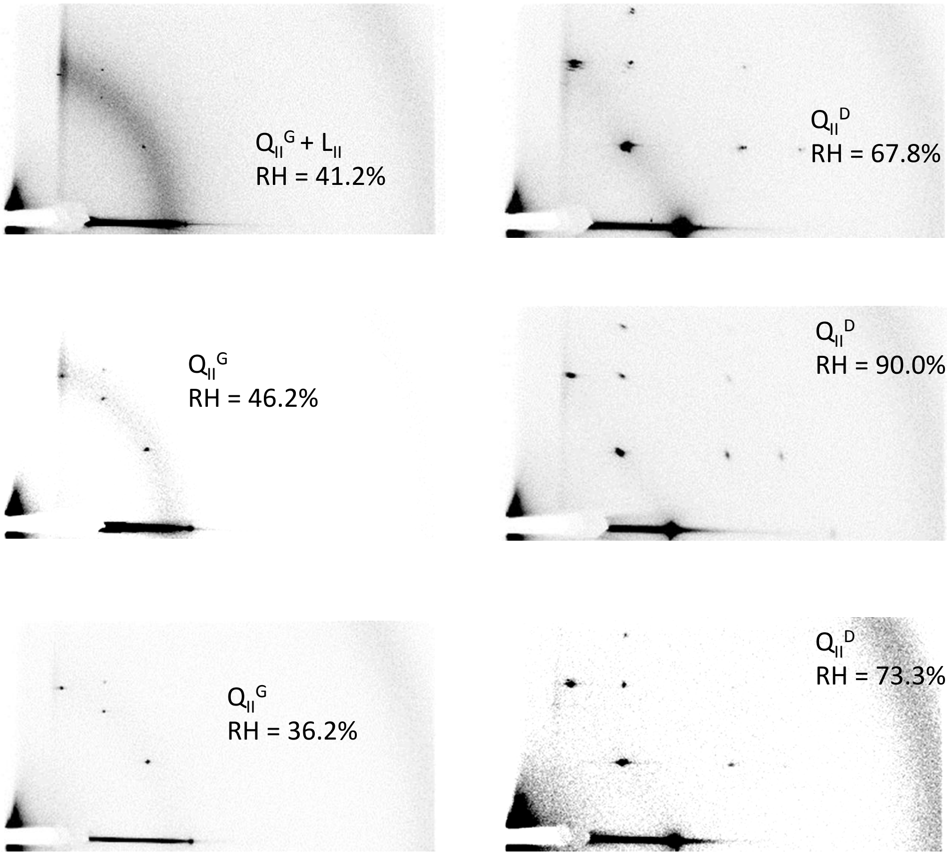

Figure 3.13. 2D GI-SAXS patterns from 20% glycerol / 80% phytantriol (w/w) films spin-cast at 1000 rpm (top), 5000 rpm (middle) and 10,000 rpm (bottom) with approximate thicknesses under ambient humidity of 1440 ± 10, 675 ± 50 and 540 ± 10 nm respectively. (For the top and bottom films, the thickness was determined by ellipsometry on the same sample; whereas for the middle film, where these data were not available, thickness was estimated from the mean of the thicknesses of three other films spin-coated from the same concentration of ethanol solution at the same speed.) Two GI-SAXS patterns are shown for each film, obtained at different levels of relative humidity (RH) to induce the formation of a Q_{II}^{G} phase (left) and a Q_{II}^{D} phase (right). In the top and bottom images, the Q_{II}^{G} phase shown was obtained in the humidifying direction (i.e. from the L_{II} phase), whilst in the middle image, the Q_{II}^{G} phase shown was obtained in the dehumidifying direction (i.e. from the Q_{II}^{D} phase).

Previously, it has been postulated that orientation of Q_{II} films may be due to an epitaxial relationship with the preceding orientated phase[96,97]. This hypothesis came from investigations where an orientated lamellar phase, with bilayers lying parallel to the substrate, was hydrated to form Q_{II} phase. Mechanisms for pathways between the L_α and Q_{II} phases and the Q_{II}^G and Q_{II}^D phases have been proposed, which suggest an epitaxial relationship is present. As an orientated Q_{II}^G phase is obtained, through hydration of an isotropic inverse micellar phase due to the suppression of the L_α phase, these results allow us to clearly rule out any such mechanisms for the Q_{II}^G phase. A coexistence of an L_{II} and Q_{II}^G is shown in Figure 3.8, demonstrating the formation of an orientated cubic phase from the non-orientated precursor. As the Q_{II}^D phase forms from an orientated Q_{II}^G phase, an epitaxial relationship between the two cannot be ruled out. Theoretical calculations based on minimising the lipid/air interfacial energy have predicted that the observed orientations are the most energetically stable facets[2], which suggests that the energetic stability is also a potential mechanism for the orientation adopted by the Q_{II} films.

3.3 SPOT PATTERN SIMULATION /AZIMUTHAL INTEGRATIONS

Simulated spot patterns were produced in order to confirm the orientation adopted by the lipid films, as shown in figure 3.12. The phase and lattice parameter of the sample are identified from the characteristic peaks shown in the 1D scattering profile. The d spacing, *d,* and the lattice parameter, *a,* are related to the Miller indices of the reflection, (*hkl*), by

$$\mathrm{d} = \frac{a}{\sqrt{h^2 + k^2 + l^2}}$$

The azimuthal angle, χ, between the uniaxial axis of rotation (horizontal on the images) and a given predicted spot is approximately given by

$$\cos(\chi) = \frac{[h^r k^r l^r] \cdot [hkl]}{|[h^r k^r l^r]||[hkl]|}$$

Where $[h^r k^r l^r]$ is the reflection being simulated and [*hkl*] is the uniaxial axis of rotation located parallel to the substrate normal ([111] for Q_{II}^D and [110] for Q_{II}^G). For each (hkl) reflection there are multiple {hkl} combinations that contribute to the scattering where |(hkl)|=|{hkl}| and for each of these {hkl} variation there are reflections with azimuthal angles ± χ. The distance in pixels of the spots from the centre was found by,

$$r = D \tan 2\theta$$

where *D* is the distance between the sample and detector in pixels and θ is taken from Bragg's law,

$$\theta = sin^{-1}\left(\frac{\lambda}{2d}\right)$$

where λ is the wavelength, in the same units as *d*. Spot positions in pixels were then given by,

$$x = rsin(\chi) + x_0$$

$$y = rcos(\chi) + y_0$$

where (x_0, y_0) are the pixel coordinates of the beam centre.

The approximation used is valid for scattering at the small angles with reflections occurring when the [hkl] direction is approaching the plane of the detector, perpendicular to the beam direction. The X-ray wavelength (0.99 Å) was small compared to the d spacing of the reflections (> 50 Å), so this approximation is reasonable. The predicted Azimuthal angles of the reflections in the 2D GISAXS images are listed in Table 3.4.

Table 3.4. Predicted Azimuthal angles for Q_{II}^{D} and Q_{II}^{G} phases. Highlighted points appear on 2D GISAXS images.

Diamond

Reflection $h^2+k^2+l^2$	χ (°)	Angle on Figure (°)
2	90	0
2	**35**	**55**
2	325	125
2	270	180
2	215	235
2	145	305
3	**71**	**19**
3	**0**	**90**
3	289	161
3	251	199
3	180	270
3	109	341
4	**55**	**35**
4	305	145
4	235	215
4	125	325
6	90	0
6	**62**	**28**
6	**19**	**71**
6	341	109
6	298	152
6	270	180
6	242	208
6	199	251
6	161	289
6	118	332
8	90	0
8	**35**	**55**
8	325	125
8	270	180
8	215	235
8	145	305
9	79	11
9	55	35
9	**16**	**74**
9	344	106
9	305	145
9	281	169
9	259	191
9	235	215
9	196	254
9	164	286
9	125	325
9	101	349
12	71	19
12	**0**	**90**
12	289	161
12	251	199
12	180	270
12	109	341

Gyroid

Reflection $h^2+k^2+l^2$	χ (°)	Angle on Figure (°)
6	90	0
6	**73**	**17**
6	**55**	**35**
6	**30**	**60**
6	330	120
6	305	145
6	287	163
6	287	163
6	270	180
6	253	197
6	235	215
6	210	240
6	210	240
6	150	300
6	125	325
6	107	343
8	90	0
8	**60**	**30**
8	**0**	**90**
8	300	150
8	270	180
8	240	210
8	180	270
8	120	330

3.4 CONCLUSIONS

These results demonstrate that adding glycerol progressively lowers the humidity at which Q_{II} phase films are stable, without affecting their lattice parameter. Furthermore, a thermodynamic model was used to explain the systems behaviour, allowing for the generation of predicted phase boundaries dependent upon glycerol content, which agree with observed data. With the addition of glycerol, it becomes possible to use Q_{II} phases in a much wider range of environments without the occurrence of dehydration. This effect will not be limited to glycerol and may also be observed in other polar liquids of high boiling point, such as ethylene glycol. This work will immediately benefit researchers using Q_{II} phases in cryo-TEM or membrane protein crystallization and allowed for the study of orientation in thin lipid films. Through the addition of glycerol, it was possible to study the orientation adopted by phytantriol/glycerol films. The Q_{II}^G and the Q_{II}^D phases were observed to be orientated, with the (110) and the (111) facet aligned parallel to the substrate respectively. This measurement was reproduced in films of varying thickness between 540 ± 10 and 1440 ± 10 nm and agreed with theoretical predictions based on the minimization of interfacial energy.

4 FABRICATION AND AN *IN SITU* X-RAY SCATTERING STUDY OF ALIGNED NANOSTRUCTURED PLATINUM FILMS

This chapter describes the production of nanostructured metal films 1-2 microns thick, featuring 3D-periodic 'single diamond' morphology and high out-of-plane alignment, with the (111) plane oriented parallel to the substrate. These films are produced by electrodeposition of platinum through a 'double diamond' lipid cubic phase template. Taking advantage of the differing symmetries featured in the template and deposit, this chapter also presents a time resolved SAXS measurement taken *in situ* as the platinum nanostructures grow within the lipid template. The *in situ* measurements were facilitated by the development of a new custom electrochemical cell for use on SAXS beamlines. These studies revealed some surprising conclusions regarding the templated electrodeposition process: firstly, that the aligned platinum films are templated from polydomain lipid templates, which suggest that polydomain Q_{II} samples display a region of uniaxial orientation at the lipid/substrate interface. Secondly, the platinum films are found to be cubic in the presence of the lipid template but undergo a slight distortion of the lattice along the 111 direction once the template is removed, resulting in a rhombohedral structure where $\alpha = 87$ ˚ ($\alpha = 90$˚ for cubic structures).

4.1 INTRODUCTION

Mesoporous materials have wide-reaching applications in the field of nanotechnology; the ordered nature of these structures has led to uses within lithography[98], catalysis[54,55,99], drug delivery[100–102], molecular sieves[103], batteries[104–106], sensors[107–110] and solar cells[38,39,111]. Bicontinuous cubic structures such as the gyroid are particularly advantageous due to their 3D morphology, which allows for enhanced diffusion[112] and electron transport[113] in addition to high mechanical stability[113,114] and catalytic durability[54,55,115].

Attard et al. were the first to demonstrate that metals can be templated directly from lyotropic liquid crystal structures[41]. Direct liquid crystal templating from type I and II systems has been shown to be a facile, chemically green and cheap method to produce well-ordered nanostructures with a variety of morphologies[41]. Work by Akbar et al. proved that this can be extended to inverse bicontinuous cubic lipid systems[35]. In this work platinum was deposited through a thin film of Q_{II}^{D} phase of the lipid phytantriol[35], exploiting the fact that type II lipids can form the Q_{II}^{D} phase in excess water conditions[12]. Interestingly, deposition was found to occur in a single water network, which was considered to arise from capping of one of the channels at the cubic phase surface; the resulting structure featured a 'single diamond' morphology with Fd3m symmetry, in contrast to the Pn3m symmetry of the 'double diamond' lipid template. Models of both these structures are shown in Figure 4.1.

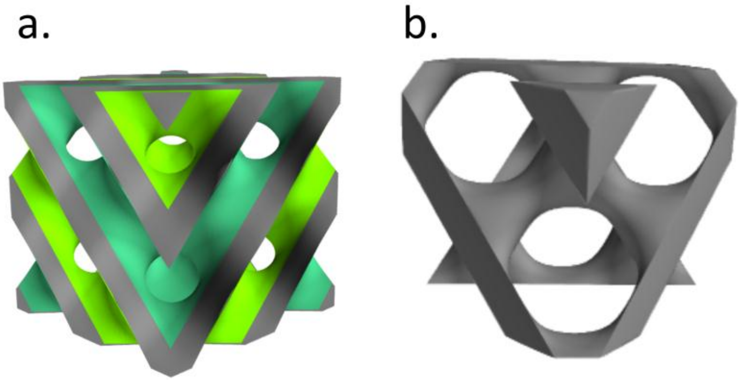

Figure 4.1. The Q_{II}^{D} 'double diamond' phase, where the grey region is occupied by the lipid bilayer, (b), corresponding 'single diamond' platinum structure.

These 'single diamond' nanostructured films were well-ordered, as demonstrated by SAXS data, but still polydomain, giving 'powder-like' scattering patterns comprising of Debye-Scherrer rings. Typically, the properties of materials are enhanced by producing ‘single-crystal’-like single domain structures[15], and it has been predicted that this should result in an enhancement in transport, as well as mechanical properties[116]. Orientation is also important for periodic nanostructures used as lithographic masks, whereby the nanoscale pores allow for higher feature density than possible with conventional lithography[98,117]. Additionally, gold structures with a uniaxial aligned gyroid morphology have been demonstrated to function as metamaterials for visible light, featuring exotic optical properties that depend on nanostructure orientation[84,118]. However, no oriented metal nanomaterials with any other bicontinuous cubic morphology have been produced. There have been several reported methods to produce a Q_{II} phase with an overall alignment by constraining sample dimensions[2,76,119], controlled hydration[15] and by shear flow[13,77,120]. While it might be expected that in order to template an orientated metal structure the lipid template must also feature an overall alignment, here it is demonstrated that it is possible to produce an orientated metal nanostructure using a polydomain lipid template with no overall orientation.

In this chapter, the alignment of platinum nanostructures deposited through a phytantriol template is studied in 3D; depositing onto thin gold foil, which can be measured in both perpendicular and parallel configurations to the SAXS beam. This enables the collection both in-plane (defined as plane parallel to the substrate) and out-of-plane (plane perpendicular to the substrate) data, which typically requires both transmission SAXS and GISAXS or reflection SAXS measurements[2,76,121]. Through this technique, the reproducible fabrication of platinum nanostructures with an Fd3m morphology aligned with the (111) plane parallel to the substrate was demonstrated.

In order to further investigate the mechanism for this orientation, as well as the deposition process in general, a study was performed monitoring both the template and deposit during the electrodeposition process, electrochemically and by SAXS. The crystallographic symmetry of the platinum film (Fd3m) is different to that of the lipid templates (Pn3m), which gives rise to additional reflections that are absent in Pn3m. Due to this difference in symmetries, it was possible to obtain distinct scattering signals for the lipid and platinum films. This allowed for the monitoring of the real-time growth of mesoporous platinum during electrodeposition: measuring the appearance of the Bragg reflection from the platinum nanostructure, as a function of deposition current density; as well as the evolution of orientation of the lipid and platinum films over time, through the use of a new custom electrochemical cell. In other periodic metal nanomaterials deposited within any of the normal topology liquid crystal, mesoporous silica or block copolymer templates previously published, the template and emerging metal have the same symmetry, so such a study has not previously been possible.

By this *in situ* method it was possible to monitor evolution of the metal nanostructures' orientation as it grows, prior to template removal, and better understand observed features in the final metal nanostructure, such as lateral disorder, orientational ordering and distortion of the cubic lattice. These measurements demonstrated that the orientated platinum nanostructures were produced from polydomain Q_{II} phase templates that had no overall orientation. This suggests that, while the lipid template is on average polydomain, a region of the lipid close to the electrode remains orientated with the (111) planes aligned parallel to the substrate. This is supported by previous theoretical work based on bilayer curvature, which has shown that the observed orientation is most favourable for a Q_{II} phase at an interface, with a closed bilayer[119]. Previously, measurements of the lipid surface at the lipid/water interface have been made using atomic force microscopy (AFM)[122], but no comparable information on the lipid/substrate interface has been obtained. This has implications for electrodes modified by Q_{II} phases[32] and is important information for others producing templated materials from lipid cubic phases, as it will dictate the structure of the templated material at the substrate. The platinum films are found to be cubic in the presence of the lipid template, but undergo a slight distortion of the lattice along the 111 direction once the template is removed, resulting in a rhombohedral structure where $\alpha = 87\,^{\circ}$ ($\alpha = 90^{\circ}$ for cubic structures).

In addition, it was possible to monitor efficiency of the growth by looking at the intensity of the SAXS signal from the platinum, which is proportional to the amount of material with respect to the charge passed electrochemically. More generally, on extension to other materials, in cases where deposition is unsuccessful and does not ultimately produce a metal with the expected nanostructure, simultaneously monitoring both the template and the deposited metal can distinguish between different potential explanations. Such explanations include a lack of deposition within the template, disruption of the template and collapse of metal nanostructure on removal of the template or on exposure to air.

In the final part of this chapter it is shown that dimensions of the nanostructure can be tuned with the addition of Brij 56 to the phytantriol template. The addition of a Brij 56, a type I surfactant, to phytantriol, a type II lipid, reduces the curvature of the Q_{II} structure formed, resulting in an increased lattice parameter. This had previously been demonstrated by Akbar[9] however the SAXS data was inconclusive, as the addition of Brij 56 produced additional disorder to the nanostructures resulting in only one scattering ring to be observed. Using both in-plane and out-of-plane measurements it was possible to clearly prove the tuning effect on the 'single diamond' platinum structures.

4.2 EXPERIMENTAL

All chemicals were used as received. Phytantriol (3,7,11,15-tetramethyl-1,2,3-hexadecanetriol) was purchased from Adina Cosmetics; chloroplatinic acid (dihydrogen hexachloroplatinate(2–)) solution (8% w/w in water)) and Brij-56 (polyethylene glycol hexadecyl ether) were purchased from Aldrich.

Thin gold foil and custom gold disc electrodes were used as substrates. Gold foil was purchased from Goodfellow and had dimensions 5 mm × 12.5 µm × 0.5 mm. A custom sample holder was produced for use in the deposition process as shown in Figure 4.2a. The custom mount holds the sample in place between the two pipette tips. A crocodile clip was used to connect the copper tape to the potentiostat.

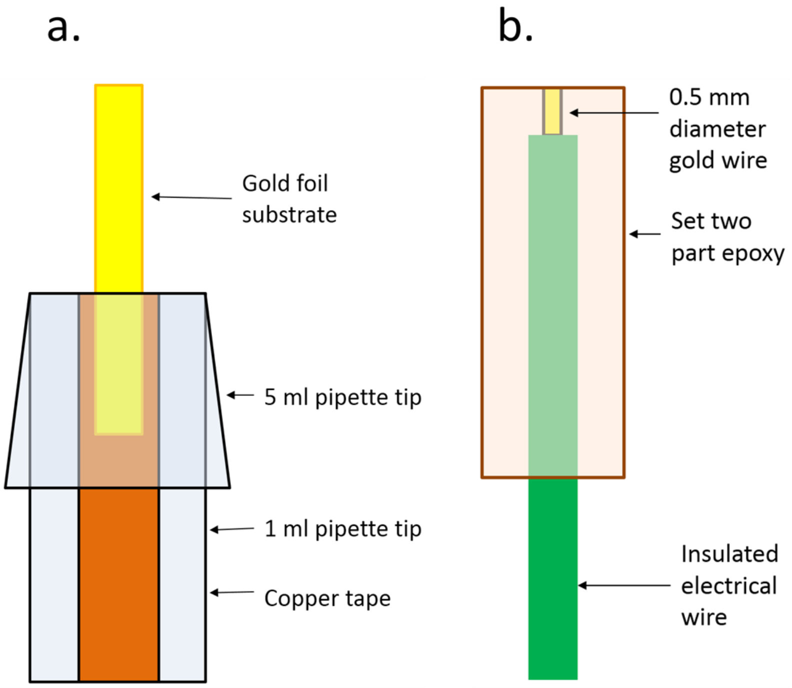

Figure 4.2. Schematic of a sample holder for electrodepositing onto gold foil (a) and a custom gold disc electrode (b).

Custom gold disc electrodes were produced as shown in Figure 4.2b using 0.5 mm diameter gold wire purchased from Goodfellow. Gold wire was cut to 10 mm pieces and attached to electrical wire using conducting silver paint. This wire was put into a 5 ml pipette tip with the end cut off and sealed with Parafilm. The pipette tip was filled with Loctite slow setting two-part epoxy using a mixing nozzle and dispensing gun and left to set for 2 days. Once the glue was dried, the pipette tip was removed leaving behind a custom electrode as shown in Figure 4.2b. The surface of the electrode was polished, initially with sand paper and then using a solution of 25 µm followed by 1 µm alumina powder on a polishing pad.

Nanostructured platinum films were deposited through thin films of dip-coated phytantriol in a fashion similar to that previously reported by Akbar et al.[35]. Substrates were initially cleaned through cycling in 0.5 M H_2SO_4 at 0.2 V/s between -0.2 and 1.8 V vs. Ag/AgCl until the cyclic voltammogram remained steady. The lipid template was applied by dip-coating in a solution of ethanol and 30% or 60% (w/w) phytantriol. Once the template was applied, the substrates were left for 30 minutes in air in order for the ethanol to evaporate, leaving a thin film of phytantriol on the substrate surface, estimated by weight to be 16 ± 0.3 µm in thickness for solutions of 30% phytantriol[9] and 22 ± 1 µm for solutions of 60% phytantriol. Platinum was deposited in a conventional three electrode electrochemical cell using the lipid coated substrate as the working electrode, a 1 cm^2 platinum mesh as a counter and a Ag/AgCl reference electrode. All three electrodes were held vertically, with the foil substrate edge on to the counter electrode in order to minimise differences in conditions on either side of the foil when in use. Before deposition, the lipid coated substrate was soaked for 10 minutes in the deposition solution of 8% (w/w) chloroplatinic acid (HCPA) in water to allow the lipid to hydrate, forming a Q_{II}^D phase on the surface. Platinum was deposited at a potential of -0.25 V vs. Ag/AgCl for 300 s, 600 s or 900 s. After deposition, platinum and lipid coated substrates were washed in Milli-Q water before being submerged in ethanol for 30 minutes in order to remove the lipid template. After soaking, the electrodes were washed again in ultra-pure water leaving a nanostructured platinum film on the gold substrate. The timings for the various steps in Q_{II} template formation and removal were chosen following protocols reported by Akbar et al.[35] and the procedure has been thoroughly characterised[9]. After deposition and template removal, samples were cycled in 0.5 M H_2SO_4 at 200 mV/s in order to confirm platinum deposition and characterise surface area, determined through the total charge measured in the hydride region[9]. All electrochemical experiments were performed with a Metrohm Autolab PGSTAT101 potentiostat controlled by Nova software.

SAXS measurements were performed at beamline I07 at Diamond Light Source, I911-SAXS at Maxlab and BM28 - XMaS at ESRF, respectively using beam energies of 13 keV, 13.6 keV and 15 keV and beam dimensions 200 µm x 200 µm, 300 µm x 300 µm and 250 µm x 250 µm. Pilatus 2M, Pilatus 1M and MAR165 detectors were used to collect data over a range of 0.01 – 0.3 Å at Diamond, Maxlab and ESRF respectively. A sample of silver behenate was used as a calibrant in order to measure the sample to detector distance and determine the beam centre in each case. Deposited platinum films were measured with the beam passing perpendicular and parallel to the plane of the foil on which platinum was deposited, in order to measure the in-plane and out-of-plane orientation respectively. Measurements of lipid coated gold films were taken before any platinum deposition as well as platinum/lipid films, which were quickly submerged in water after deposition. Lipid coated gold foil and platinum/lipid films were held in a custom 3D-printed water cell with Kapton windows to allow X-ray transmission. The cell was made with a path length of 7 mm, which was short enough to allow for SAXS data to be obtained. A schematic of the experimental setup with this custom cell is shown in Figure 4.3. The gold foil used as a substrate was held in place along the long end of the sample holder by conductive copper tape and threaded through a hole in the sample holder to be placed into the cell. A platinum mesh counter electrode was placed in the bottom of the cell and, after filling the cell with 1ml of HCPA, a Ag/AgCl reference electrode was placed in the centre. The cell and sample holder were both designed using Sketchup and produced by 3D printing at Salt 3D services using acrylonitrile butadiene styrene. Models of the printed designs are shown in Figure 4.4. To allow for beam transmission, Kapton windows were adhered onto the cell using a two-part epoxy.

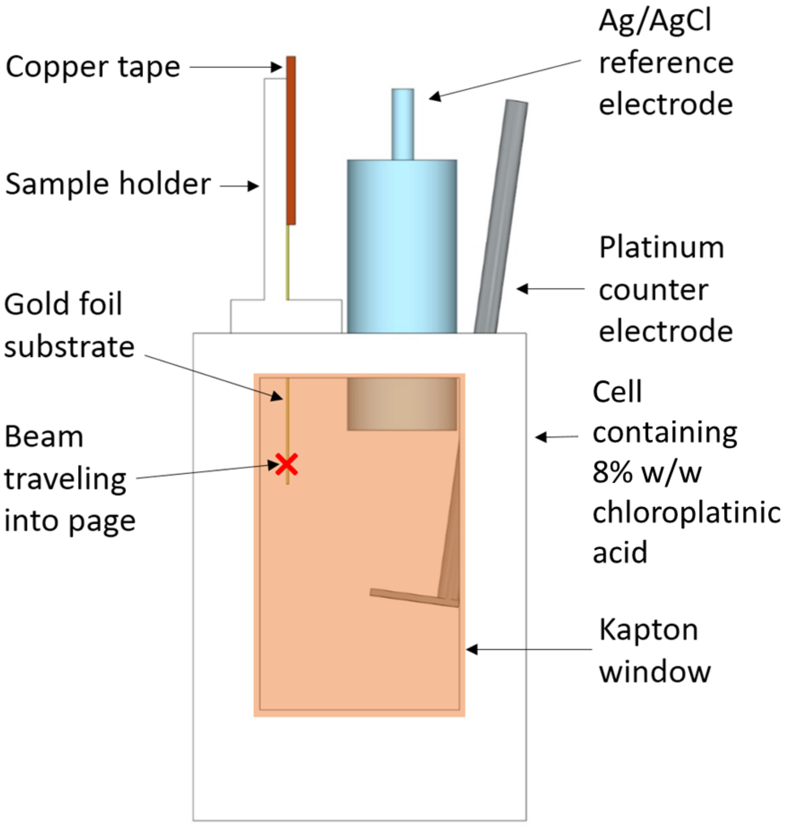

Figure 4.3. Schematic of the experimental set up for simultaneous electrochemical and X-ray scattering experiments.

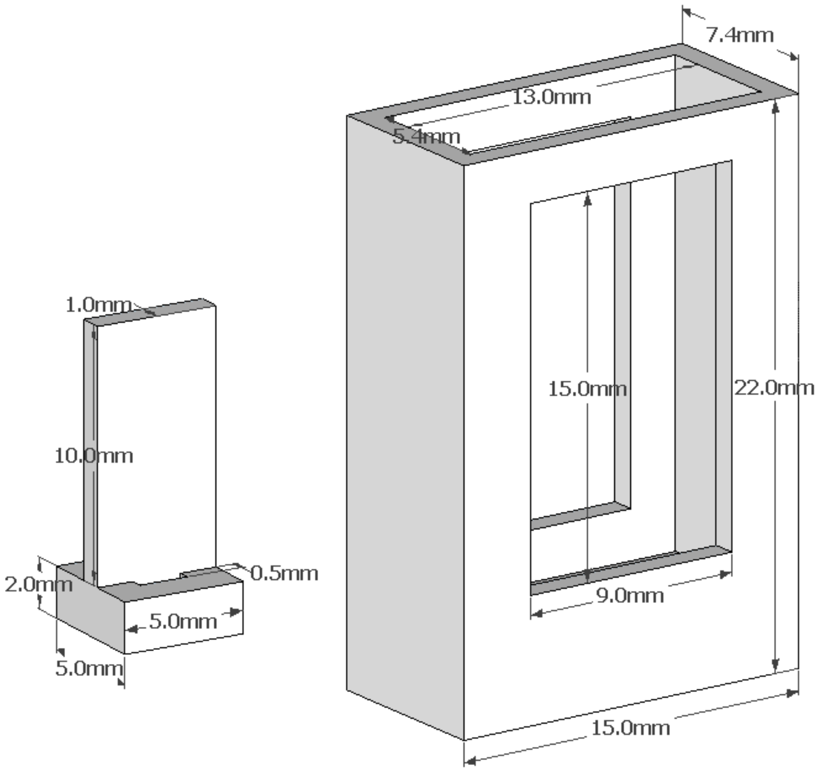

Figure 4.4. 3D models of a printed sample holder (left) and cell (right)

Two-dimensional SAXS images were radially and azimuthally integrated using YAX[88,89]. Phases were identified by assigning peaks measured to Bragg reflections for a given phase. Simulated spot patterns were produced using previously published calculations[2,76], as detailed in the previous chapter.

SEM images were taken using an FEI Quanta FEG 600 environmental scanning electron microscope. Platinum coated foil samples were mounted onto adhesive carbon discs in order to measure the film thickness.

TEM images were taken using a Philips CM20 Analytical TEM. Samples were prepared for measurements by scraping platinum deposit from the substrate using a scalpel and pressing into a lacey carbon film on a copper 300 mesh.

4.3 RESULTS

4.3.1 Electrochemical deposition and characterisation of nanostructured platinum films

Platinum films were electrodeposited onto gold substrates from a solution of HCPA (8% w/w) and water at -0.25 vs. Ag/AgCl. A representitive transient for the elctrodepostion is shown in Figure 4.5; after an initial nucleation period a steady flow of current was recorded as platinum was deposited onto the surface.

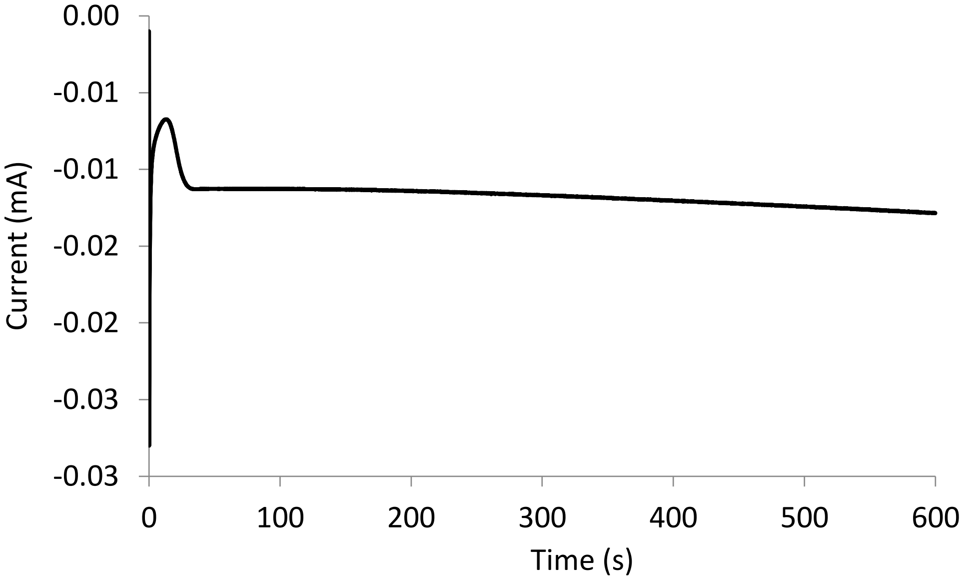

Figure 4.5. Representative transient for electrodeposition of phytantriol-directed nanostructured platinum onto 0.5 mm diameter gold electrode from 8% w/w hexachloroplatinic acid solution at -0.25 V vs. Ag/AgCl.

Once the platinum films were deposited, the surface was charecterised electrochemically with a cyclic voltammetry measurement in acid (0.5 M sulfuric acid in water). A representitive voltammogram is shown in Figure 4.6. Samples were cycled between -0.3 V and 1.2 V starting at 0.2 V in the positive direction. An oxidation and reduction peak can be observed, as the potential is initially increased then decreased respectively. After the reduction peak is observed, at around 0.5V, the current plateaus whilst a double layer of charge builds up on the electrodes surface. As the voltage drops below 0 V, two peaks are observed due to the deposition of a monolayer of hydrogen; corresponding peaks are seen when the potential becomes more positive, as this layer is stripped off. The multiple peaks observed in this region are due to the different surface properties found in the different facets of polydomain platinum, 100, 110 and 111.

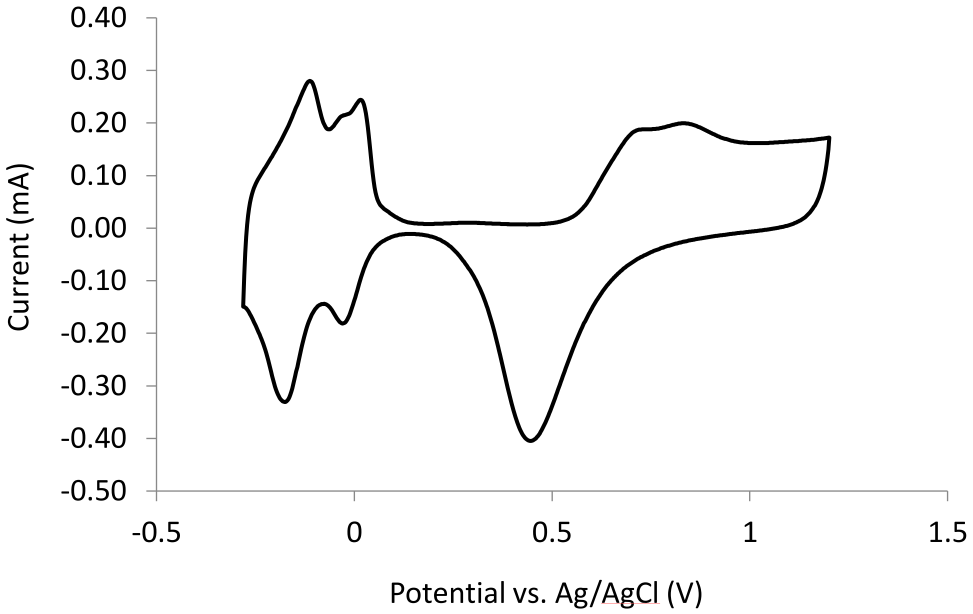

Figure 4.6. A representative cyclic voltammetry measurement for templated platinum film deposited for 600s. CV scan carried out in 0.5M H_2SO_4 at 200 mV/s.

Sample surface area was estimated from the charge passed in the hydride region (0.1 to -0.3 V) in Figure 4.6, as electrons are donated from the surface to hydrogen ions from the acid, allowing the adsorption to occur. The real surface area of the sample can be estimated to be,

$$S = \frac{Q_H}{210}$$

Where S is surface area (cm^2) and Q_H is the average charge passed in the hydride region (µC). An experimentally obtained conversion factor of 210 µC/cm^2 is used to estimate surface area[123]. These values of mass and surface area of platinum can be combined to determine a specific surface area, which was determined to be 42 ± 1 m^2/g across five electrodepositions onto gold disc electrodes, agreeing with previous literature[35].

4.3.2 TEM and SEM images of platinum nanostructures

SEM and TEM measurements provided further characterisation of the nanostructured platinum films. SEM images allowed the overall homogeneity of the films to be assessed, as well as providing an estimate for the film thickness. For this estimation, the platinum coated gold foils were mounted on onto adhesive carbon disks, as shown in Figure 4.7.

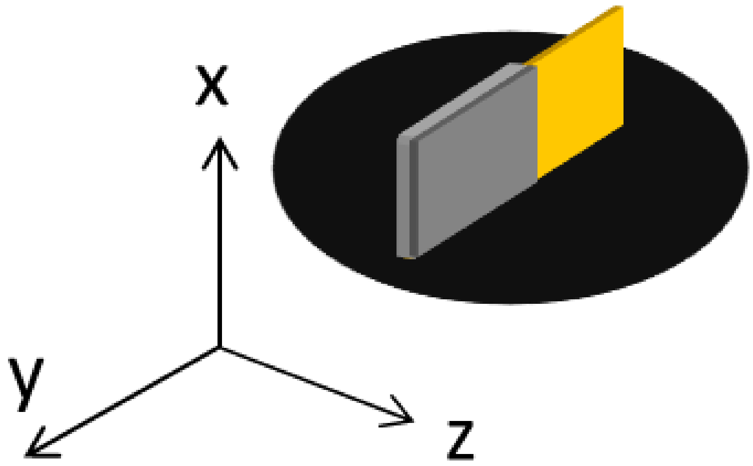

Figure 4.7. Schematic for the SEM measurement set up.

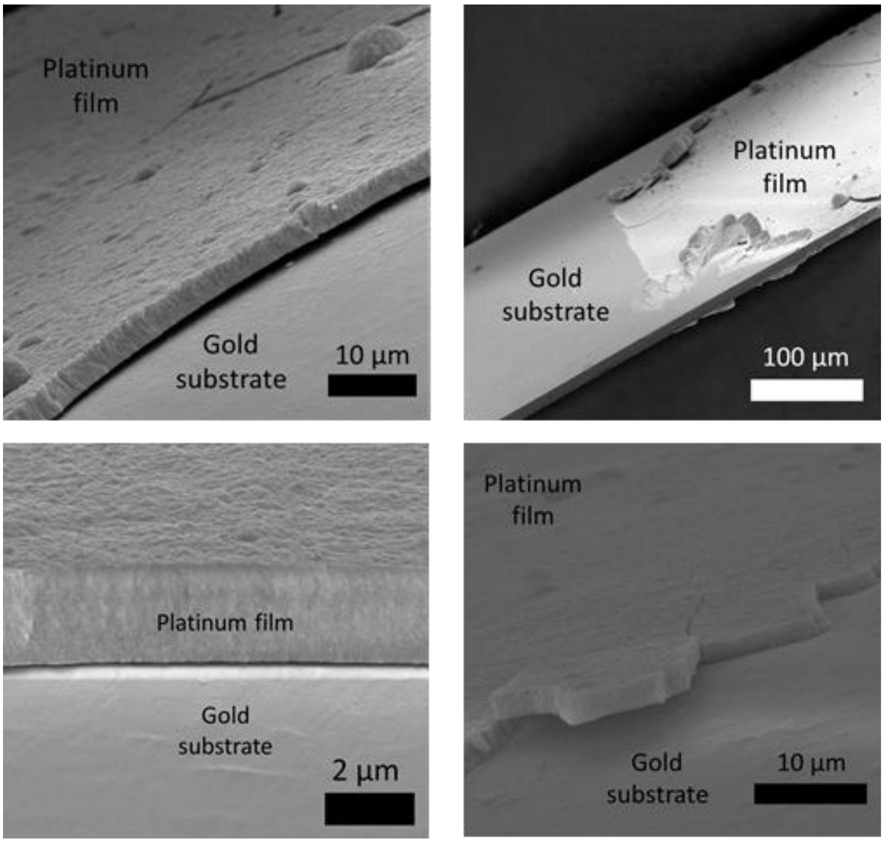

Figure 4.8. SEM images of a platinum nanostructure deposited onto a gold foil substrate. Gold substrate and platinum film are labelled as identified by EDX analysis.

Figure 4.8 shows SEM images of a nanostructured platinum film on a piece of gold foil. Chemical analysis performed by EDX was used to identify the platinum film and gold substrate as labelled. In general, the platinum films show good adherence to the substrates, but the platinum film was seen to flake off in some places. This is not surprising given the flexible nature of the gold foil substrate and the fact that the samples had undergone a lot of bending and flexing during X-ray analysis and transportation to and from synchrotron facilities, before the SEM images were obtained. Flaking of the platinum allowed for SEM images showing film thickness and thickness estimations, detailed in section 4.3.6. TEM images of the deposited platinum nanostructure are shown in Figure 4.9. A porous network of nanowires can be clearly observed. A more detailed characterisation of the un-oriented material is contained in the reference by Akbar et al.[35], where TEM images confirm the 3D network of nanowires 2-3 nm in diameter.

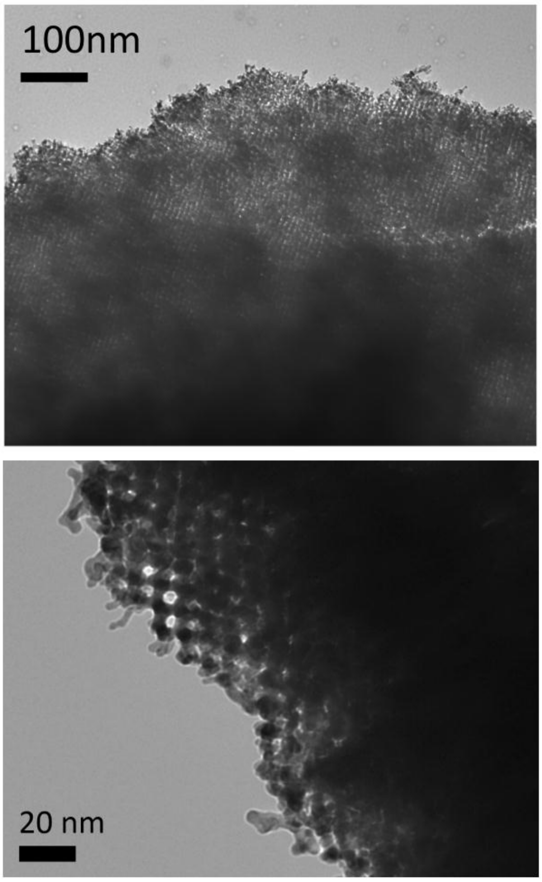

Figure 4.9. TEM images of platinum deposit scraped onto a lacey carbon grid.

4.3.3 In-plane and out-of-plane SAXS measurements of nanostructured platinum

Platinum nanostructures templated using the Q_{II}^{D} phase formed by phytantriol at excess hydration were deposited onto gold foil. In order to describe the position of the sample with respect to the beam, an experimental axis relative to the substrate was defined. Schematics for the two measurement configurations (xy and zy, obtained with beam travelling in the z and x directions respectively) are shown in Figure 4.10, along with corresponding SAXS patterns of a phytantriol-directed platinum nanostructure. Throughout this thesis the xy and zy configurations are also referred to as in-plane and out-of-plane SAXS measurements respectively. In Figure 4.10c, a ring is observed indicating no overall orientation in the xy plane. In contrast, Figure 4.10d shows spots, which indicates a high degree of orientation of the platinum structure in the zy plane. These images clearly demonstrate that the platinum structure displays uniaxial orientation, i.e. fibre averaged about an axis perpendicular to the electrode surface. The scattering pattern produced by the orientated structure closely matches the predicted scattering pattern for Fd3m symmetry orientated with the (111) plane (a/d = √3) parallel to the substrate, which has been superimposed onto Figure 4.10d. An offset angle has been added to the simulated pattern to account for offset of the foil sample, determined from the horizontal scatter from the foil substrate. The on-axis reflections are observed to be more intense, which is predicted by the Lorentz factor for uniaxial orientation.[77,124]. The √8 and √12 reflections are difficult to see on the same image as the √3 reflections due to contrast difference; an adjusted image showing the outer reflections is shown in Figure 4.11, where again the positions match predictions.

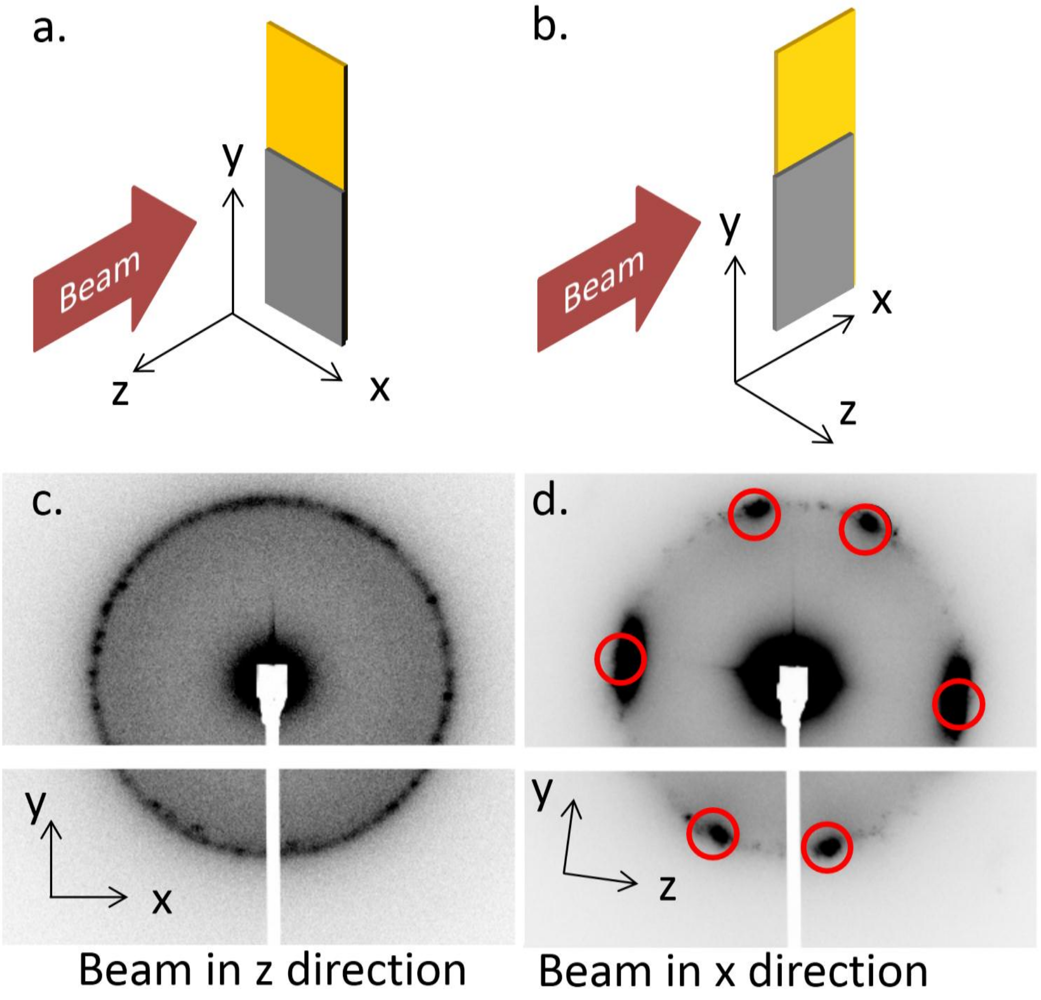

Figure 4.10. Schematic of in-plane and out-of-plane SAXS measurements (a – b), with representative images of nanostructured platinum film measured in each configuration (c-d). The predicted scattering pattern for a structure with a Fd3m morphology with the (111) plane orientated parallel to the substrate has been superimposed as circles on image (d).

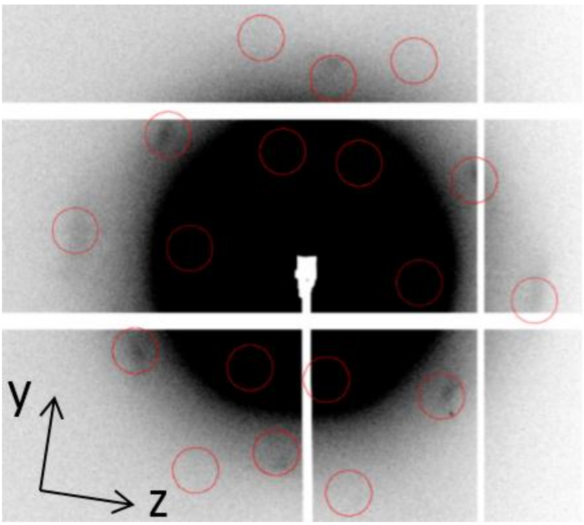

Figure 4.11. SAXS image of the nanostructured platinum film shown in figure 4.11 taken in the zy plane. Contrast has been adjusted to allow for reflections from the √8 and √12 peaks to be observed. Red circles show the predicted spot pattern from the √3, √8 and √12 reflections for a structure with Fd3m morphology and the (111) plane aligned parallel to the y direction.

Radial profiles within 25° wedges, extending in the positive and negative z, x and y directions from the centre of the SAXS images shown in Figure 4.10, were taken in the xy and zy plane. The average signal from the wedges extending in the positive and negative of each direction are shown in Figure 4.12. As the √8 and √12 dots measured in the zy plane are so localised, 25° wedges were chosen in order to see either spots in the radial profiles from the z and y direction wedges, as averaging over the entire ring would hide the signals. No signal is observed for the √11 peak or from the off-axis √12 spots (the full predicted spot pattern for an orientated Fd3m structure is shown in Figure 4.13). For uniaxial scattering patterns the intensity of off-axis reflections is reduced compared to on-axis reflections, which is why only the on-axis √12 spots can be observed out of the √11 and √12 peaks. Under the conditions listed, four samples were fabricated, each producing similar scattering patterns demonstrating the reproducibly of this work.

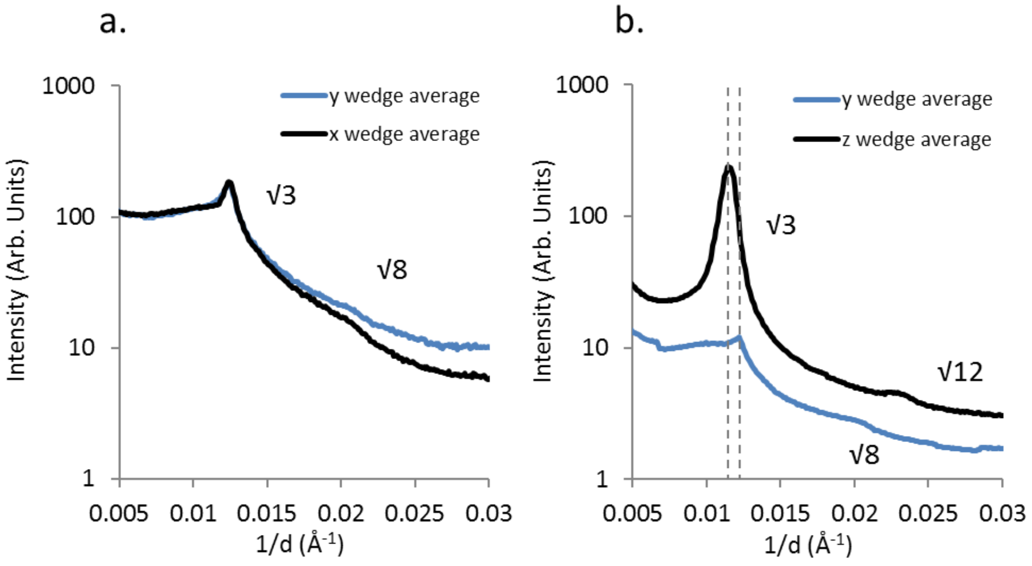

Figure 4.12. 25° wedge radial integrations for a nanostructured platinum foil measured in the xy plane (a) and the zy plane (b). Wedges were taken from the centre of the image in the positive and negative x, y and z directions with the average signal from the positive and negative wedges shown. Characteristic Bragg peaks have been labelled.

Interestingly, it can be observed that the 1/d peak positions do not match, indicating that the platinum adopts a non-cubic structure. Wedge position and size were selected in order for the x and y average to integrate over the on- and off-axis reflections respectively. According to predicted Azimuthal angles for a (111) orientation, on-axis reflections will occur where (hk + kl + hl) = 3; whereas for off-axis reflections (hk + kl + hl) = - 1. The 1/d spacing of the off-axis and on-axis reflections does not agree for the film with the template removed which suggests a rhombohedral distortion of the cubic lattice according to,

$$\frac{1}{d^2} = \frac{(h^2 + k^2 + l^2)sin^2\alpha + 2(hk + kl + hl)(cos^2\alpha - cos\ \alpha)}{a^2(1 - 3cos^2\alpha + 2cos^3\alpha)}$$

where the lattice parameter is found to be, a = 147 Å and the lattice angle, α = 87˚ (α = 90˚ for cubic structures). This result is in contrast to previous observations on double gyroid structures produced using a silica template, where a contraction in the z direction was observed after template removal[54].

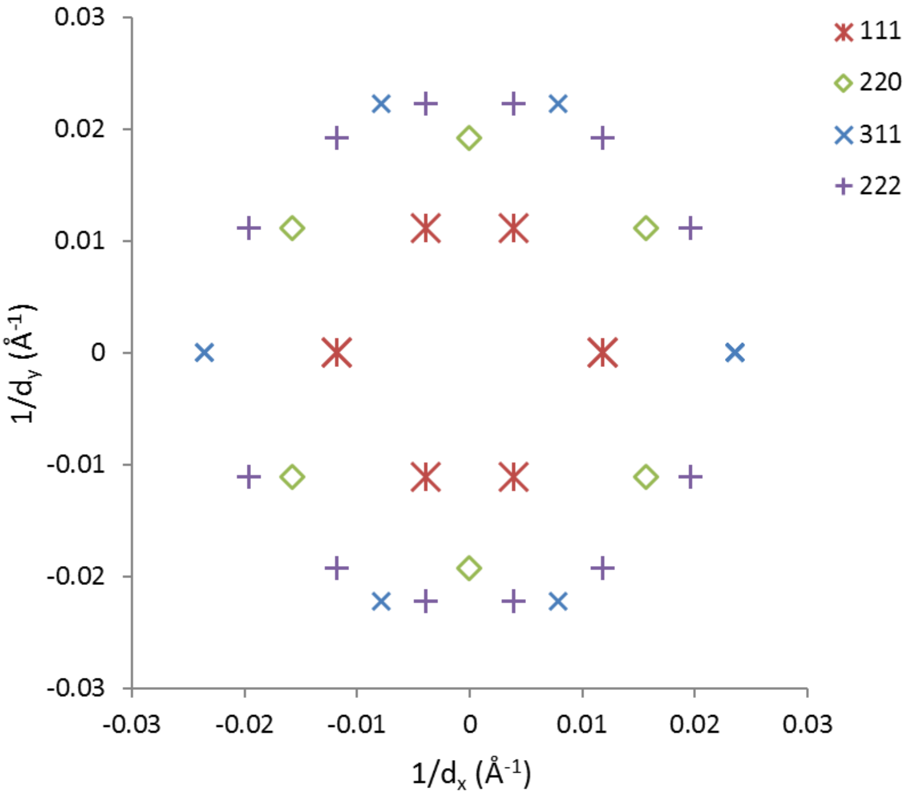

Figure 4.13. Predicted scattering pattern for a structure with Fd3m morphology orientated with the (111) plane parallel to the $1/d_y$ axis.

4.3.4 Out-of-plane SAXS measurements of lipid template

Initially, it was assumed that the dip-coated lipid films would too be orientated, causing orientation of the platinum deposits. In order to investigate the dip-coated films, a SAXS pattern was obtained in the zy plane of a gold substrate, dip-coated in phytantriol and then immersed in water as shown in Figure 4.14. A custom liquid-SAXS cell shown in Figure 4.3 was built in order to facilitate this measurement. No clear orientation of the lipid film can be observed; orientated samples display a regular spot pattern[13,77] which is not observed here. Instead, a randomly orientated polydomain sample is demonstrated by the presence of Debye-Scherrer rings, with uniform intensity (azimuthal profiles of inner reflection shown in Figure 4.15a). The radial profile (Figure 4.15b) shows that the sample has formed a saturated Q_{II}^{D} phase with a lattice parameter of a = 69.2 ± 0.1 Å, in agreement with previous measurements[12] and is approximately half of the 'single diamond' structure due to differences in symmetry[35].

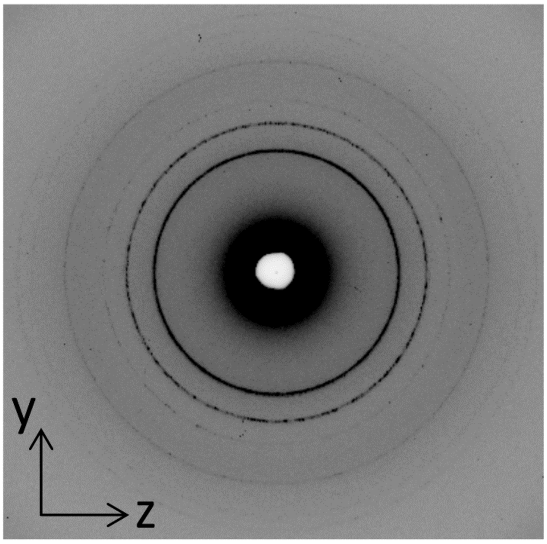

Figure 4.14. SAXS image taken in the zy plane of a thin lipid film on a gold foil substrate dip-coated from ethanol and 30% phytantriol solution displaying Q_{II}^{D} phase.

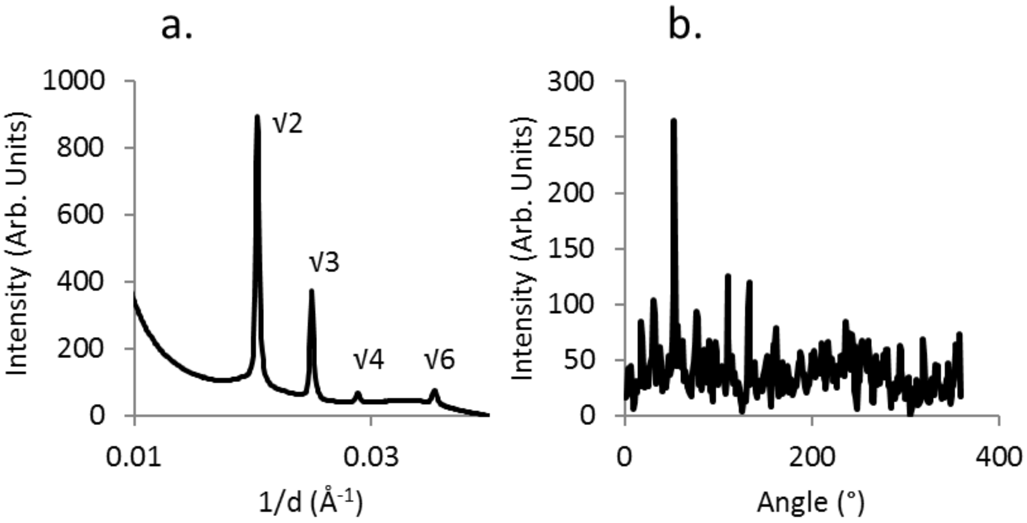

Figure 4.15. Azimuthal (a) and radial (b) profiles of the SAXS pattern shown in Figure 4.14, taken of hydrated phytantriol coated gold foil. Characteristic Bragg peaks for Pn3m space group are labelled on the radial profile.

4.3.5 Imaging the coexistence of the lipid template and a platinum nanostructure

In order to further understand the mechanism for alignment, the coexistence of lipid template and platinum nanostructure after deposition was probed. A SAXS image was taken in the zy plane of the aligned platinum film immediately after deposition, before the lipid template was removed, as shown in Figure 4.16a. In this image both a spot pattern and rings are observed, features previously displayed when separately imaging the platinum structures and the lipid films respectively. The platinum nanostructures are only observed to deposit in a single water channel of the Q_{II} phase[35], leading to differing structural symmetries, observable for the platinum (Fd3m) and lipid structures (Pn3m), giving unique reflections for Fd3m that are systematic absences for Pn3m.

The peak positions for the spot pattern and those from the rings shown in the radial profile (Figure 4.16b) agree with previous measurements for the platinum nanostructures and phytantriol in excess water: the lattice parameters are found to be a = 67.6 ± 0.5 Å for the lipid and a = 146.4 ± 0.6 Å for the platinum film. The predicted spot patterns for an Fd3m structure aligned with the (111) plane parallel to the substrate have been superimposed onto the image and show good agreement with the measured data. The two rings measured from the lipid again do not show any overall orientation, demonstrating that the aligned platinum structures are being produced from polydomain lipid template.

In order to explain this surprising result, it is hypothesised that while overall the lipid is polydomain, the lipid close to the substrate/lipid interface exhibits an overall orientation. Theoretical calculations have shown that for an interface where the Q_{II} lipid bilayer remains continuous and closed, the energy is minimised when parallel to the (111) planes[2,76]. Grazing-incidence SAXS studies, shown in the previous chapter, of different spin-coated Q_{II} films between 0.2 and 1 µm thick all confirmed this orientation[2]. Such films have interfaces with a hydrophobic substrate on one side and a vapour phase on the other, either or both of which could induce the observed orientation. In the current work, our results can be explained by the same phenomenon occurring at the lipid/electrode interface.

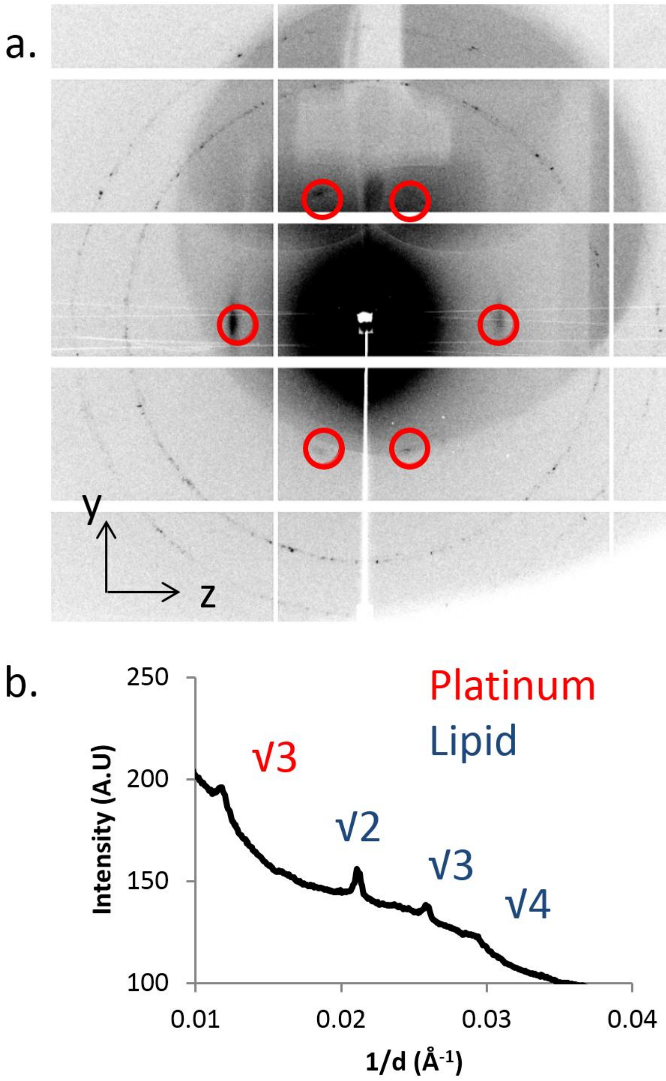

Figure 4.16. (a) SAXS image taken in the zy plane of the platinum nanostructure after deposition and submerged in water before lipid template is removed. (b) Radial profile of the total image with the platinum and lipid Bragg peaks labelled. Limitations in setup resulted in large amount of air scatter, which produced a shadow on the top right.

4.3.6 Determining the dependence of film alignment on thickness

To test the hypothesis that an orientated region of cubic phase was located close to the lipid/substrate interface, platinum films were fabricated with varying amounts of charge. Longer deposition times result in thicker mesoporous platinum films, as they grow deeper into the Q_{II} template coating[35], away from the electrode. Film thicknesses were estimated to be 1.9 ± 0.2 µm (from 5 minutes of deposition), 2.5 ± 0.2 µm, 2.8 ± 0.3 µm and 3.3 ± 0.2 µm, as determined by SEM measurements. Representative SEM images are shown in Figure 4.17. Three images were taken of either side of each film, in order to estimate the thickness and confirm even deposition on either side of the substrate.

Figure 4.18 shows 2D images and azimuthal integrations of the √3 reflection for films of varying thickness. Predicated azimuthal angles are marked by vertical lines; an offset angle was again added to compensate for the angle between the y axis of the foil samples and the detectors vertical axis. Films of thickness up to 2.8 ± 0.3 µm were observed to display orientation of the (111) parallel to the substrate. However, the 3.3 µm film was found to be more disordered, with no defined orientation. Interestingly, a film measured to be 2.5 ± 0.2 µm thickness was observed to feature the (110) orientation in addition to the (111) orientation. In earlier GISAXS work, lipid films produced by allowing a drop of lipid solution in chloroform to run down an angled substrate displayed both the (111) and (110) orientations; such films were less uniform, and likely to have thicker regions[76]. These results are consistent with a Q_{II} lipid template that is overall polydomain and unoriented, but with a region a few microns thick close to the lipid/substrate interface oriented with (111) parallel to the substrate.

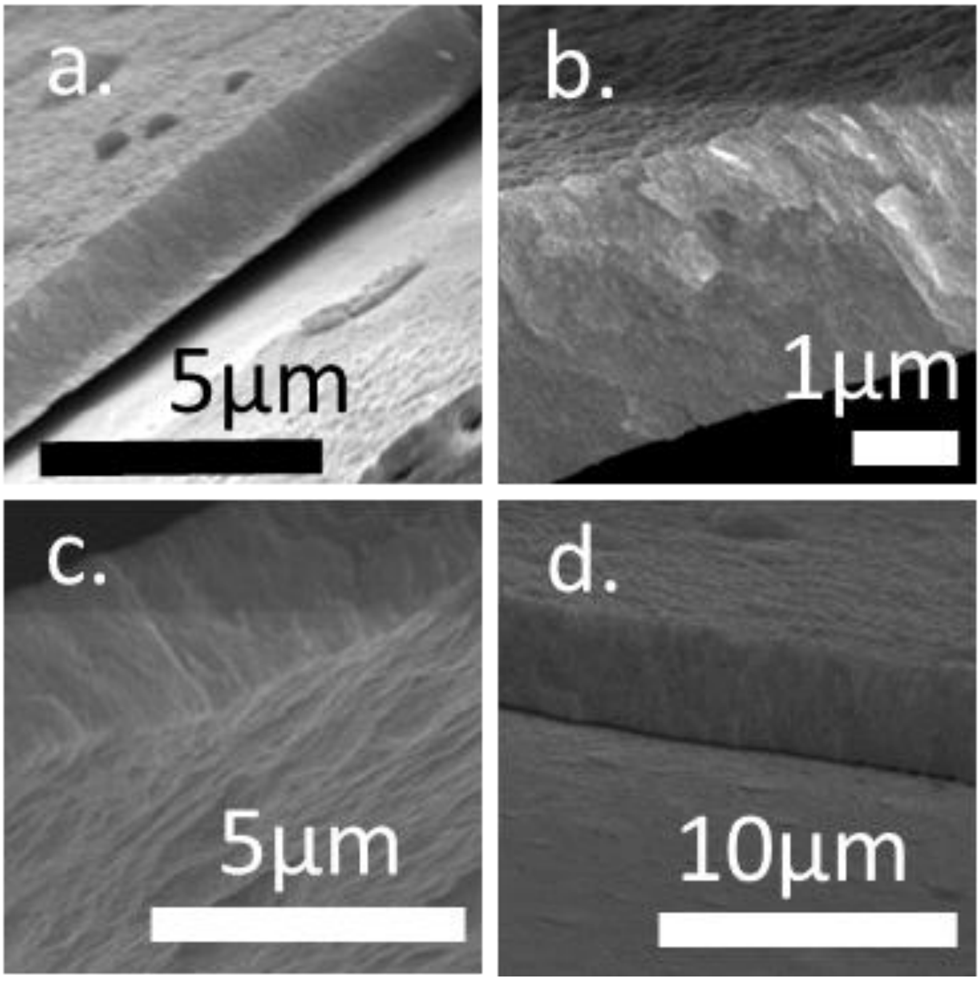

Figure 4.17. Representative SEM images taken in the zy plane for platinum film estimated to be (a) 1.9 ± 0.2 µm, (b) 2.5 ± 0.2 µm, (c) 2.8 ± 0.3 µm and (d) 3.3 ± 0.2 µm.

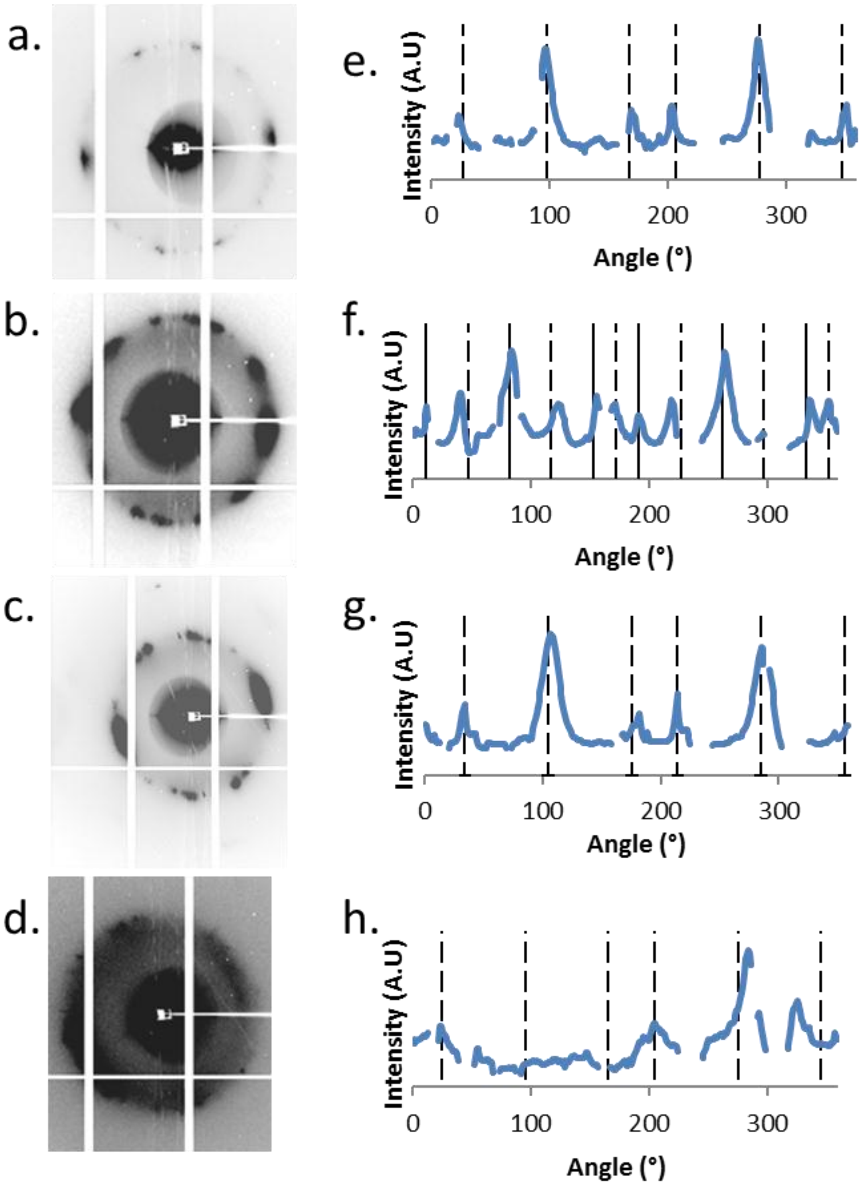

Figure 4.18. (a) 2D SAXS images of nanostructured platinum films taken in the zy plane with varying thickness (a-d) and with azimuthal integrations of each image (e-h). (a, e) thickness = 1.9 ± 0.2 µm, (b, f) thickness 2.5 ± 0.2 µm, (c, g) thickness 2.8 ± 0.3 µm, (d, h) thickness = 3.3 ± 0.2 µm. Predicted azimuthal angles for (111) plane orientated parallel to the substrate are shown by dashed lines for e, g and h, predicted angles for (111) and (110) are shown on f by dashed and solid lines respectively.

4.3.7 Monitoring the growth of lipid templated platinum films by *in situ* SAXS

Building on this work of imaging the coexistence of template and deposit, a further investigation was performed, this time monitoring the platinum electrodeposition as the process evolved. SAXS measurements were taken of a phytantriol coated foil substrate held in a custom electrochemical cell in platinum precursor solution (HCPA). A 1 s image was taken every 120 s during the electrodeposition process. Stacked radial profiles are shown in Figure 4.19; 1D SAXS data is stacked with respect to the deposition time, where 0 s is defined as when the reducing potential of -0.25 V was initially applied. Before this, only the signal from the lipid can be seen, where the √2, √3, √4, √6 Bragg peaks indexed to the Pn3m space group (Q_{II}^{D} phase) are observed. The lattice parameter of the lipid was a = 70.36 ± 0.02 Å. From 0 s a potential of -0.25 V is applied and a new peak was observed to appear at 0.0125 $Å^{-1}$ due to the growing platinum nanostructure. This peak can be identified as the √3 peak of the Fd3m phase from the 2D images, evidence for which will be discussed in section 4.3.8 The lattice parameter of the platinum film was found to be 138.6 Å. This would correspond to asymmetric deposition through a single channel network of a double diamond structure of lattice parameter a = 69.3 Å, which agrees with our observations of the lipid and previous literature[35]. This data demonstrates an *in situ* SAXS measurement of the growth of nanostructured film, whilst simultaneously monitoring the lipid template.

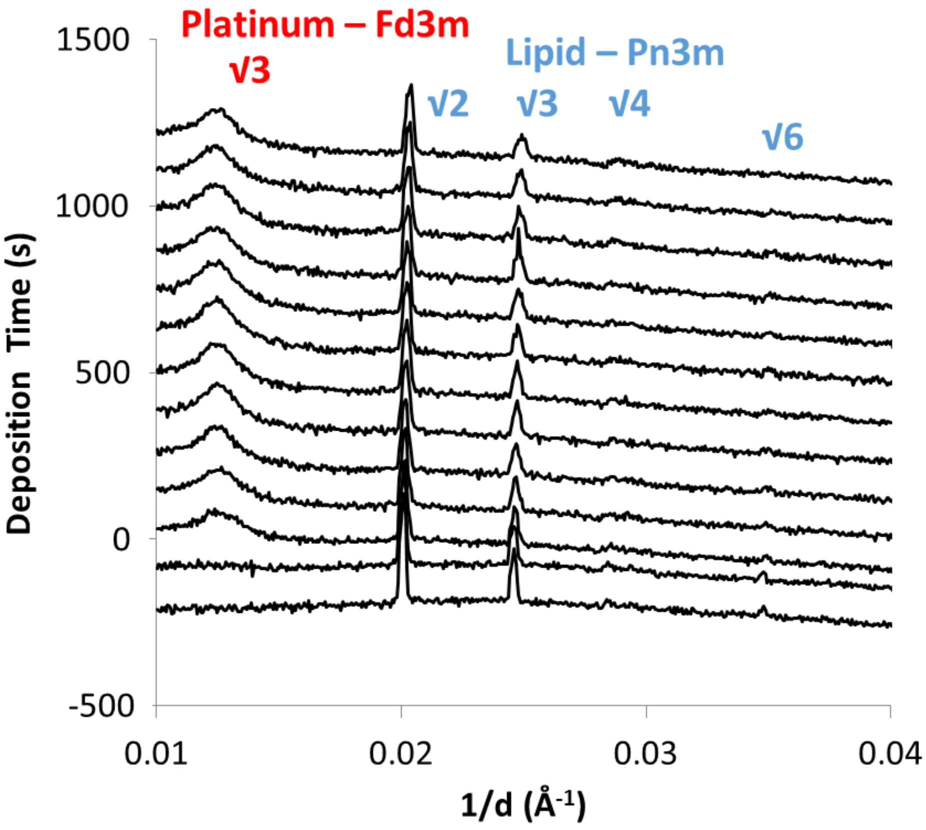

Figure 4.19. Stacked SAXS radial intensity profiles monitoring the deposition process of platinum onto a phytantriol coated substrate. Data are plotted on a log vertical scale and stacked with respect to the depositon time at which the image was taken. The Bragg peaks belonging to the lipid and platinum films are noted.

Figure 4.20a shows how the integrated intensity of the platinum SAXS peak evolves over time, which can be correlated with the charge passed shown in Figure 4.20b. The intensity of a Bragg reflection is usually dependent upon the amount of scattering material so this value would be expected to be proportional to the amount of nanostructured platinum deposited. It can be seen from the plot that the intensity of the platinum peak rapidly increases during the initial deposition. This then slowly increases after 2 C cm^{-2}, before a plateau after 9 C cm-^{2}. After this point, the peak does not increase despite the passage of further current. This may be because the increasing orientational disorder (see section 4.3.8) provides domains that do not satisfy the Bragg condition. However, other potential explanations cannot be ruled out; there is the possibility that no further platinum is being deposited and the current instead is driving other electrochemical processes. Alternatively, platinum could be deposited in a form that is not nanostructured, for example, outside of the lipid template. Contrary to these possibilities, it is noted that in section 4.3.6 the thickness of films of comparable charge density was found to be up to 3.3 ± 0.2 µm[3], as compared with the lipid template thickness[3] of approximately 16 µm[35]. This fact, coupled with the relatively smooth behaviour of deposition charge density, makes these options less likely.

Earlier it was shown that once the lipid is removed the platinum nanostructure features a rhombohedral unit cell with a lattice parameter, a = 147 Å and the lattice angle, $\alpha = 87^\circ$ ($\alpha = 90^\circ$ for cubic structures). Wedged radial profiles for a platinum structure during deposition, coexisting with the lipid template, are shown in Figure 4.21. Images were radially integrated in wedges of 25° extending from the centre along the y and x axes. Wedges taken in x and y directions were found to agree within experimental uncertainty. This indicates that the previously observed elongation occurs after the removal of the template.

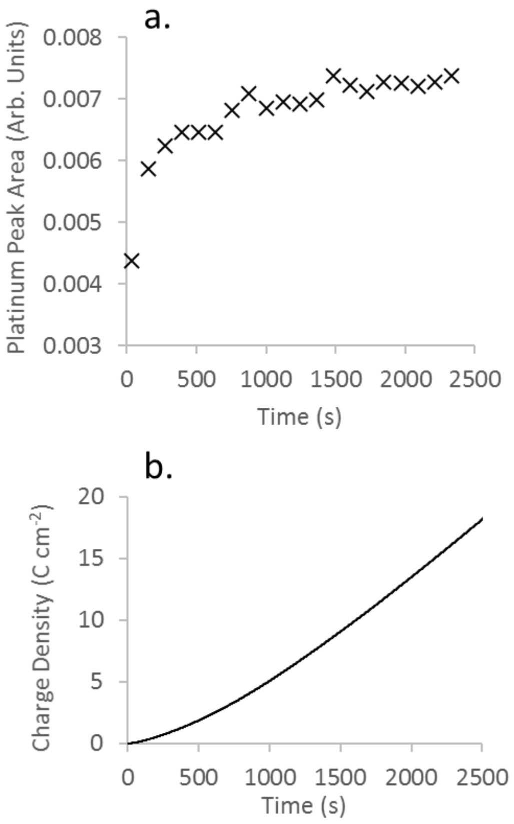

Figure 4.20. Evolution over time of the intensity of platinum SAXS peak at 1/d = 0.0125Å^1 during the electrodeposition of platinum (a), and charge density (b).

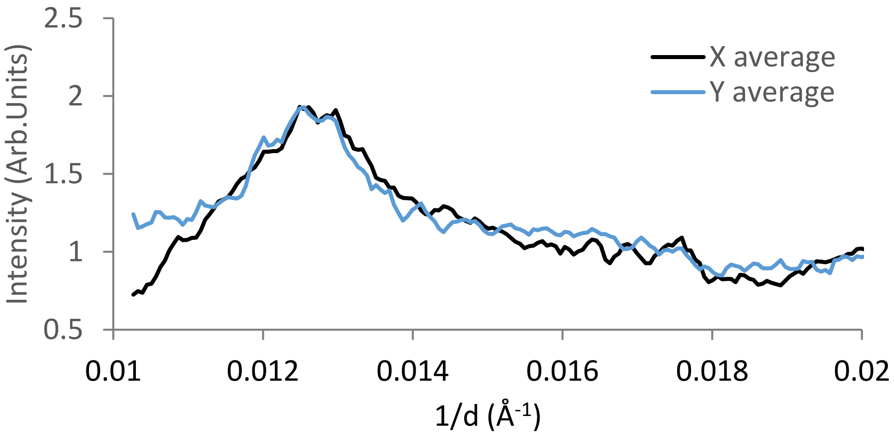

Figure 4.21. Radial profiles taken within 45 degree wedges extending out from the beam centre in the positive x and y directions.

4.3.8 Monitoring the orientation of the deposit and template films during deposition

The 2D SAXS images allow the orientation of the films to be studied in addition to the growth rates and also provide further evidence of the material's morphology. Figure 4.22 shows 2D SAXS images taken during the deposition process, together with 1D Azimuthal profiles of the inner platinum reflection. From the 2D images it can be observed that the innermost reflection, arising from the platinum structure, does not feature uniform intensity indicating that the platinum structure is oriented. The 1D Azimuthal profiles are plotted with dotted lines showing the predicted azimuthal angles for a Fd3m structure with the (111) plane oriented parallel to the substrate. It can be observed that initially the film is highly oriented in this fashion and after continuous deposition the film becomes more disordered. These initial images are able to confirm that this signal is the √3 reflection from an Fd3m structure, as previously assumed. The outer two rings correspond to the lipid template and can be observed to be uniform in intensity, indicating a polydomain structure with no overall alignment. This demonstrates that the aligned platinum films are being produced from overall polydomain lipid templates. This agrees with previous data in this chapter, where it was hypothesised that there was an orientated region of the polydomain lipid close to the substrate interface. Platinum grown in the surface orientated polydomain film will initially be orientated as the lipid film, but as more charge is passed and the film becomes thicker, this order will gradually be lost.

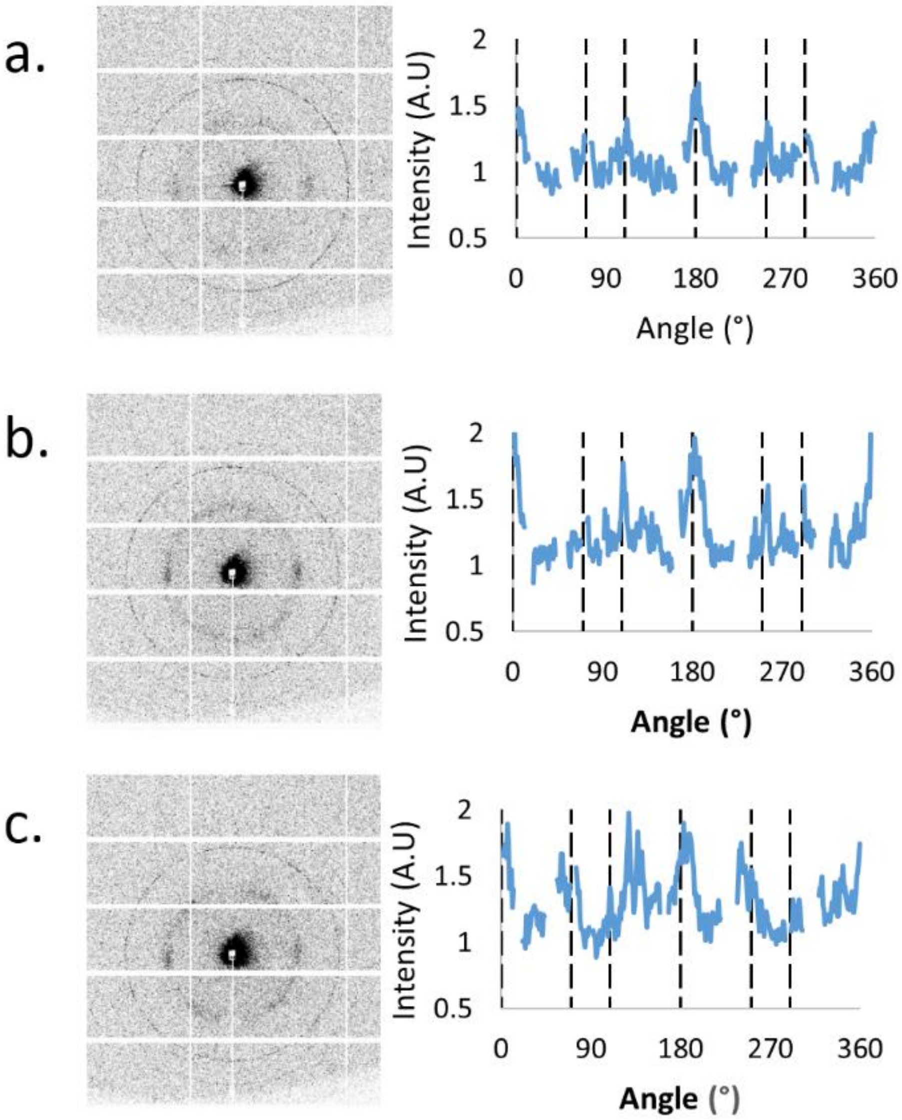

Figure 4.22. 2D SAXS images taken during electrodepositon (left) with 1D azimuthal profile of the inner ring, which arose from the deposition of platinum (right) after 153s (a.), 516s (b.) and 1242s (c.).

In order to quantify the level of alignment in the platinum deposit, the average intensity at each of the predicted azimuthal angles taken from the 1D azimuthal profiles was divided by overall average intensity. This orientation value would be 1 for a completely polydomain sample, and increases as the sample becomes more aligned. Figure 4.23 shows the orientation as defined, plotted over time. This plot demonstrates more clearly that the films are initially oriented, and after 1200 s of charge being passed the structure becomes disordered and polydomain.

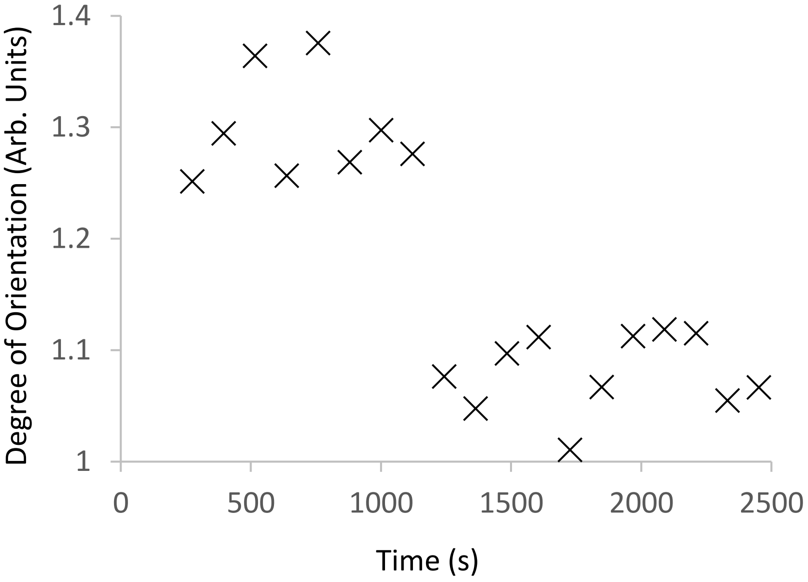

Figure 4.23. Defined orientation value of platinum film with the (111) facet parallel to the substrate plotted against deposition time

4.3.9 Tuning nanoscale morphology with the addition of Brij 56

Platinum films were deposited through a phytantriol/Brij 56 template. As Brij 56 is a type I surfactant, it causes the curvature of phytantriol (a type II lipid) to decrease, and thus the lattice parameter of deposited materials to increase. This system has thoroughly characterised by Akbar, who demonstrated tuneable platinum nanostructures by varying the concentration of Brij 56 in the Brij/phytantriol template[9]. However, the addition of Brij 56 was also observed to increase the disorder, resulting in wider Bragg peaks in the out-of-plane SAXS measurements and, crucially, only a single scattering peak. This is not sufficient evidence to prove the Fd3m structure was produced. Out-of-plane SAXS measurements (in the zy plane) were used in order to prove that platinum with an

Fd3m structure and tuneable dimensions was electrodeposited through a phytantriol/Brij 56 system. Figure 4.24 shows the 1D radial SAXS profiles taken of platinum produced from the phytantriol/Brij 56 system; the Bragg peak is observed to move to lower 1/d values, indicating swelling of the film with increased Brij 56 content. However, these results only show a single peak, which is insufficient proof of a particular nanostructure, despite appearing where the first √3 peak would be expected to arise.

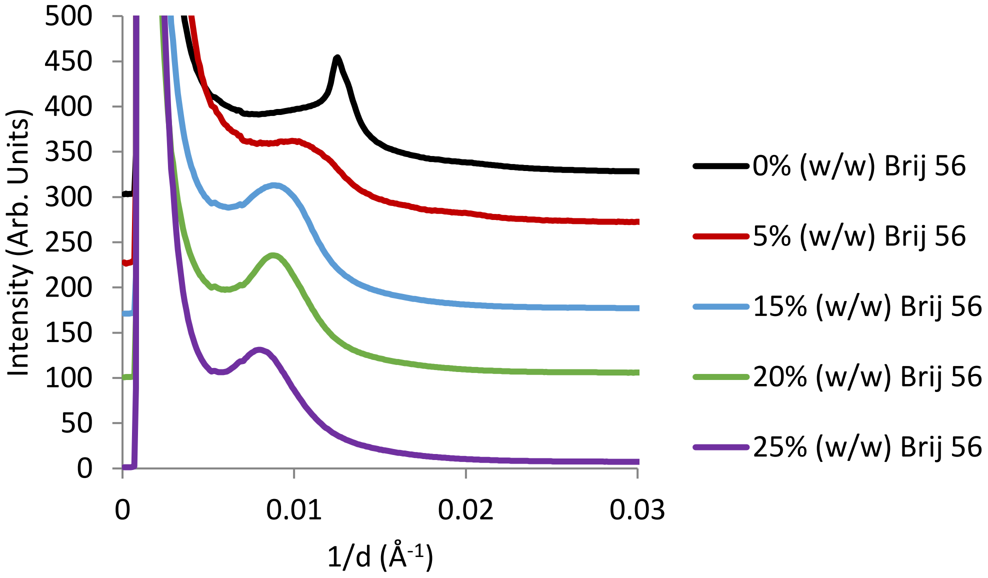

Figure 4.24. 1D SAXS profiles for platinum electrodeposited for 300s from a phytantriol/Brij 56 template.

Figure 4.25 shows 2D SAXS images of platinum nanostructures templated from phytantriol and 0, 5 and 10% (w/w) Brij 56 taken in the xy and zy planes respectively. From these images it can be observed that the films feature uniaxial orientation from the presence of dots in the out-of-plane image.

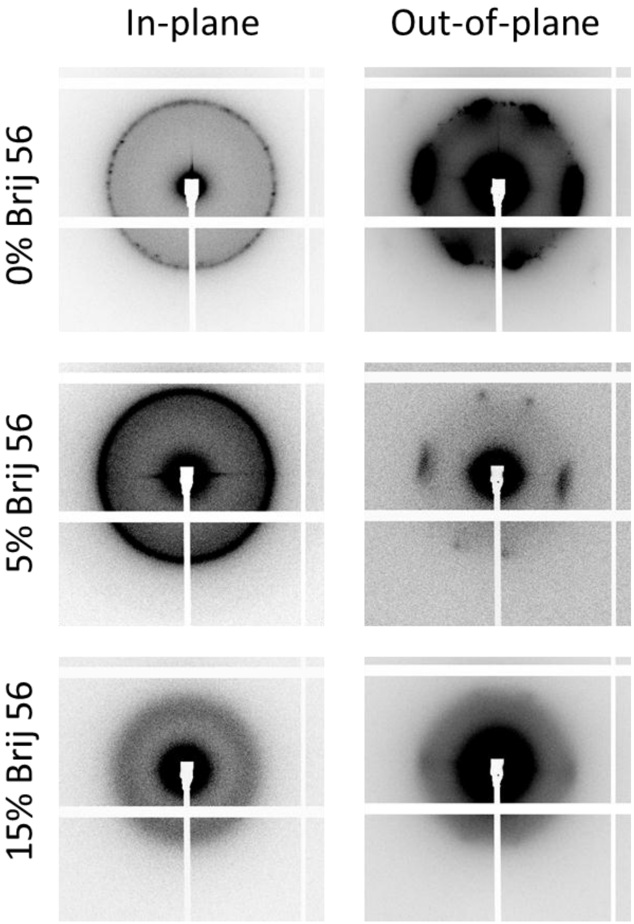

Figure 4.25. In-plane (xy) and out-of-plane (zy) SAXS image of platinum nanostructure deposited from a template of phytantriol and 0, 5 and 15% w/w Brij 56.

Uniaxially aligned structures were observed at concentrations of 0%, 5% and 10% Brij 56, whereas at concentrations of 20% and 25% only polydomain rings were observed. Figure 4.26 shows the lattice parameter with respect to Brij 56 concentration, with aligned structures marked as crosses and polydomain as plusses. This data provides proof of a tuneable platinum nanostructure with a lattice parameter of 140 – 192 Å when electrodepositing through a phytantriol/Brij 56 (0 – 15% w/w) template. The structures deposited through the templates containing 20% and 25% Brij 56 were not found to be orientated, and thus the structure cannot be proven from the single observed peak. However, it is likely that these too feature a 'single diamond' morphology, but that it is polydomain rather than aligned.

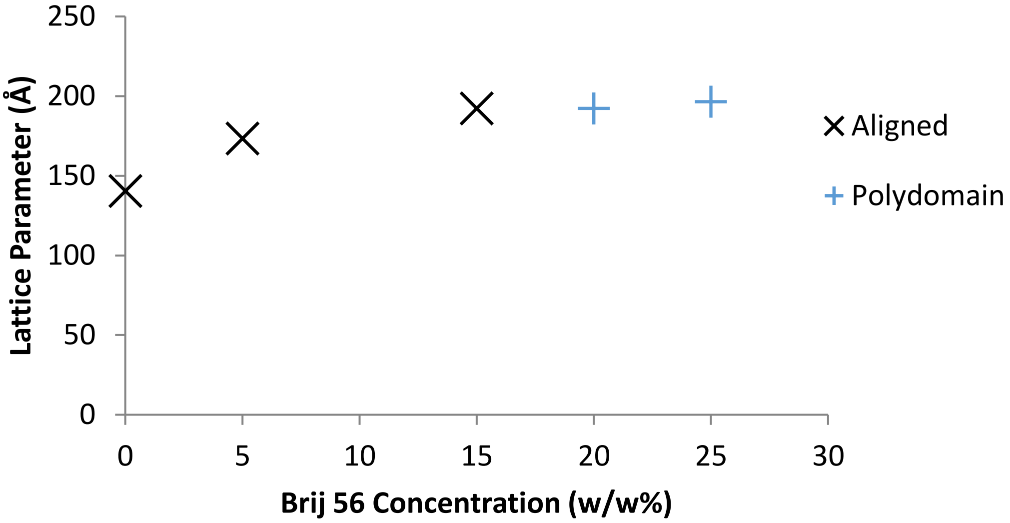

Figure 4.26. Lattice parameter of platinum nanostructures deposited from phytantriol/Brij system with respect to Brij concentration (%w/w). Samples were observed as being either aligned (×) or polydomain (+).

4.4 CONCLUSIONS

In conclusion, nanostructured platinum has been electrodeposited through the Q_{II}^{D} phase of the type II lipid phytantriol from a platinum precursor solution. These structures have been demonstrated electrochemically to feature high surface area, > 40 m^2/g. SAXS measurements provided evidence of an Fd3m structure, which was shown to feature uniaxial alignment in out-of-plane SAXS measurements. Further investigations into the mechanism for alignment were performed by simultaneously monitoring the structure of the lipid template and the nanostructured deposit through SAXS measurements, whilst also measuring the growth of the platinum structure electrochemically through the use of a new custom electrochemical cell. By these measurements, it was shown that these aligned platinum structures were produced from polydomain lipid cubic templates, suggesting that the Q_{II}^D phase features a region of interfacially-driven alignment, rising approximately 3µm from the lipid/substrate interface. These findings give a new insight into the Q_{II}-electrode interface and have implications for the production of functional nanomaterials. This is the first time a study has been able to monitor both the template and deposit during the deposition of a mesoporous film, by taking advantage of the unique asymmetry found in the Q_{II}^D deposition system. It is possible that this technique could be extended to other materials templated from a lipid cubic phase system. In addition, the development of these out-of-plane SAXS images allowed for observations of direct evidence for an Fd3m structure with tuneable dimensions from the phytantriol/Brij 56 system.

5 NANOSTRUCTURED PLATINUM FILMS FOR DIRECT ALCOHOL FUEL CELLS

In this chapter, phytantriol templated platinum nanostructures featuring high surface area (42 ± 1 m^2/g) were assessed for use as anode catalysts in alcohol fuel cells. Platinum nanostructures deposited onto gold disc substrates exhibited enhanced catalytic responses to the oxidation of both ethanol and methanol, when compared to unstructured platinum films. As the soft lipid template was applied to the substrate by dip-coating from a lipid/ethanol solution, lipid cubic phase templating is potentially compatible with any conductive substrate; this was demonstrated by electrodepositing directly on porous carbon paper, as used in conventional fuel cell design. Platinum nanostructures on carbon and gold disc electrodes showed a comparable result towards the oxidation of ethanol. This versatility, and the observed enhanced catalytic properties, mean that this technique presents a practical method for nanostructured films to be incorporated into conventional fuel cell designs.

5.1 INTRODUCTION

The direct alcohol fuel cell, a device which converts chemical potential energy in fuels such as methanol or ethanol into electrical energy, is a promising candidate to one day replace the traditional fossil fuel combustion engine. Oxidation of fuel occurs at the anode and is part of a redox reaction facilitating the flow of current through the cell. In order to achieve a practical current output, a catalyst is required at the anode to increase the rate of fuel oxidation[125,126]. As a catalyst, platinum far outperforms other materials and the current industry standard is in the form of nanoparticles suspended on a porous carbon support (Pt/C)[52,127]. The small particle size allows for high activity per gram, or mass activity, however, the cost of these catalysts still remains too high. For widespread commercial use, the amount of platinum must be reduced either by substitution for another material or by increasing the catalytic response of platinum itself, thus allowing the active material to be reduced. In addition, nanoparticle catalysts are prone to instabilities, whereby active catalytic sites can be reduced through a number of routes, such as detachment, coalescence and poisoning[128].

In order to address these two fundamental issues, much work has gone into researching ways to enhance the catalytic activity and stability of platinum by using platinum alloys[47,129–133], as well as other non-precious materials[134–138]. Another route is through the production of nanostructured platinum, with reports of nanowires[99,139–142], nanosponges[46], nanoflowers[143,144], nanocages[145] and hollow nanospheres[146] all showing enhanced catalytic properties over unstructured platinum. Recently, nanostructured platinum based upon continuous 3D geometries has been demonstrated to achieve far superior stability in addition to enhanced activity. This enhanced stability is postulated to be due to the self-supporting nature of the 3D topology and a higher proportion of the more active (111) and (100) sites at the surface is believed to lead to the observed activity improvements[54]. Whilst these results are very promising, the relatively low specific areas obtained have limited the mass activity and thus the feasibility of these systems in comparison to commercial nanoparticle catalysts[55]. Typically, ordered nanostructured films are fabricated in the gyroid morphology through the use of surfactant ordered silica[54,115,147,148] or an etched block copolymer template[55,149]. However, these methods have long fabrication times (over a week) and require harsh chemical or environmental conditions in order to form and remove the template[54,55].

The lipid cubic templating route to produce ‘single diamond’ platinum structures described in the previous chapter presents itself as a promising alternative to silica and block copolymer routes. This procedure, including the formation and removal of the template, can be undertaken in approximately an hour without the need for any harsh conditions, as the lipid can simply be dissolved in ethanol. In this chapter, the catalytic response of these ‘single diamond’ structures to the methanol and ethanol oxidation reactions is investigated. Greatly enhanced specific and mass activities when compared to non-templated platinum films, as well as commercial catalysts and other ordered nanostructured systems, are demonstrated. In addition to this enhanced activity, a comparable loss of surface area after 3000 cycles was observed compared to commercial nanoparticles, but whilst maintaining a far greater activity per unit area (specific activity) towards the oxidation of methanol, resulting in a maintenance of mass activity comparable to the initial performance of commercial nanoparticles.

One area that has been overlooked by current research into ordered nanostructured catalysts is the feasibility of their incorporation into conventional fuel cell designs. Electrodeposition through a lipid cubic phase potentially allows for the fabrication of nanostructured material onto any conducting substrate, which is demonstrated in this chapter by electrodepositing ‘single diamond’ platinum directly onto porous carbon paper. Phytantriol-directed platinum nanostructures deposited on porous carbon paper are shown to feature comparable catalytic activity to nanostructured platinum deposited onto gold disc substrates. These ordered nanostructures offer a practical method for nanostructured platinum catalysts to be incorporated into conventional fuel cell designs due to the ability to deposit onto gas diffusion layers already in industrial use and enhanced catalytic properties towards alcohol oxidation reactions.

5.2 METHODS

All chemicals and materials were used as received. Phytantriol (3,7,11,15-tetramethyl-1,2,3-hexadecanetriol) was purchased from Adina Cosmetics, chloroplatinic acid (Dihydrogen hexachloroplatinate(2–)) solution (8% w/w in water), methanol and ethanol were purchased from Sigma-Aldrich. Carbon paper AvCarb P50 and Toray T03 carbon paper were purchased from FuelCellsEtc.

Nanostructured platinum films were deposited through thin films of dip-coated phytantriol onto gold disc electrodes, as described in the previous chapter. Carbon paper was cut into pieces 5 mm x 10 mm, with deposition occurring on approximately 5 mm x 3 mm. Electrochemical experiments were performed in a three electrode cell featuring a Ag/AgCl reference electrode (3M KCL) and a platinum mesh counter electrode. Surface area of the nanostructured films was measured by cyclic voltammetry (CV) in 0.5 M H_2SO_4, with the charge passed in the hydride region used to calculate the electroactive surface area[45]. Catalytic characterization was performed by CV in a solution of 0.5 M methanol/ethanol + 0.5 M H_2SO_4 at 50 mV/s. Solutions of alcohol and sulphuric acid were made fresh on the day of measurements and the cell sealed in parafilm during measurements, in order to minimise evaporation of the alcohols.

Structural characterisation of nanostructures was performed by SAXS, as well as scanning and tunnelling electron microscopy. SAXS measurements were performed on beamline I07 at Diamond Light Source and I911-SAXS at Maxlab with a beam size of 200 µm x 200 µm and 300 µm x 300 µm and energies of 13 keV and 13.6 keV respectively. At both I07 and I911-SAXS data was collect over a range of 0.01 – 0.3 Å using Pilatus 2M and 1M detectors respectively. SEM images were taken using an FEI Quanta FEG 600 environmental scanning electron microscope, with samples mounted on aluminium studs by adhesive carbon film. For the TEM images, deposited platinum was scraped off of substrates using a scalpel and pressed into a lacey carbon film on Copper 300 mesh before measurement in a JEOL JEM-2010 High Resolution TEM.

5.3 RESULTS

5.3.1 Morphology characterisation

Phytantriol-directed and non-templated platinum films were electrodeposited onto gold disc electrodes with deposition transients shown in Figure 5.1. The amount of platinum was estimated from the total charge passed, as described in the previous chapter. Representative voltammograms for nanostructured and non-templated platinum electrodes in 0.5 M acid measured at 200 mV/s are shown in Figure 5.2. Surface area was again estimated from charge passed in the hydride region (-0.3 – 0.1 V vs. Ag/AgCl) where cathodic and anodic peaks correspond to the deposition and subsequent removal of a hydrogen monolayer[57]. The nanostructured electrodes were found to feature high specific surface area, 42 ± 1 m^2/g and non-templated platinum films featured a lower specific surface area of 2.0 ± 0.5 m^2/g.

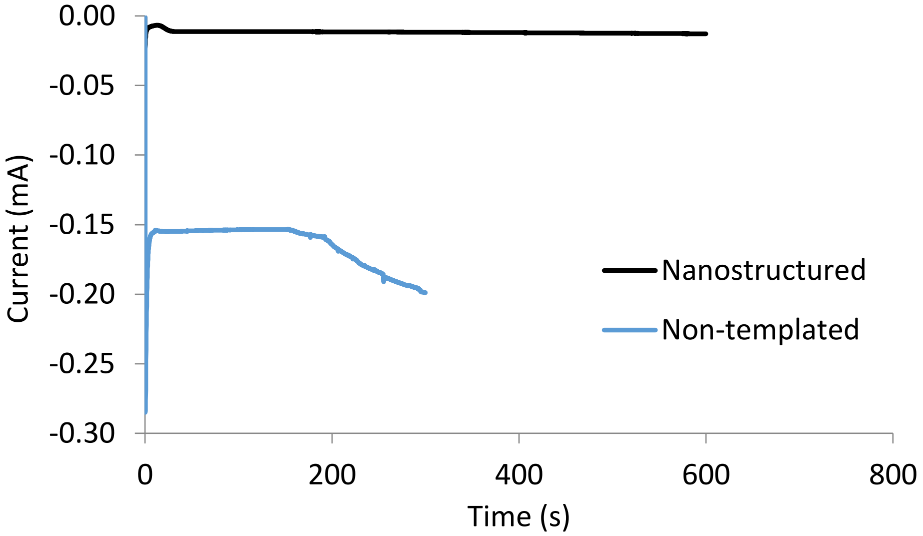

Figure 5.1. Deposition transients for the electrodeposition of phytantriol-directed nanostructured and non-templated platinum from a HCPA solution at -0.25 V vs. Ag/AgCl.

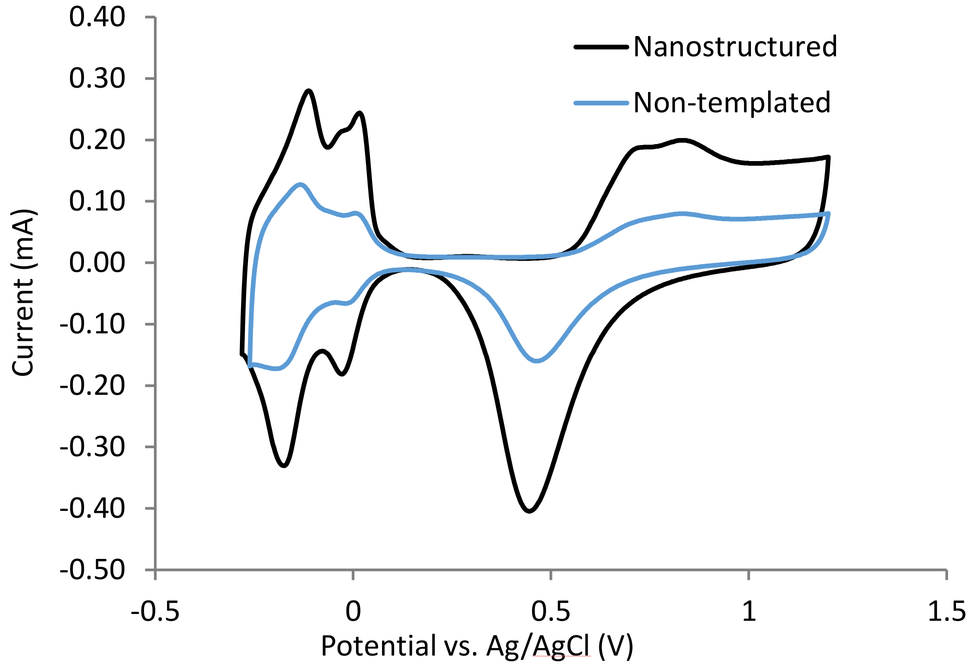

Figure 5.2. Cyclic voltammetry measurements for nanostructured and non-templated platinum films in 0.5M H_2SO_4 at 200 mV/s.

The nanostructured platinum films deposited onto the gold discs featured a 'single diamond' morphology with the Fd3m symmetry, as demonstrated in the previous chapter. Phytantriol has been well characterised to form a 'double diamond' cubic phase under the excess hydration conditions found in the deposition process[1,2]. Figure 5.3 shows a representative TEM image of a platinum nanostructure deposited onto the gold substrate, showing a large porous network.

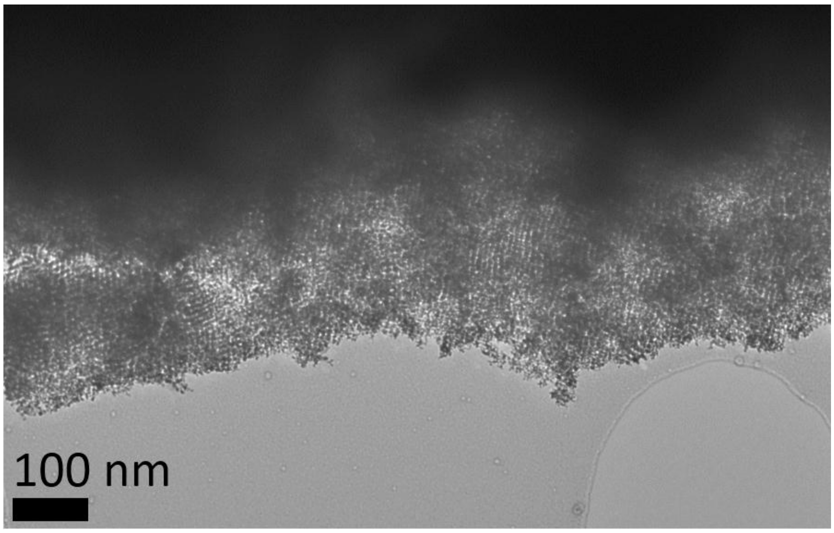

Figure 5.3. TEM images of a phytantriol-directed nanostructure, darker regions show the platinum nanowire network.

5.3.2 Evaluation of catalytic responses to the oxidation of alcohols

The catalytic responses of both electrodes with respect to the oxidation of methanol and ethanol was evaluated through CV measurements in 0.5 M ethanol/methanol + 0.5 M H_2SO_4 between -0.3 V and 1 V vs. Ag/AgCl at 50 mV/s; representative voltammograms are shown in Figure 5.4. Anodic peaks in forward and reverse scans exhibited by both films demonstrates a catalytic response to the oxidation of ethanol and methanol[99,150]. In particular, the peak in the forward scan located around 0.7 V is directly proportional to the oxidation of the respective fuel[99]. The nanostructured 'single diamond' electrode is observed to feature a much greater specific activity than the non-templated electrode for both reactions. It is important to note that the specific activity is normalised with respect to the actual electroactive surface area, as measured from Figure 5.2, not the geometric surface area, indicating that the nanostructured catalyst features a surface more active per unit area than that of the unstructured platinum film.

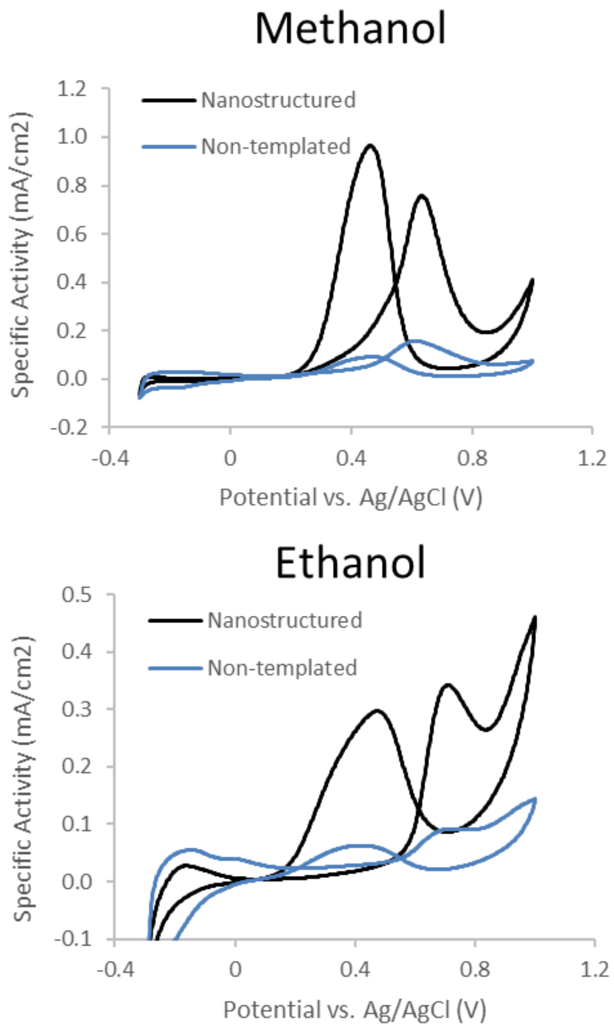

Figure 5.4. Representitive CV measurements for phytantriol-directed and non-templated electrodes in 0.5 M ethanol/methanol + 0.5 M H_2SO_4 cycled between -0.3 V and 1 V vs. Ag/AgCl at 50 mV/s. Current density was normalised according to the measured electroactive surface area.

Table 5.1 lists the specific area, the peak specific activity and mass activity (measured in the positive scan of the CV) for the ‘single diamond’ and non-templated electrodes towards the oxidation of methanol; for comparison values of commercial and another 3D ordered nanostructured system have also been listed. Of particular note is the peak mass activity towards the oxidation of methanol for the nanostructured structures, which was found to be 279 ± 4 A/g, significantly higher than the other catalyst systems in comparison. The specific activity and mass activity towards the oxidation of ethanol are also listed in Table 5.2. Figure 5.5 shows closely the onset of the catalytic peak measured in the positive sweep for both films. It can be observed for both fuels that the onset of the peak is reduced in the nanostructured platinum compared to the non-templated electrode; this is desirable for use in fuel cells, as working at a lower overpotential is more economical. This demonstrates that the nanostructured morphology provides a route to enhance the activity of platinum per gram over the conventional nanoparticle morphology. It has been proposed that, for the oxygen reduction reaction, enhanced catalytic effects found in ordered nanostructures compared to unstructured or nanoparticle surfaces are due to a higher concentration of the more active (111) and (100) sites and a reduction in less active edge sites[54].

Table 5.1. Observed specific area, specific activity and mass activity for nanostructured 'single diamond' and non-templated electrodes, compared to previously reported values for other commercial and nanostructured platinum catalysts measured under the same conditions (0.5M H_2SO_4 + 0.5M methanol, 50 mV/s).

Sample	Specific Area (m^2/g)	Specific Activity (A/m^2)	Mass Activity (A/g)
Nanostructured Pt	42 ± 2	6.3 ± 0.5	279 ± 4
Non-templated Pt	2.0 ± 0.5	1.0 ± 0.5	3 ± 1
Pt/c[55,151]	62.6 – 72.8	1.2 - 4.0	87.3 -214.2
Platinum black[55]	22.2	2.4	48.0
Gyroid[55]	15.6	2.6	40.8

Table 5.2. Observed specific area, specific activity and mass activity for nanostructured 'single diamond' and non-templated electrodes measured under the conditions 0.5M H_2SO_4 + 0.5M ethanol, 50 mV/s.

Sample	Specific Area (m^2/g)	Specific Activity (A/m^2)	Mass Activity (A/g)
Nanostructured Pt	42 ± 2	3.2 ± 0.2	130 ± 20
Non-templated Pt	2.0 ± 0.5	0.60 ± 0.09	1.9 ± 0.3

Stability with respect to repeat cycling is the second major area for improvement in platinum catalysts. A 'single diamond' electrode was cycled 3,000 times in 0.5 M H_2SO_4 between -0.3 and 1 V vs. Ag/AgCl at 50 mV/s. After this test the specific activity was found to be 12.7 m^2/g, as shown in Figure 5.6a, which is a percentage loss comparable with commercial Pt/C catalysts. However, these 'single diamond' structures maintain high specific activity for methanol oxidation, resulting in a mass activity of 110 A/g, as shown in Figure 5.6b, comparable with initial measurements of commercial Pt/C catalysts.

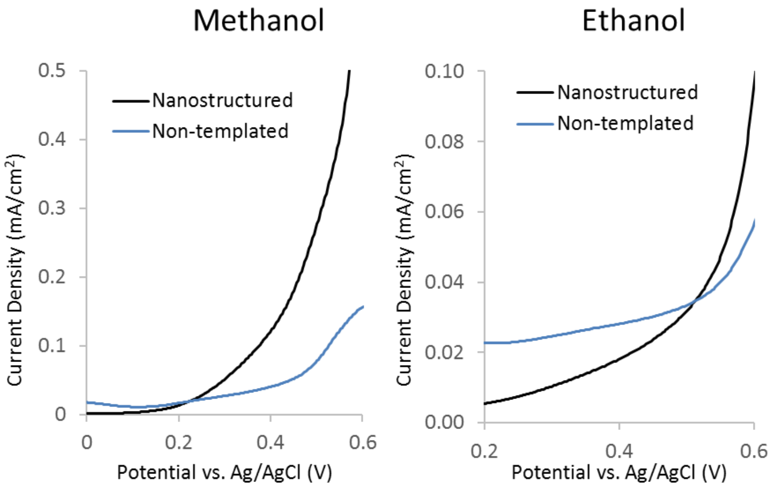

Figure 5.5. Representitive CV measurements highlighting onset potential for phytantriol-directed and non-templated electrodes in 0.5 M ethanol/methanol + 0.5 M H_2SO_4, cycled between -0.3 V and 1 V vs. Ag/AgCl at 50 mV/s. Current density was normalised according to the measured electroactive surface area.

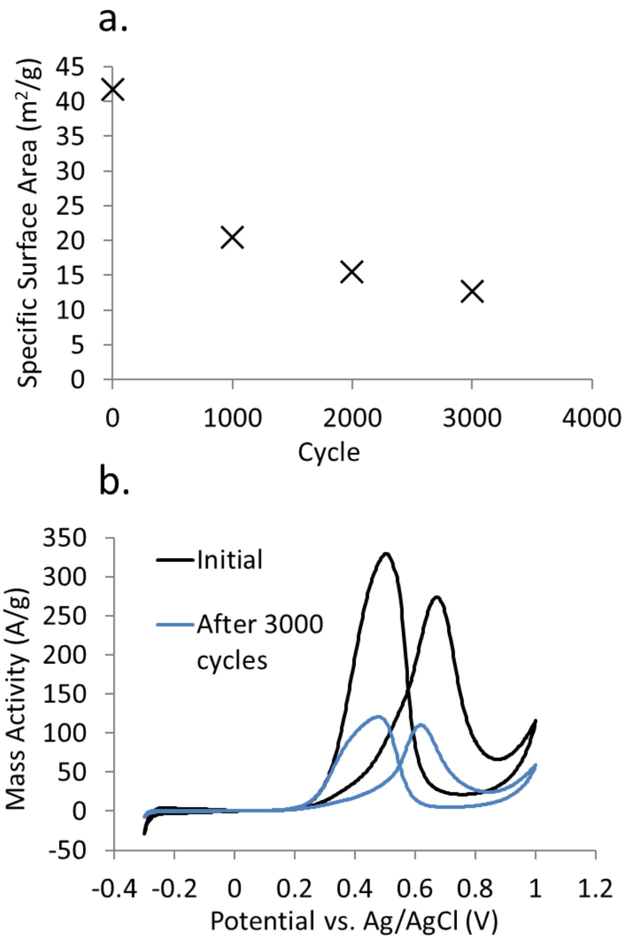

Figure 5.6. Stability of a lipid templated platinum nanostructure with specific surface area plotted in respect to time (a) and the mass activity before and after 3,000 cycles measured in a solution of 0.5M methanol and 0.5M H_2SO_4 at 50 mV/s (b).

5.3.3 Electrodeposition of lipid templated platinum nanostructures onto porous carbon gas diffusion layers

These results demonstrate that, as catalysts, lipid templated ordered nanostructures show enhanced mass activity and stability when compared to unstructured platinum and commercial platinum catalysts. However, nanostructures produced on solid non-porous supports, such as gold or glassy carbon, are incompatible with conventional fuel cell design, as they do not allow for the flow of fuel through the system. In contrast, fuel is able to flow through Pt/C catalysts due to the porous nature of the carbon support. In order to demonstrate that these nanostructured films could be incorporated into conventional fuel cell design, phytantriol-directed platinum was directly deposited onto commercial carbon paper. Using the same technique as for the gold disc electrodes, platinum was deposited onto carbon paper P50 and T03. Deposition transients for phytantriol-directed and non-templated deposition are shown in Figure 5.7 and representative cyclic voltammetry measurements of P50 electrodes with nanostructured and non-templated platinum are shown in Figure 5.8; in both cases the characteristic peaks of platinum can be observed. The surface area for the phytantriol-directed electrodes was found to be 11.7 ± 0.9 m^2/g, which is lower than when deposited onto polished gold. This may be due to phytantriol failing to fully coat the electrode, potentially allowing for areas of non-templated deposition. Another reason for the decrease may be reduced deposition efficiency; currently the estimate of platinum mass assumes 100% efficiency in the electrodeposition process.

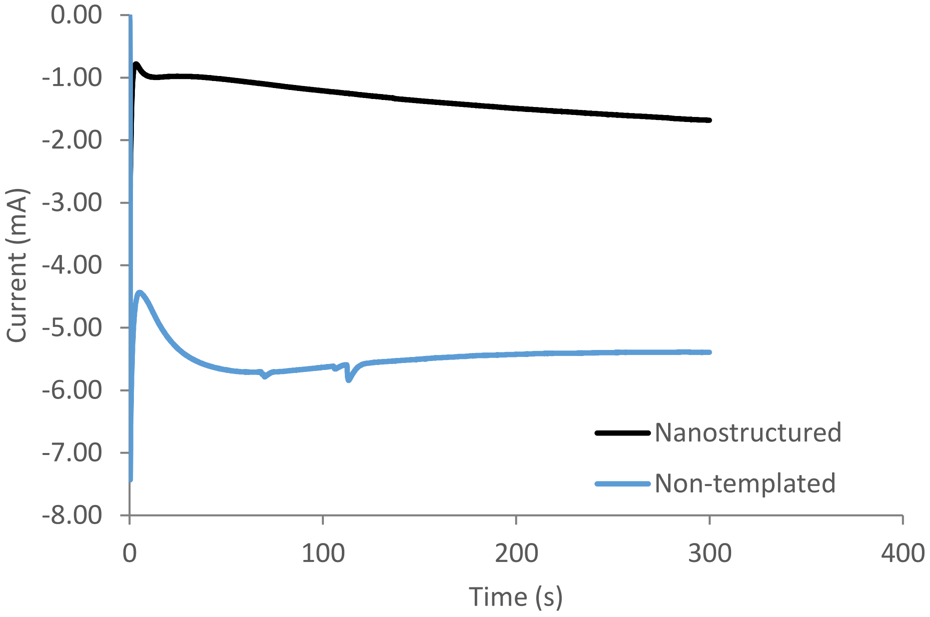

Figure 5.7. Deposition transient of phytantriol-directed platinum onto P50 carbon paper at -0.25V.

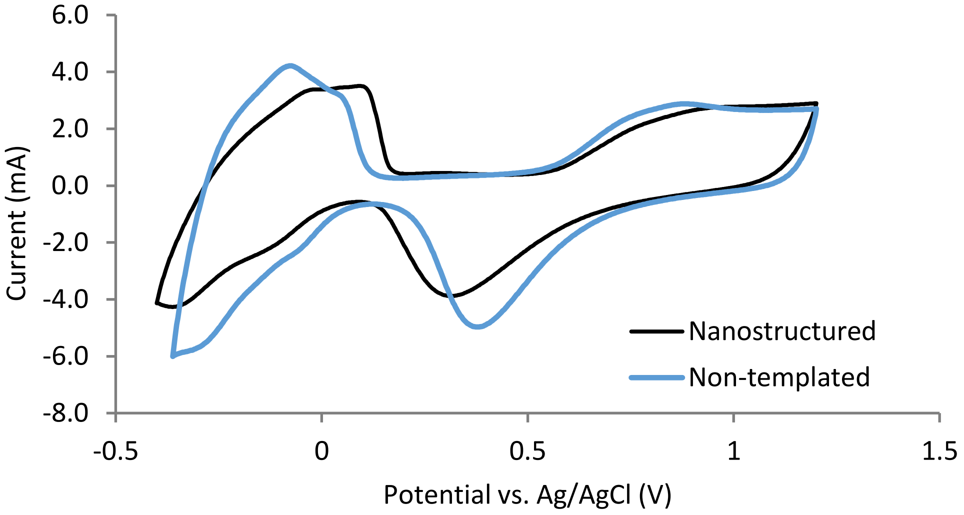

Figure 5.8. CVs of nanostructured and un-templated platinum deposited onto P50 carbon paper in (a) 0.5 M H_2SO_4 measured at 200 mV/s.

SEM measurements of the carbon surface after phytantriol-directed deposition in Figure 5.9 show that the porous nature of the carbon structure is unaffected by the platinum deposition, confirming that flow of fuel should still be possible through the layer. Additionally, EDX measurements confirmed the presence of platinum deposited onto the carbon through phytantriol. TEM images taken of platinum scraped off of the carbon substrate are shown in Figure 5.10. In Figure 5.10a, dark regions show deposited platinum and the lighter regions are carbon; these results appear to show that particles of platinum are deposited rather than a continuous film, which has been observed on solid substrates[3]. Alternatively, the presence of particles may be due to the destructive procedure for preparing samples for TEM measurements. In Figure 5.10b, a porous nanowire structure can be observed with a similar morphology to that previously observed for 'single diamond' structures. A simulated nanowire structure, independently scaled, has been super imposed onto the image to show that the repeat distance of the observed structure matches with theoretical predictions.

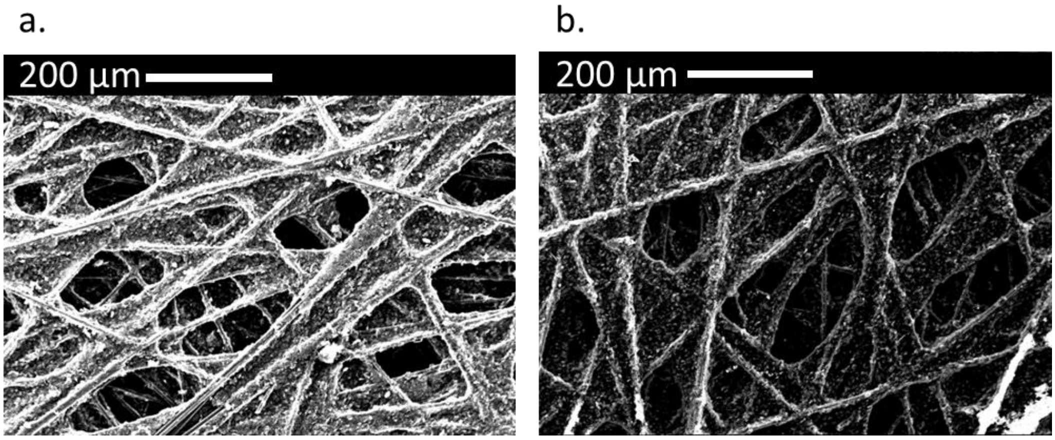

Figure 5.9. SEM images of P50 carbon paper, taken before (a) and after (b) electrodeposition of phytantriol-directed platinum.

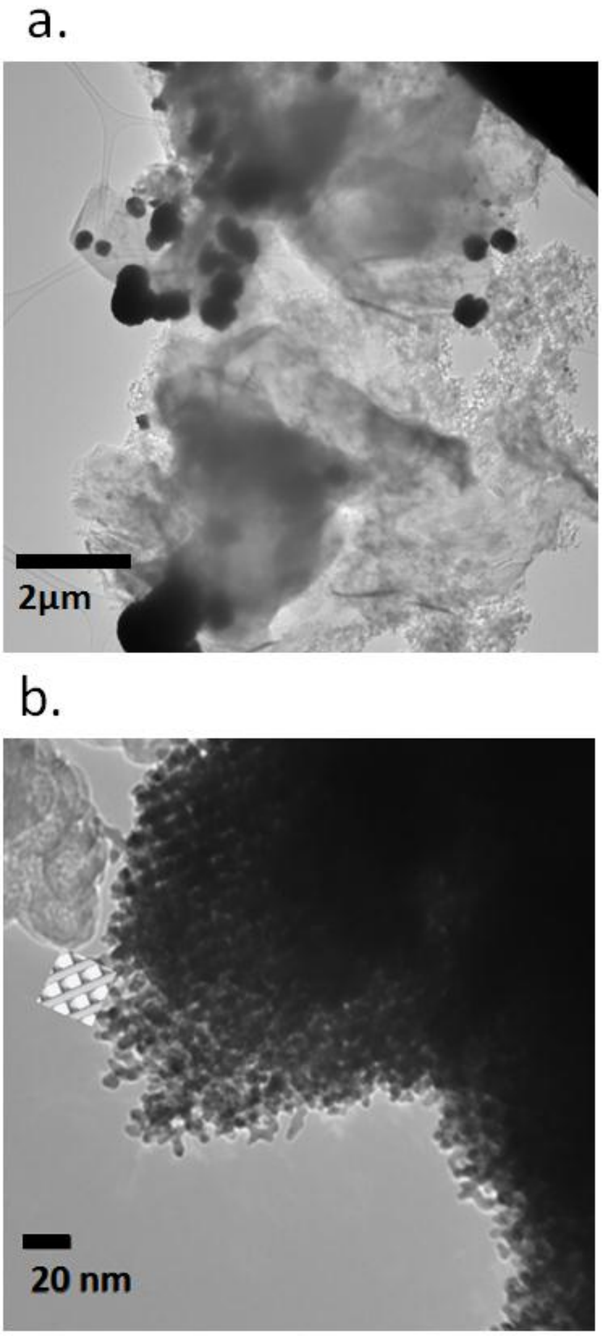

Figure 5.10. TEM images of electrodeposited nanostructured platinum. Lighter regions are carbon and darker, higher contrast regions are platinum depositions. An independently scaled simulation of ‘single diamond’ structure has been super imposed onto image b for comparison.

A SAXS measurement was taken of a nanostructured platinum film deposited onto T03 carbon paper, the 2D image and radial integration are shown in Figure 5.11. The radial integration shows a slight peak at around 0.011 Å^{-1}, which corresponds to a lattice parameter of a = 154 Å for a 'single diamond' structure featuring Fd3m symmetry. This is comparable to lattice parameters measured for platinum deposited onto gold in this thesis and in the literature[45]; this suggests the same morphology is adopted when depositing onto porous carbon.

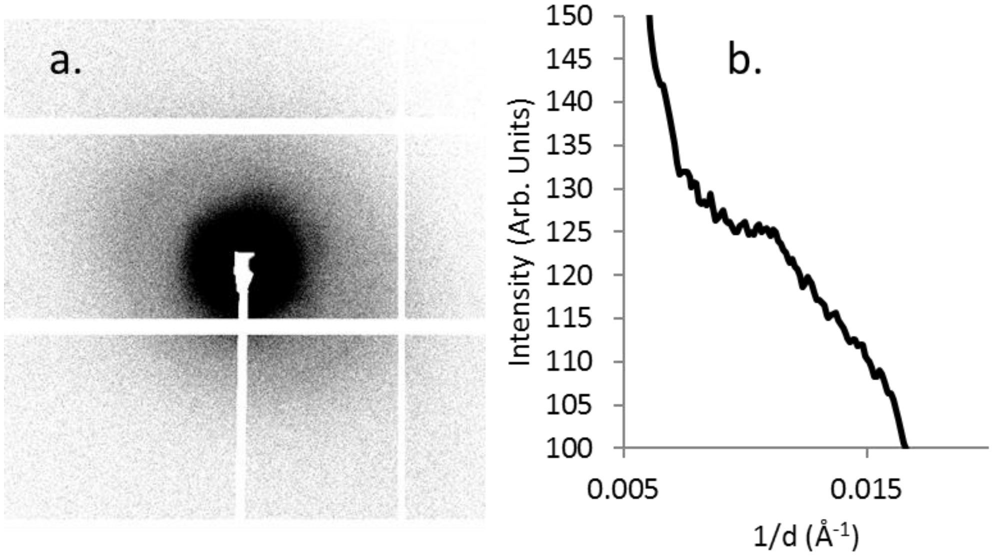

Figure 5.11. SAXS image of nanostructured platinum deposited onto T03 carbon paper (a) and the corresponding radial integration (b).

Finally, phytantriol-directed platinum on P50 was evaluated as a catalyst for the oxidation of ethanol, as shown in Figure 5.12. For comparison, nanostructured platinum and a non-templated platinum on gold are also shown. The peak current density for both nanostructured electrodes was comparable, 0.25 ± 0.03 mA/cm^2 for the gold substrate and 0.21 ± 0.01 mA/cm^2 on the carbon substrate; both electrodes were observed to greatly outperform the non-templated platinum electrode. Further work must be undertaken to optimise the deposition onto porous carbon in order to match specific areas and thus mass activity found when depositing onto polished electrodes. Further enhancements may be achieved in the future by producing 'single diamond' platinum alloys[130] or through the use of polymer coatings, to further enhance the activity of platinum catalysts[152].

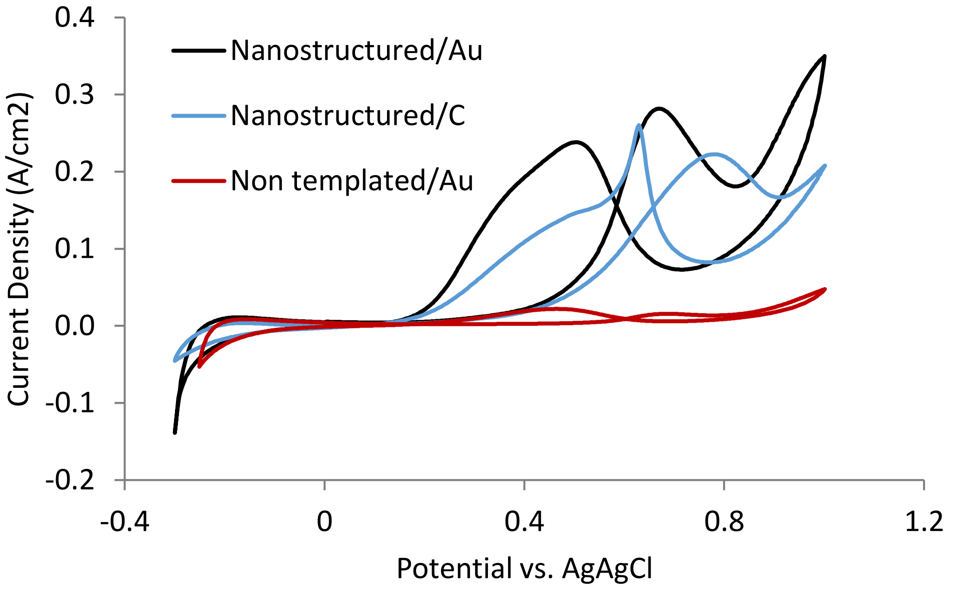

Figure 5.12. Representitive CV measurements for phytantriol-directed electrodes on polished gold and P50 carbon paper and, for comparison, non-templated electrodes in 0.5 M ethanol + 0.5 M H_2SO_4, cycled between -0.3 V and 1 V vs. Ag/AgCl at 20 mV/s. Current density was normalised according to the measured electroactive surface area.

5.4 CONCLUSIONS

Platinum nanostructures featuring a 'single diamond' morphology have been fabricated with a specific surface area of 42 ± 1 m^2/g. Measurements of the catalytic response to the methanol and ethanol oxidation reaction were promising, showing higher peak specific and mass activities in nanostructured films than in unstructured films, as well as in other commercial catalysts for the methanol reaction. Lipid cubic phase templating is highly versatile, potentially allowing for direct deposition onto any conductive substrate, such as the porous carbon demonstrated in this chapter. Moreover, ‘single diamond’ structures deposited onto porous carbon and polished gold substrates exhibit comparable specific activity for the oxidation of ethanol. These results suggest that phytantriol-directed platinum nanostructures offer a practical way to incorporate ordered 3D nanostructures into conventional fuel cell design.

6 CONCLUSIONS AND FUTURE DIRECTIONS

6.1 CONCLUSIONS

In summary, several studies were performed to investigate the phase behaviour of thin lipid films, their utilisation as soft templates for the electrodeposition of aligned platinum nanostructures and the application of this mesoporous platinum for use in direct alcohol fuel cells.

Through an experimental and theoretical study of the thermodynamics of thin films of lipid cubic phase, it was demonstrated that adding glycerol progressively lowers the humidity at which Q_{II} phase films are stable, without affecting their lattice parameter[1]. This work facilitates the study and application of Q_{II} phases in a much wider range of environments, without the possibility of dehydration collapsing the cubic structure. Through the addition of glycerol, it was also possible to study the orientation adopted by thin Q_{II} films. The Q_{II}^G and the Q_{II}^D phases were observed to be reproducibly orientated with the (110) and the (111) facets aligned parallel to the substrate respectively, up to a measured thickness of 1.4 µm[2]. These results agreed with theoretical predictions based on the minimization of interfacial energy.

By using thin lipid cubic phase films as a template, nanostructured platinum was electrodeposited, producing a high surface area of 42 ± 1 m^2/g. SAXS measurements provided evidence of an Fd3m structure, which was shown to feature uniaxial alignment in out-of-plane SAXS measurements. Further investigations into the mechanism for alignment were performed using SAXS measurements of the platinum films with and without the lipid template. The data collected in this study demonstrated that these orientated platinum structures were templated by un-orientated polydomain lipid cubic films. This suggests that the Q_{II}^{D} phase formed by the lipid film on the substrate features a region of interfacially driven alignment, rising approximately 3 µm from the lipid/substrate interface[3].

In order to further investigate the growth of this nanostructured platinum, a new measurement was developed, using SAXS to monitor the real-time growth of mesoporous platinum during electrodeposition. To facilitate this technique, a custom electrochemical cell for use on a SAXS beam was designed and produced. Previously, it was demonstrated that platinum films featuring 'single diamond' (Fd3m) morphology can be produced from 'double diamond' (Pn3m) lipid templates; the difference in symmetry providing additional scattering signals unique to the metal. Taking advantage of this, data was presented of simultaneous in-situ SAXS / electrochemical measurements allowing new observations of the platinum nanostructure growing within the lipid template. This permitted the correlation of the nanostructures growth with the deposition current density and observations of the evolution of orientational and lateral ordering of the lipid and platinum, during deposition and after template removal. This study produced a number of important results, shedding light on observations made previously on the metal films after template removal. Namely that the metal shows: more lateral disorder than the lipid template, characterised by broader Bragg peaks; a slight elongational distortion perpendicular to the plane of the electrode, shown by a non-cubic unit cell; and more orientational ordering. These *in situ* results demonstrated that the mesoporous films grow with cubic symmetry, and therefore that the rhombohedral distortion occurs after template removal, but also that the lateral disorder is present as the mesoporous film grows. Conversely, the lipid template shows orientational disorder and is polydomain, however the deposited platinum structure is initially highly orientated with the (111) plane aligned parallel to the substrate. As the film becomes thicker, it becomes un-aligned, consistent with the presence of a layer of the lipid template close to the electrode, which is oriented by the surface. In other periodic metal nanomaterials deposited within any of the normal topology liquid crystal, mesoporous silica or block copolymer templates previously published, the template and emerging metal have the same symmetry, preventing a similar study in other systems.

In addition, the techniques developed in this work allowed for the observation of direct evidence for an Fd3m structure with tuneable dimensions from the phytantriol/Brij 56 system. This had not previously been possible with conventional transmission SAXS, as the addition of Brij 56 to the phytantriol template resulted in more disordered platinum films, which produced a single broad peak in the scattering pattern. By measuring the samples in the out-of-plane configuration, alignment of the lattice-tuned films was observed, confirming the Fd3m morphology.

Nanostructured platinum films possessed enhanced catalytic response to the oxidation of methanol and ethanol when compared to non-templated platinum, with respect to both the mass and area normalised activity. Furthermore, promising results were shown in stability testing, with comparable percentage area loss to commercial nanoparticle systems, but with maintained high specific activity. This resulted in an endpoint mass activity towards the oxidation of methanol comparable with initial measurements of platinum nanoparticle catalysts.

Direct electrodeposition of nanostructured platinum onto porous carbon paper was demonstrated, with comparable specific activity for the oxidation of ethanol measured. This is an important result, as it demonstrates potential for the practical incorporation of 3D ordered nanostructures into conventional fuel cell design, which would not be possible with other fabrication routes, such as by directed silica or block copolymer. The technique demonstrated shows a means to produce nanostructured platinum directly onto materials compatible with conventional fuel cells, in a manner that other templating methods would not functionally allow. These results show that phytantriol-directed platinum nanostructures offer a practical way to incorporate ordered 3D nanostructures into conventional fuel cell design.

6.2 FUTURE DIRECTIONS

The work described in this thesis has the potential to be continued in several directions. The protocols for fabricating and characterising platinum nanostructures may be applied to new materials with many possible new applications. Perhaps the most relevant to current technological needs, would be to build upon the work studying nanostructured catalysts for fuel cells and to develop a 3D nanostructured platinum alloy deposited onto porous conducting supports, for use in an alcohol and hydrogen fuel cell. Nanostructured platinum alloys that could be incorporated in conventional fuel cell design have the potential to significantly improve performance and lower cost of fuel cell production, by reducing the amount of precious metal required.

The first area to be investigated would be the application of 'single diamond' nanostructures to the oxygen reduction reaction for use in alcohol and hydrogen fuel cell cathodes. Whilst the oxidation of alcohols has been thoroughly characterised, these structures have yet to be tested as cathodes for the oxygen reduction reaction, which is important for both alcohol and hydrogen fuel cells devices. Previous studies have shown enhanced catalytic performance from mesoporous platinum with gyroid morphology from block co-polymer and silica templating routes, hypothesised to be due to a lack of less active edge sites when compared to nanoparticle materials[54], so it would be expected that 'single diamond' platinum structures would see similar enhancements with the added benefit of ease of fabrication.

The next area of interest would be in the deposition of alloyed nanostructured materials, such as Pt/Ru[153] and Pt/Ru/Cu, with an aim to improve resistance to poisoning and further reduce the amount of precious metal required. Potentially a two-layered nanostructured material could be developed as an analogue to core shell nanoparticles, with a thin layer of platinum coating a cheaper bulk material. Finally, current procedures for electrodeposition onto porous carbon gas diffusion layers would need to be optimised and scaled up to allow for the mesoporous films to be evaluated in a real fuel cell test system. Whilst comparable activity per unit area was achieved here, nanostructures deposited onto carbon substrates were observed to feature lower specific surface area, resulting in reduced mass activity. Experiments would need to be performed to improve specific surface area, optimising the deposition conditions, where factors such as overpotential, precursor solution and deposition can be varied. In addition, electroless deposition has been demonstrated by Akbar as a route to produce powders with identical morphologies to the electrodeposited films[9]. These could be used to create an ink for patterning a carbon support, implementing standard industry techniques, as used to produce coatings of nanoparticle catalysts.

7 REFERENCES

1. Richardson, S. J. *et al.* Glycerol prevents dehydration in lipid cubic phases. *Chem. Commun.* (2015). doi:10.1039/C5CC03771A

2. Richardson, S. J. *et al.* Predicting the Orientation of Lipid Cubic Phase Films. *Langmuir* **30,** 13510–13515 (2014).

3. Richardson, S. J. *et al.* Aligned platinum nanowire networks from surface-oriented lipid cubic phase templates. *Nanoscale* **8,** 2850–2856 (2016).

4. Richardson, S. J. *et al.* Watching Mesoporous Metal Films Grow During Templated Electrodeposition with In Situ SAXS. In publication 2016.

5. Squires, A. Bending Energetics and Phase Transition Kinectics in Type II Mesophases formed by Hydrated 2LA/DLPC. (Imperial College, 2002).

6. Larsson, K., Fontell, K. & Krog, N. Structural relationships between lamellar, cubic and hexagonal phases in monoglyceride-water systems. Possibility of cubic structures in biological systems. *Chem. Phys. Lipids* **27,** 321–328 (1980).

7. Fontell, K. Cubic phases in surfactant and surfactant-like lipid systems. *Colloid Polym. Sci.* **268,** 264–285 (1990).

8. Dong, Y.-D., Larson, I., Hanley, T. & Boyd, B. J. Bulk and Dispersed Aqueous Phase Behavior of Phytantriol: Effect of Vitamin E Acetate and F127 Polymer on Liquid Crystal Nanostructure. *Langmuir* **22,** 9512–9518 (2006).

9. Akbar, S. Novel synthesis of nanostructured platinum materials via true liquid crystal templating utilising phytantriol as a structure directing agent. (University of Reading, 2012).

10. Israelachvili, J. *Intermolecular and Surface Forces*. (Academic Press, 2011).

11. Schoen, A. H. Infinite periodic minimal surfaces without self-intersections. (1970).

12. Barauskas, J. & Landh, T. Phase Behavior of the Phytantriol/Water System. *Langmuir* **19,** 9562–9565 (2003).

13. Seddon, A. M., Lotze, G., Plivelic, T. S. & Squires, A. M. A Highly Oriented Cubic Phase Formed by Lipids under Shear. *J. Am. Chem. Soc.* **133,** 13860–13863 (2011).

14. Squires, A. M. *et al.* Experimental Evidence for Proposed Transformation Pathway from the Inverse Hexagonal to Inverse Diamond Cubic Phase from Oriented Lipid Samples. *Langmuir* **31,** 7707–7711 (2015).

15. Oka, T. & Hojo, H. Single Crystallization of an Inverse Bicontinuous Cubic Phase of a Lipid. *Langmuir* **30,** 8253–8257 (2014).

16. Squires, A. M., Hallett, J. E., Beddoes, C. M., Plivelic, T. S. & Seddon, A. M. Preparation of Films of a Highly Aligned Lipid Cubic Phase. *Langmuir* **29,** 1726–1731 (2013).

17. Rittman, M. *et al.* Control and Analysis of Oriented Thin Films of Lipid Inverse Bicontinuous Cubic Phases Using Grazing Incidence Small-Angle X-ray Scattering. *Langmuir* **29,** 9874–9880 (2013).

18. Landau, E. M. & Rosenbusch, J. P. Lipidic cubic phases: a novel concept for the crystallization of membrane proteins. *Proc. Natl. Acad. Sci.* **93,** 14532–14535 (1996).

19. Caffrey, M. A comprehensive review of the lipid cubic phase or in meso method for crystallizing membrane and soluble proteins and complexes. *Acta Crystallogr. Sect. F Struct. Biol. Commun.* **71,** 3–18 (2015).

20. Caffrey, M. A lipid's eye view of membrane protein crystallization in mesophases. *Curr. Opin. Struct. Biol.* **10,** 486–497 (2000).

21. Caffrey, M. & Cherezov, V. Crystallizing membrane proteins using lipidic mesophases. *Nat. Protoc.* **4,** 706–731 (2009).

22. Caffrey, M., Li, D., Howe, N. & Shah, S. T. A. 'Hit and run' serial femtosecond crystallography of a membrane kinase in the lipid cubic phase. *Philos. Trans. R. Soc. Lond. B Biol. Sci.* **369,** 20130621 (2014).

23. Nguyen, T.-H., Hanley, T., Porter, C. J. H. & Boyd, B. J. Nanostructured liquid crystalline particles provide long duration sustained-release effect for a poorly water soluble drug after oral administration. *J. Controlled Release* **153,** 180–186 (2011).

24. Wu, H. *et al.* A novel small Odorranalectin-bearing cubosomes: Preparation, brain delivery and pharmacodynamic study on amyloid-β25–35-treated rats following intranasal administration. *Eur. J. Pharm. Biopharm.* **80,** 368–378 (2012).

25. Bender, J. *et al.* Lipid cubic phases for improved topical drug delivery in photodynamic therapy. *J. Controlled Release* **106,** 350–360 (2005).

26. Bender, J., Simonsson, C., Smedh, M., Engström, S. & Ericson, M. B. Lipid cubic phases in topical drug delivery: Visualization of skin distribution using two-photon microscopy. *J. Controlled Release* **129,** 163–169 (2008).

27. Shah, J. C., Sadhale, Y. & Chilukuri, D. M. Cubic phase gels as drug delivery systems. *Adv. Drug Deliv. Rev.* **47,** 229–250 (2001).

28. Negrini, R. & Mezzenga, R. pH-Responsive Lyotropic Liquid Crystals for Controlled Drug Delivery. *Langmuir* **27,** 5296–5303 (2011).

29. Lawrence, M. J. Surfactant systems: their use in drug delivery. *Chem. Soc. Rev.* **23,** 417–424 (1994).

30. Fong, W.-K., Hanley, T. & Boyd, B. J. Stimuli responsive liquid crystals provide ‘on-demand’ drug delivery in vitro and in vivo. *J. Controlled Release* **135,** 218–226 (2009).

31. Zhang, H. & Kim, J.-C. Preparation and photothermal induced release from cubic phase containing gold nanoparticle. *Colloids Surf. Physicochem. Eng. Asp.* **465,** 59–66 (2015).

32. Bilewicz, R., Rowiński, P. & Rogalska, E. Modified electrodes based on lipidic cubic phases. *Bioelectrochemistry* **66,** 3–8 (2005).

33. Chen, Y. *et al.* Humidity-Modulated Phase Control and Nanoscopic Transport in Supramolecular Assemblies. *J. Phys. Chem. B* **118,** 3207–3217 (2014).

34. Vauthey, S. *et al.* Release of Volatiles from Cubic Phases: Monitoring by Gas Sensors. *J. Dispers. Sci. Technol.* **21,** 263–278 (2000).

35. Akbar, S., Elliott, J. M., Rittman, M. & Squires, A. M. Facile Production of Ordered 3D Platinum Nanowire Networks with ‘Single Diamond’ Bicontinuous Cubic Morphology. *Adv. Mater.* **25,** 1160–1164 (2013).

36. Rioux, R. M., Song, H., Hoefelmeyer, J. D., Yang, P. & Somorjai, G. A. High-Surface-Area Catalyst Design: Synthesis, Characterization, and Reaction Studies of Platinum Nanoparticles in Mesoporous SBA-15 Silica†. *J. Phys. Chem. B* **109,** 2192–2202 (2005).

37. Nandiyanto, A. B. D., Kim, S.-G., Iskandar, F. & Okuyama, K. Synthesis of spherical mesoporous silica nanoparticles with nanometer-size controllable pores and outer diameters. *Microporous Mesoporous Mater.* **120,** 447–453 (2009).

38. Bach, U. *et al.* Solid-state dye-sensitized mesoporous TiO2 solar cells with high photon-to-electron conversion efficiencies. *Nature* **395,** 583–585 (1998).

39. Sauvage, F. *et al.* Dye-Sensitized Solar Cells Employing a Single Film of Mesoporous TiO $_2$ Beads Achieve Power Conversion Efficiencies Over 10%. *ACS Nano* **4,** 4420–4425 (2010).

40. Demetriadou, A., Oh, S. S., Wuestner, S. & Hess, O. A tri-helical model for nanoplasmonic gyroid metamaterials. *New J. Phys.* **14,** 83032 (2012).

41. Attard, G. S. Mesoporous Platinum Films from Lyotropic Liquid Crystalline Phases. *Science* **278,** 838–840 (1997).

42. Elliott, J. M. & Owen, J. R. Electrochemical impedance characterisation of a nanostructured (mesoporous) platinum film. *Phys. Chem. Chem. Phys.* **2,** 5653–5659 (2000).

43. Montalvo, G., Valiente, M. & Rodenas, E. Rheological Properties of the L Phase and the Hexagonal, Lamellar, and Cubic Liquid Crystals of the CTAB/Benzyl Alcohol/Water System. *Langmuir* **12,** 5202–5208 (1996).

44. Elliott, J. M. *et al.* A generic approach to electrodes with novel controllable continuous nanostructures. *J. New Mater. Electrochem. Syst.* 239–241 (1999).

45. Akbar, S., Elliott, J. M., Rittman, M. & Squires, A. M. Facile Production of Ordered 3D Platinum Nanowire Networks with 'Single Diamond' Bicontinuous Cubic Morphology. *Adv. Mater.* **25,** 1160–1164 (2013).

46. Zhu, C., Guo, S. & Dong, S. Rapid, General Synthesis of PdPt Bimetallic Alloy Nanosponges and Their Enhanced Catalytic Performance for Ethanol/Methanol Electrooxidation in an Alkaline Medium. *Chem. – Eur. J.* **19,** 1104–1111 (2013).

47. Antolini, E., Salgado, J. R. C. & Gonzalez, E. R. The methanol oxidation reaction on platinum alloys with the first row transition metals: The case of Pt–Co and –Ni alloy electrocatalysts for DMFCs: A short review. *Appl. Catal. B Environ.* **63,** 137–149 (2006).

48. Lee, K.-S. *et al.* Electrocatalytic activity and stability of Pt supported on Sb-doped SnO2 nanoparticles for direct alcohol fuel cells. *J. Catal.* **258,** 143–152 (2008).

49. Li, X. & Faghri, A. Review and advances of direct methanol fuel cells (DMFCs) part I: Design, fabrication, and testing with high concentration methanol solutions. *J. Power Sources* **226,** 223–240 (2013).

50. Kamarudin, M. Z. F., Kamarudin, S. K., Masdar, M. S. & Daud, W. R. W. Review: Direct ethanol fuel cells. *Int. J. Hydrog. Energy* **38,** 9438–9453 (2013).

51. Wasmus, S. & Küver, A. Methanol oxidation and direct methanol fuel cells: a selective review1. *J. Electroanal. Chem.* **461,** 14–31 (1999).

52. Gasteiger, H. A., Kocha, S. S., Sompalli, B. & Wagner, F. T. Activity benchmarks and requirements for Pt, Pt-alloy, and non-Pt oxygen reduction catalysts for PEMFCs. *Appl. Catal. B Environ.* **56,** 9–35 (2005).

53. Zhu, C., Du, D., Eychmüller, A. & Lin, Y. Engineering Ordered and Nonordered Porous Noble Metal Nanostructures: Synthesis, Assembly, and Their Applications in Electrochemistry. *Chem. Rev.* (2015). doi:10.1021/acs.chemrev.5b00255

54. Kibsgaard, J., Gorlin, Y., Chen, Z. & Jaramillo, T. F. Meso-Structured Platinum Thin Films: Active and Stable Electrocatalysts for the Oxygen Reduction Reaction. *J. Am. Chem. Soc.* **134,** 7758–7765 (2012).

55. Cheng, C.-F. *et al.* Nanoporous gyroid platinum with high catalytic activity from block copolymer templates via electroless plating. *NPG Asia Mater.* **7,** e170 (2015).

56. Kibsgaard, J., Jackson, A. & Jaramillo, T. F. Mesoporous platinum nickel thin films with double gyroid morphology for the oxygen reduction reaction. *Nano Energy* doi:10.1016/j.nanoen.2016.05.005

57. Bard, A. J. & Faulkner, Larry R. *Electrochemical methods: fundamentals and applications*. (Wiley, 2001).

58. Gollas, B., Elliott, J. M. & Bartlett, P. N. Electrodeposition and properties of nanostructured platinum films studied by quartz crystal impedance measurements at 10 MHz. *Electrochimica Acta* **45,** 3711–3724 (2000).

59. *Encyclopedia of Electrochemistry, Instrumentation and Electroanalytical Chemistry*. (Wiley-VCH, 2003).

60. Frelink, T., Visscher, W. & van Veen, J. A. R. The third anodic hydrogen peak on platinum; Subsurface H2 adsorption. *Electrochimica Acta* **40,** 545–549 (1995).

61. Doña Rodríguez, J. M., Herrera Melián, J. A. & Pérez Peña, J. Determination of the Real Surface Area of Pt Electrodes by Hydrogen Adsorption Using Cyclic Voltammetry. *J. Chem. Educ.* **77,** 1195 (2000).

62. Ashcroft, N. W. & Mermin, N. D. *Solid State Physics*. (Cengage Learning, 1976).

63. Schnablegger, H. & Singh, Y. *The SAXS Guide*. (Anton Paar, 2011).

64. Detlef, S. GISAXS, staff.chess.cornell.edu. (2010).

65. Muller, F., Salonen, A. & Glatter, O. Phase behavior of Phytantriol/water bicontinuous cubic< i> Pn3m</i> cubosomes stabilized by Laponite disc-like particles. *J. Colloid Interface Sci.* **342,** 392–398 (2010).

66. Kondoh, E. ELLIPSHEET: Spreadsheet Ellipsometry. (2001). www.ccn.yamanashi.ac.jp/~kondoh/ellips_e

67. Fujiwara, H. *Spectroscopic Ellipsometry: Principles and Applications*. (John Wiley & Sons, 2007).

68. Cobet, C. in *Ellipsometry of Functional Organic Surfaces and Films* (eds. Hinrichs, K. & Eichhorn, K.-J.) 1–26 (Springer Berlin Heidelberg, 2014).

69. Vernon-Parry, K. D. Scanning electron microscopy: an introduction. *III-Vs Rev.* **13,** 40–44 (2000).

70. Chen, Z. *et al.* Energy dispersive X-ray analysis on an absolute scale in scanning transmission electron microscopy. *Ultramicroscopy* **157,** 21–26 (2015).

71. Rochow, T. G. & Tucker, P. A. *Introduction to Microscopy by Means of Light, Electrons, X Rays, or Acoustics*. (Springer Science & Business Media, 2013).

72. Qiu, H. & Caffrey, M. The phase diagram of the monoolein/water system: metastability and equilibrium aspects. *Biomaterials* **21,** 223–234 (2000).

73. Clogston, J., Rathman, J., Tomasko, D., Walker, H. & Caffrey, M. Phase behavior of a monoacylglycerol:(Myverol 18-99K)/water system. *Chem. Phys. Lipids* **107,** 191–220 (2000).

74. Larsson, K. Aqueous dispersions of cubic lipid–water phases. *Curr. Opin. Colloid Interface Sci.* **5,** 64–69 (2000).

75. Rowiński, P., Bilewicz, R., Stébé, M.-J. & Rogalska, E. A Concept for Immobilizing Catalytic Complexes on Electrodes: Cubic Phase Layers for Carbon Dioxide Sensing. *Anal. Chem.* **74,** 1554–1559 (2002).

76. Rittman, M. *et al.* Control and Analysis of Oriented Thin Films of Lipid Inverse Bicontinuous Cubic Phases Using Grazing Incidence Small-Angle X-ray Scattering. *Langmuir* **29,** 9874–9880 (2013).

77. Squires, A. M., Hallett, J. E., Beddoes, C. M., Plivelic, T. S. & Seddon, A. M. Preparation of Films of a Highly Aligned Lipid Cubic Phase. *Langmuir* **29,** 1726–1731 (2013).

78. Nilsson, C. *et al.* PEGylation of Phytantriol-Based Lyotropic Liquid Crystalline Particles—The Effect of Lipid Composition, PEG Chain Length, and Temperature on the Internal Nanostructure. *Langmuir* (2014). doi:10.1021/la501411w

79. Pieranski, P., Sotta, P., Rohe, D. & Imperor-Clerc, M. Devil's Staircase–Type Faceting of a Cubic Lyotropic Liquid Crystal. *Phys. Rev. Lett.* **84,** 2409–2412 (2000).

80. Tan, K. M., Tay, C. M., Tjin, S. C., Chan, C. C. & Rahardjo, H. High relative humidity measurements using gelatin coated long-period grating sensors. *Sens. Actuators B Chem.* **110,** 335–341 (2005).

81. Lindell, K., Engblom, J., Engström, S., Jonströmer, M. & Carlsson, A. in *The Colloid Science of Lipids* (eds. Lindman, B. & Ninham, B. W.) 111–118 (Steinkopff, 1998).

82. Sagalowicz, L., Leser, M. E., Watzke, H. J. & Michel, M. Monoglyceride self-assembly structures as delivery vehicles. *Trends Food Sci. Technol.* **17,** 204–214 (2006).

83. Salvatore, S. *et al.* Tunable 3D Extended Self-Assembled Gold Metamaterials with Enhanced Light Transmission. *Adv. Mater.* **25,** 2713–2716 (2013).

84. Dolan, J. A. *et al.* Optical Properties of Gyroid Structured Materials: From Photonic Crystals to Metamaterials. *Adv. Opt. Mater.* **3,** 12–32 (2015).

85. Larsson, K. Aqueous dispersions of cubic lipid–water phases. *Curr. Opin. Colloid Interface Sci.* **5,** 64–69 (2000).

86. Chen, Y., Ma, P. & Gui, S. Cubic and Hexagonal Liquid Crystals as Drug Delivery Systems. *BioMed Res. Int.* **2014,** e815981 (2014).

87. Kulkarni, C. V., Wachter, W., Iglesias-Salto, G., Engelskirchen, S. & Ahualli, S. Monoolein: a magic lipid? *Phys. Chem. Chem. Phys.* **13,** 3004 (2011).

88. Snow, T., Rittman, M. & Squires, A. *YAX*. www.cunninglemon.com/projects.YAX

89. Gras, S. L. & Squires, A. M. Dried and hydrated X-ray scattering analysis of amyloid fibrils. *Methods Mol. Biol. Clifton NJ* **752,** 147–163 (2011).

90. Hoyt, L. F. New Table of the Refractive Index of Pure Glycerol at 20°C. *Ind. Eng. Chem.* **26,** 329–332 (1934).

91. Phytantriol basic information. www.chemicalbook.com/ProductChemicalPropertiesCB2141592_EN

92. Green, M. A. & Keevers, M. J. Optical properties of intrinsic silicon at 300 K. *Prog. Photovolt. Res. Appl.* **3,** 189–192 (1995).

93. Templer, R. H., Turner, D. D., Harper, P. & Seddon, J. M. Corrections to Some Models of the Curvature Elastic Energy of Inverse Bicontinuous Cubic Phases. *J. Phys. II* **5,** 1053–1065 (1995).

94. Slaughter, A. Masters thesis. (University of Reading, 2013).

95. Chung, H. & Caffrey, M. The curvature elastic-energy function of the lipid–water cubic mesophase. *Nature* **368,** 224–226 (1994).

96. Squires, A. M. *et al.* Kinetics and Mechanism of the Lamellar to Gyroid Inverse Bicontinuous Cubic Phase Transition. *Langmuir* **18,** 7384–7392 (2002).

97. Squires, A. *et al.* Kinetics and mechanism of the interconversion of inverse bicontinuous cubic mesophases. *Phys. Rev. E* **72,** (2005).

98. Felts, J. R., Onses, M. S., Rogers, J. A. & King, W. P. Nanometer Scale Alignment of Block-Copolymer Domains by Means of a Scanning Probe Tip. *Adv. Mater.* **26,** 2999–3002 (2014).

99. Zhang, X. *et al.* Porous platinum nanowire arrays for direct ethanol fuel cell applications. *Chem. Commun.* 195–197 (2009). doi:10.1039/B813830C

100. Mamaeva, V. *et al.* Mesoporous Silica Nanoparticles as Drug Delivery Systems for Targeted Inhibition of Notch Signaling in Cancer. *Mol. Ther.* **19,** 1538–1546 (2011).

101. Vallet-Regí, M., Balas, F. & Arcos, D. Mesoporous Materials for Drug Delivery. *Angew. Chem. Int. Ed.* **46,** 7548–7558 (2007).

102. Phan, S., Fong, W.-K., Kirby, N., Hanley, T. & Boyd, B. J. Evaluating the link between self-assembled mesophase structure and drug release. *Int. J. Pharm.* **421,** 176–182 (2011).

103. Beck, J. S. *et al.* A new family of mesoporous molecular sieves prepared with liquid crystal templates. *J. Am. Chem. Soc.* **114,** 10834–10843 (1992).

104. Shi, Y. *et al.* Ordered Mesoporous Metallic MoO2 Materials with Highly Reversible Lithium Storage Capacity. *Nano Lett.* **9,** 4215–4220 (2009).

105. Li, N. *et al.* Battery Performance and Photocatalytic Activity of Mesoporous Anatase TiO2 Nanospheres/Graphene Composites by Template-Free Self-Assembly. *Adv. Funct. Mater.* **21,** 1717–1722 (2011).

106. Li, B. *et al.* Mesoporous Tungsten Trioxide Polyaniline Nanocomposite as an Anode Material for High-Performance Lithium-Ion Batteries. *ChemNanoMat* **2,** 281–289 (2016).

107. Evans, S. A. G. *et al.* Detection of Hydrogen Peroxide at Mesoporous Platinum Microelectrodes. *Anal. Chem.* **74,** 1322–1326 (2002).

108. Teoh, L. G., Hon, Y. M., Shieh, J., Lai, W. H. & Hon, M. H. Sensitivity properties of a novel NO2 gas sensor based on mesoporous WO3 thin film. *Sens. Actuators B Chem.* **96,** 219–225 (2003).

109. Walcarius, A. Mesoporous Materials-Based Electrochemical Sensors. *Electroanalysis* n/a-n/a (2015). doi:10.1002/elan.201400628

110. Wen, Z., Zhu, L., Zhang, Z. & Ye, Z. Fabrication of gas sensor based on mesoporous rhombus-shaped ZnO rod arrays. *Sens. Actuators B Chem.* **208,** 112–121 (2015).

111. Ye, Y., Jo, C., Jeong, I. & Lee, J. Functional mesoporous materials for energy applications: solar cells, fuel cells, and batteries. *Nanoscale* **5,** 4584–4605 (2013).

112. Omer, L., Ruthstein, S., Goldfarb, D. & Talmon, Y. High-Resolution Cryogenic-Electron Microscopy Reveals Details of a Hexagonal-to-Bicontinuous Cubic Phase Transition in Mesoporous Silica Synthesis. *J. Am. Chem. Soc.* **131,** 12466–12473 (2009).

113. Wang, D. *et al.* A General Route to Macroscopic Hierarchical 3D Nanowire Networks. *Angew. Chem.* **116,** 6295–6299 (2004).

114. Crossland, E. J. W. *et al.* A Bicontinuous Double Gyroid Hybrid Solar Cell. *Nano Lett.* **9,** 2807–2812 (2009).

115. Wang, H. *et al.* Shape- and Size-Controlled Synthesis in Hard Templates: Sophisticated Chemical Reduction for Mesoporous Monocrystalline Platinum Nanoparticles. *J. Am. Chem. Soc.* **133,** 14526–14529 (2011).

116. Biggins, J. S., Warner, M. & Bhattacharya, K. Supersoft elasticity in polydomain nematic elastomers. *Phys. Rev. Lett.* **103,** 37802 (2009).

117. Yamashita, N. *et al.* Chemically directed self-assembly of perpendicularly aligned cylinders by a liquid crystalline block copolymer. *J. Mater. Chem. C* **3,** 2837–2847 (2015).

118. Vignolini, S. *et al.* A 3D Optical Metamaterial Made by Self-Assembly. *Adv. Mater.* **24,** OP23-OP27 (2012).

119. Latypova, L., Góźdź, W. T. & Pierański, P. Facets of Lyotropic Liquid Crystals. *Langmuir* **30,** 488–495 (2014).

120. Seddon, A. M., Hallett, J., Beddoes, C., Plivelic, T. S. & Squires, A. M. Experimental Confirmation of Transformation Pathways between Inverse Double Diamond and Gyroid Cubic Phases. *Langmuir* **30,** 5705–5710 (2014).

121. Paik, T., Ko, D.-K., Gordon, T. R., Doan-Nguyen, V. & Murray, C. B. Studies of Liquid Crystalline Self-Assembly of GdF3 Nanoplates by In-Plane, Out-of-Plane SAXS. *ACS Nano* **5,** 8322–8330 (2011).

122. Rittman, M., Frischherz, M., Burgmann, F., Hartley, P. G. & Squires, A. Direct visualisation of lipid bilayer cubic phases using Atomic Force Microscopy. *Soft Matter* **6,** 4058–4061 (2010).

123. Zhan, D., Velmurugan, J. & Mirkin, M. V. Adsorption/Desorption of Hydrogen on Pt Nanoelectrodes: Evidence of Surface Diffusion and Spillover. *J. Am. Chem. Soc.* **131,** 14756–14760 (2009).

124. De Wolff, P. M. On the lorentz factor for integrated intensities from azimuthal and radial diffractometer records of fiber patterns. *J. Polym. Sci.* **60,** S34–S36 (1962).

125. Liu, H. *et al.* A review of anode catalysis in the direct methanol fuel cell. *J. Power Sources* **155,** 95–110 (2006).

126. Vigier, F., Rousseau, S., Coutanceau, C., Leger, J.-M. & Lamy, C. Electrocatalysis for the direct alcohol fuel cell. *Top. Catal.* **40,** 111–121 (2006).

127. Kakati, N. *et al.* Anode Catalysts for Direct Methanol Fuel Cells in Acidic Media: Do We Have Any Alternative for Pt or Pt–Ru? *Chem. Rev.* **114,** 12397–12429 (2014).

128. Zhu, C., Du, D., Eychmüller, A. & Lin, Y. Engineering Ordered and Nonordered Porous Noble Metal Nanostructures: Synthesis, Assembly, and Their Applications in Electrochemistry. *Chem. Rev.* (2015). doi:10.1021/acs.chemrev.5b00255

129. Simões, F. C. *et al.* Electroactivity of tin modified platinum electrodes for ethanol electrooxidation. *J. Power Sources* **167,** 1–10 (2007).

130. Wang, M. *et al.* Electrochemical activated PtAuCu alloy nanoparticle catalysts for formic acid, methanol and ethanol electro-oxidation. *Electrochimica Acta* doi:10.1016/j.electacta.2015.07.157

131. Ge, X. *et al.* A Core-Shell Nanoporous Pt-Cu Catalyst with Tunable Composition and High Catalytic Activity. *Adv. Funct. Mater.* **23,** 4156–4162 (2013).

132. Chen, X., Cai, Z., Chen, X. & Oyama, M. Green synthesis of graphene-PtPd alloy nanoparticles with high electrocatalytic performance for ethanol oxidation. *J Mater Chem A* **2,** 315–320 (2014).

133. Du, W. *et al.* Platinum-Tin Oxide Core–Shell Catalysts for Efficient Electro-Oxidation of Ethanol. *J. Am. Chem. Soc.* **136,** 10862–10865 (2014).

134. Jaouen, F. *et al.* Recent advances in non-precious metal catalysis for oxygen-reduction reaction in polymer electrolyte fuel cells. *Energy Environ. Sci.* **4,** 114–130 (2010).

135. Jeon, I.-Y. *et al.* Facile, scalable synthesis of edge-halogenated graphene nanoplatelets as efficient metal-free eletrocatalysts for oxygen reduction reaction. *Sci. Rep.* **3,** (2013).

136. Deng, J. *et al.* Highly active reduction of oxygen on a FeCo alloy catalyst encapsulated in pod-like carbon nanotubes with fewer walls. *J. Mater. Chem. A* **1,** 14868 (2013).

137. Du, W. *et al.* Highly Active Iridium/Iridium–Tin/Tin Oxide Heterogeneous Nanoparticles as Alternative Electrocatalysts for the Ethanol Oxidation Reaction. *J. Am. Chem. Soc.* **133,** 15172–15183 (2011).

138. Gong, Y. *et al.* Boron- and Nitrogen-Substituted Graphene Nanoribbons as Efficient Catalysts for Oxygen Reduction Reaction. *Chem. Mater.* **27,** 1181–1186 (2015).

139. Guo, S., Zhang, S., Sun, X. & Sun, S. Synthesis of Ultrathin FePtPd Nanowires and Their Use as Catalysts for Methanol Oxidation Reaction. *J. Am. Chem. Soc.* **133,** 15354–15357 (2011).

140. Koenigsmann, C., Semple, D. B., Sutter, E., Tobierre, S. E. & Wong, S. S. Ambient Synthesis of High-Quality Ruthenium Nanowires and the Morphology-Dependent Electrocatalytic Performance of Platinum-

Decorated Ruthenium Nanowires and Nanoparticles in the Methanol Oxidation Reaction. *ACS Appl. Mater. Interfaces* **5,** 5518–5530 (2013).

141. Zhou, W.-P. *et al.* Morphology-dependent activity of Pt nanocatalysts for ethanol oxidation in acidic media: Nanowires versus nanoparticles. *Electrochimica Acta* **56,** 9824–9830 (2011).

142. Serrà, A., Gómez, E. & Vallés, E. Facile electrochemical synthesis, using microemulsions with ionic liquid, of highly mesoporous CoPt nanorods with enhanced electrocatalytic performance for clean energy. *Int. J. Hydrog. Energy* doi:10.1016/j.ijhydene.2015.04.095

143. Chen, X. *et al.* Platinum nanoflowers supported on graphene oxide nanosheets: their green synthesis, growth mechanism, and advanced electrocatalytic properties for methanol oxidation. *J. Mater. Chem.* **22,** 11284 (2012).

144. Yao, Z. *et al.* Highly efficient electrocatalytic performance based on Pt nanoflowers modified reduced graphene oxide/carbon cloth electrode. *J. Mater. Chem.* **22,** 13707–13713 (2012).

145. Xia, B. Y., Wu, H. B., Wang, X. & Lou, X. W. (David). One-Pot Synthesis of Cubic PtCu3 Nanocages with Enhanced Electrocatalytic Activity for the Methanol Oxidation Reaction. *J. Am. Chem. Soc.* **134,** 13934–13937 (2012).

146. Guo, Y.-G., Hu, J.-S. & Wan, L.-J. Nanostructured Materials for Electrochemical Energy Conversion and Storage Devices. *Adv. Mater.* **20,** 2878–2887 (2008).

147. Giraldo, L. F. *et al.* Mesoporous Silica Applications. *Macromol. Symp.* **258,** 129–141 (2007).

148. Zhao, L., Qin, H., Wu, R. & Zou, H. Recent advances of mesoporous materials in sample preparation. *J. Chromatogr. A* **1228,** 193–204 (2012).

149. Castelletto, V. & Hamley, I. W. Morphologies of block copolymer melts. *Curr. Opin. Solid State Mater. Sci.* **8,** 426–438 (2004).

150. Asghar, K. A., Elliott, J. M. & Squires, A. M. 2D hexagonal mesoporous platinum films exhibiting biaxial, in-plane pore alignment. *J. Mater. Chem.* **22,** 13311 (2012).

151. Zhou, Y. *et al.* Ultrasonic-assisted synthesis of carbon nanotube supported bimetallic Pt–Ru nanoparticles for effective methanol oxidation. *J. Mater. Chem. A* **3,** 8459–8465 (2015).

152. Fujigaya, T., Okamoto, M., Matsumoto, K., Kaneko, K. & Nakashima, N. Interfacial Engineering of Platinum Catalysts for Fuel Cells: Methanol Oxidation is Dramatically Improved by Polymer Coating on a Platinum Catalyst. *ChemCatChem* **5,** 1701–1704 (2013).

153. Hong, Y.-H., Tsai, Y.-C., Hong, Y.-H. & Tsai, Y.-C. Electrodeposition of Platinum and Ruthenium Nanoparticles in Multiwalled Carbon Nanotube-Nafion Nanocomposite for Methanol Electrooxidation, Electrodeposition of Platinum and Ruthenium Nanoparticles in Multiwalled Carbon Nanotube-Nafion Nanocomposite for Methanol Electrooxidation. *J. Nanomater. J. Nanomater.* **2009, 2009,** e892178 (2009).